Master's thesis

NTNU
Norwegian University of Science and Technology
Faculty of Natural Sciences
Department of Materials Science and Engineering

Hans-Olav Meløy

# Influence of synthesis techniques and morphology on electrochemical properties in manganese based lithium ion batteries.

Master's thesis in Chemistry
Supervisor: Hilde Lea Lein
May 2019

NTNU
Norwegian University of
Science and Technology

Hans-Olav Meløy

# Influence of synthesis techniques and morphology on electrochemical properties in manganese based lithium ion batteries.

Master's thesis in Chemistry
Supervisor: Hilde Lea Lein
May 2019

Norwegian University of Science and Technology
Faculty of Natural Sciences
Department of Materials Science and Engineering

NTNU
Norwegian University of
Science and Technology

# Acknowledgments

All work on this thesis was carried out at the Department of Materials Science and Engineering, Norwegian university of Science and Technology (NTNU). My biggest thank most go to my supervisors Elise Ramleth Østli, Fride Vullum-Bruer and Hilde Lea Lein for all the help they have given me during my time here. The rest of the battery group does also deserve special thank, particularly Nils P. Wagner, Andreas Norberg and Harald Pollen. I would also like to extend my thanks Pei Na Kui, Kristin Høydalsvik Wells and Yingda Yu for all the help they have given me with the technical parts.

I must of course thank all the people I have meet in my five years here at NTNU, for making these years fantastic. My flat mates in Øvre Bergsvingen 10 also deserves a shoot-out, especially Asai for being a great cat. And at last I would like to than my parents and brothers for always being there for me.

# Summary

The purpose of this thesis is the synthesis of $LiMn_2O_4$ with different morphologies and the impact this have on its use for high-voltage lithium ion batteries (LIB). Through sol-gel synthesis and coprecipitation, phase pure $LiMn_2O_4$ were synthesised successfully and selected samples was used in the assembly of lithium ion half cells. A large number of synthesis with different parameters were completed for both techniques, which resulted in a large number of samples with a secondary $Mn_2O_3$ phase. Both techniques showed that they could produce $LiMn_2O_4$ with a variety of morphologies. Open sponge like structures, porous ellipsoids and particles with wide size distribution have been synthesised. Sol-gel synthesis was either the citric acid method or Pechini method. Different calcination temperatures were used, as well as some samples with active pH control. Altering the pH of the gel yielded no usable results. Synthesis of $LiMn_2O_4$ through coprecipitation was done through precipitation of $MnCO_3$. Heat treatment of $MnCO_3$ was done to form $MnO_2$ for some samples. Both $MnCO_3$ and $MnO_2$ was attempted mixed with $LiNO_3$ with mortar and pestle, ball milling, and mixing in a water dispersion. Mixing by hand in mortar and pestle and ball milling proved far insufficient to get the desired phase pure $LiMn_2O_4$, while the water dispersion technique however provided the desired result. Phase purity was evaluated through X-ray diffraction. Scanning electron microscopy was used to analyse morphology, and overall surface area was found for selected samples.

Phase pure samples from both techniques was used to assemble lithium ion half cells to evaluate their electrochemical properties. An cathode slurry was prepared by mixing $LiMn_2O_4$ powder with carbon black N-Metyl-2-pyrrolidione (NEP) polyvinylidene fluoride binder in both 5 and 10 % by weight. The slurry was casted on a aluminium foil current collector, and cathodes cut from the foil. Prepared cathodes were assembled into lithium ion half cells in a glove box in a inert argon atmosphere, alongside a metallic lithium anode and $LiPF_6$ electrolyte.

The properties of the assembled cells were tested through galvanostatic charge-discharge cycling, to evaluate capacity, capacity loss and rate capability. Both materials had a low initial capacity of 81.2 mAh/g for sol-gel synthesised $LiMn_2O_4$ and 82.7 mAh/g for coprecipitated synthesis $LiMn_2O_4$. Both samples experienced rapid capacity fading, and next to no available capacity at high C-rates. There was only marginal difference between tested samples, but the sol-gel synthesis seemed superior.

Some evaluation of changes in the cathode cast was done following galvanostatic cycling. X.ray diffraction was taken of cycled and non-cycled casted cathode. And investigation into the surface microstructure was also done.

# Samandrag

Føremålet med denne avhandlinga er syntese av $LiMn_2O_4$ med varierande partikkel morfologi, og kva det si påverknad det vil væra for bruk i høg spennings litium ion batteri (LIB). Gjennom sol-gel syntese og medutfelling vart da vellukka syntetisert fase reint $LiMn_2O_4$, og utvalde prøvar vart nytta til å setja saman litium ion half celler. Eit høgt tall syntesar vart utført for båe sol-gel og medutfelling, som resulterte i eit høgt tall prøvar med ein sekundær fase av $Mn_2O_3$. Begge teknikkar viste at dei kunne nyttast til å laga $LiMn_2O_4$ med eit utval av ulike morfologiar. Opene svamp likande partikklar, porøse ellipsoidar og prøvar med stor variasjon i partikelstørrelse har vorte laga. Sol-gel syntesen var enten sitron syre eller Pechini metoden. Endring i båe kalsinerings temperatur og pH-control vart forsøkt. Endring i pH leia ikkje til noko brukbart resultat. Syntese av $LiMn_2O_4$ gjennom medutfelling vart gjort gjennom først utfelling av $MnCO_3$. som alternativt vart varmebehandla for å forma $MnO_2$. Båe $MnCO_3$ og $MnO_2$ vart blanda med $LiNO_3$ etterfølgt av kalsinering. Tre like blande teknikar vart utprøvd, for hånd med mørter og pestel, ball mølling og vatn dispergering. Verken bruk av mortar og pestel og ball mølling gav ønskja fasereine $LiMn_2O_4$ men, vatn dispergering oppnådde dette derimot. Analyse av fase reinleiken til alle prøvar vart gjort gjennom røntgen diffraksjon, mens analyse av overflate areal og morfologi gjennom sveipelektronmikroskop.

Utvalde fasereine prøvar frå både sol-gel syntese og medutfellings syntesen vart nytta til å setja samen litium ion halv celler, for å analysera materialets eigenskap før dette føremål. Ein katode slurry vart laga med å blanda $LiMn_2O_4$ pulver med svart karbon, N-metyl-2-pyrrolidon (NEP) of ployvinyldiene flourid bindemiddel i båe 5 % og 10 % forhold etter masse. Blanda slurry vart smørt ut over ein aluminiumsfolie straum samlar, og katodar av passande størrelse vart kutta ut. Ferdig framstilte katodar vart saman med ein metallisk litium anode og $LiPF_6$-elektrolytt sett saman til ei halv-celle.

Eigenskapane til dei samansett cellene vart evaluert gjennom galvanostatisk sykling, for å bedømma kapasitet, tap av kapasitet og rate evne. Begge valte materialar hadde låg kapasitet ved start med 81.2 mAh/g for produkt frå sol-gel syntesen og 82.7 mAh/g for produkt frå medutfellinga. Begge prøvane opplevde raskt tap av kapasitet, og tilnærma inga tilgjengeleg kapasitet ved høge C-rater. Det var lite forskjell mellom produkta som vart testa, men $LiMn_2O_4$ fr sol-gel verka som det betre val.

Vidare evaluering av endring i forskjellen mellom sykla og usykla katode vart gjort etter galvanostatisk sykling. Røntgen diffraksjon vart teken av både testa og utesta støypte katodar. Vidare så vart endingar i mikrostrukturen analysert før og etter bruk.

# Contents

# Chapter 1

# Introduction

At the dawn of history when mankind first learned to harness fire, the use and storage of energy have been an essential part of the development of our society. The burning of wood and coal permitted cooking of food, metalworking and burning of primitive ceramics. Taming the wind and river currents provided mechanical energy for use in windmills, sawmills and water pumps. Even as technological advances were made during the antique and middle ages, the global energy demand remained fairly constant. However, as the scientific understanding gained during the age of Enlightenment lead to the industrial revolution, the use of energy skyrocketed. As new machines were developed, alongside new ways of metal forging and advanced in chemical production a far larger concern grew for the nation states for reliable energy sources. This need has so far been largely covered by fossil sources as, coal, oil and natural gas, which have been able to cover most of the energetic demand of the globe [1, 2].

These sources are not without their issues however, the source of fossil fuels are finite and more pressing, the rising $CO_2$-levels. As the levels of $CO_2$ in the atmosphere rises, the changes in global climate seem to lead to catastrophic ecological and sociological consequences. To counteract this, a increased research have been focused on green energy sources the last 20 years. This is however not enough, as many renewable energy sources suffers from storage issues, as no large scale renewable energy storage exits in the global scale. One proposed solution in the application of large-scale battery systems connected to the power grid, which can store excess energy and supply the network when required. And among the cell on the market today the lithium-ion battery (LIB) offers the best possible properties, regarding lifetime and energy density. LIBs are already an established technology as their use in full electric and hybrid electric vehicles, portable electronics and other electrical applications which are not connected to the power grid. However, even as LIBs in a mature technology, there is still the opportunity and demand for significant improvements should the technology be able to compete with fossil sources for energy storage. With a rather low energy density, low power density high cost, safety concerns and pressure on scarce materials there is a list of issues related to LIBs [1–4].

One option to increase both energy and power density of LIBs are to increase their operating voltage, by utilizing high voltage cathode materials. There is however several issues related to high-voltage lithium ion cell, such as decomposition of electrolyte and

dissolution of specific elements from the cathode during use. The latter is especially an issue for manganese-based electrodes. As the $12^{th}$ most abundant element in the earths crust combined with a high potential for the $Mn^{4+} \longrightarrow Mn^{3+}$ reduction versus lithium, the use if manganese in high-voltage LIBs is highly desired. However the dissolution of manganese, Jahn-Teller distortion and other reasons makes the stability of $LiMn_2O_4$ far to low for commercial purposes [5–9].

Several different ways have been proposed to increase the stability of the cathode, as surface doping, the addition of Nickel to the structure to form LiMnNiO [10, 11] synthesis of core-shell structure. [12–14] and synthesising the particles with different morphologies [15–18] The latter have found to have a high impact on the electrochemical properties of the material, when used as cathode for LIBs.

## 1.1 Aim of work

The aim of this work was the analysis on the effect of different synthesis techniques and particle morphologies on the electrochemical properties of $LiMn_2O_4$. The goal is to synthesise a phase pure $LiMn_2O_4$ through sol-gel synthesis and coprecipitation, with different morphologies and analyse the impact on overall electrochemical properties. Electrochemical analysis is to be done through galvonostatic cycling, to evaluate, capacity, capacity fading and evaluation at different cycling rates. Further some comparison of the cells before and after cycling will also be done.

# Chapter 2

# Theory

## 2.1 Lithium ion batteries

Simply put, a battery is a device made from one or several galvanic cells, which can convert stored chemical energy into electrical work through a locally separated spontaneous redox reaction. A working galvanic cell consists of two electrodes, the cathode and anode, separated by the electrolyte and a separator, as seen in Figure 2.1 [19–22].

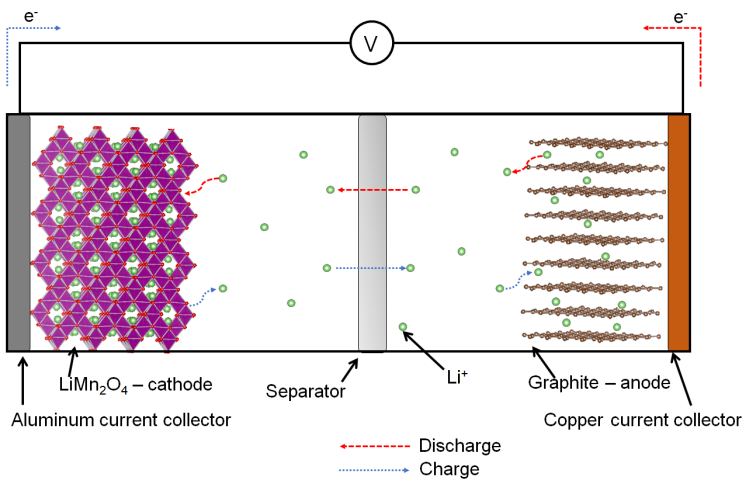


**Figure 2.1:** A lithium ion battery with $LiMn_2O_4$-cathode and a graphite anode [20], cathode and anode structures made with VESTA [23].

The electrochemical reactions occur at the electrodes, the positive cathode is reduced, while the negative anode is oxidised. This process is driven by an overall reduction of Gibbs free energy ($\Delta G$), due to a difference in the electron density at the electrodes. Thus connecting the cell to an external circuit, the electrodes comes into electrical contact. And a

spontaneous flow of electrons between the electrodes through the extranl circuit is permitted. Internal charge neutrality is preserved through an internal ionic circuit and a charge transfer reaction at the electrodes. The charge transfer reaction is an oxidation/reduction reaction which converts the electric current between the external electronic part and the internal ionic part. For a cell with a $LiMn_2O_4$ cathode and graphite ($C_6$) anode the proposed reactions are

$$\text{Cathode reaction} \qquad \mathrm{Li^+ + Mn_2O_4 + e^-} \underset{\text{Charge}}{\overset{\text{Discharge}}{\rightleftharpoons}} \mathrm{LiMn_2O_4} \tag{2.1}$$

$$\text{Anode reaction} \qquad \mathrm{LiC_6} \underset{\text{Charge}}{\overset{\text{Discharge}}{\rightleftharpoons}} \mathrm{Li^+ + C_6 + e^-} \tag{2.2}$$

$$\text{Total reaction} \qquad \mathrm{Mn_2O_4 + LiC_6} \underset{\text{Charge}}{\overset{\text{Discharge}}{\rightleftharpoons}} \mathrm{LiMn_2O_4 + C_6} \tag{2.3}$$

Here Li does not change its oxidation state during the cycling, but rather acts as a charge carrier between the cells as it migrates between them during cycling. Electrodes are usually made from a mixture of active material, which reacts mixed with a binder and other additives to increase conductivity. This mixture is in contact with a current collector to ensure an easy connection between the cell and the external circuit. The cathode and anode terminology for reversible cells is technically only valid during discharge, as the reactions are reversed during charging. But due to the fact that the positive electrode in a secondary lithium ion battery commonly is referred to as the cathode, that terminology will be used in this thesis [19, 21, 24–28].

Due to the spontaneous nature of the electrochemical reaction, direct contact between the electrodes will result in the system short circuiting. To prevent this, the electrodes must be electronically insulated from each other. But an ionic exchange must occur to sustain the electrochemical reaction. These requirements are fulfilled by the separator and the electrolyte. The separator is an electronically inert material, which physically separate the electrodes form each other. In LIBs it is often a insulating porous ion conductive polymer. As it does not partake in the electrochemical reaction, it should be light and have a low resistance for the ionic current. The electrolyte is a medium which can transfer current in the form of ionic migration. In LIBs an organic compound with dissolved lithium salts, as $LiPF_6$ dissolved in ethylene carbonate and diethyl carbonate is ise as the electrolyte. As the transport medium for the ionic current, it should have an high ionic conductivity. In addition it should also have high electronic resistance. Thus an ionic current can pass between the electrodes and maintain a closed electrical circuit, with an internal ionic part and an external electronic part which is available for work [19, 21, 29–33].

Depending on the reversibility of the reactions, galvanic cells are divided between primary and secondary cells. In primary cells, the electrochemical reactions can not be reversed by applying an external electrical potential. In secondary cells however, the high energy state can be restored through the application of an external electrical potential. Thus a primary cell must be fabricated in its high energy state and discarded after use, while a secondary cell can be recharged and used again [19, 21].

### 2.1.1 Important parameters and properties

Certain parameters and properties of the system are important to consider before a secondary battery is considered for practical applications. Ideally each cell should have a high specific

capacity, high voltage, high specific power, a long cycle life, be safe during use, non-harmful to dispose off and cheap [19, 20]

The specific capacity is the amount of charge a system can store, given theoretically as

$$C_s = \frac{n \cdot F}{3.6M} \tag{2.4}$$

Where $n$ is the number of charges transferred in the reaction, $F$ is Faraday's constant (= 96485.3365 C/mol) and $M$ is the molar mass of the reacting material. 3.6 is an conversion factor, to convert $C_s$ to mAh/g. However, this value is rarely reached, as full reaction with the active material may not be feasible or reversible. The practical or reversible capacity is the capacity the system can store without irreversible loss of said capacity. As full charge or discharge of the cell may cause unwanted irreversible reactions to occur and thus a loss of capacity [19, 21, 34–36].

The electrical potential of the cell, termed the working voltage or open circuit voltage ($V_{OC}$) is the difference in the chemical potential of the cathode and anode, given as

$$V_{OC} = \frac{\mu_A - \mu_C}{e} \tag{2.5}$$

Where $\mu_A$ is the chemical potential of the anode, $\mu_C$ the chemical potential of the cathode and $e$ is the elementary charge of the electron ($= -1.602 \cdot 10^{-19}$ C). The practical working voltage is however, limited by the electrochemical stability window of the electrolyte. Which as shown in Figure 2.2 is dependent on the highest occupied molecular orbital (HOMO) and lowest unoccupied molecular orbital (LUMO) of the electrolyte. Some systems can however be kinetically stabilised even when $\mu_A >$ LUMO and/or $\mu_C <$ HOMO, through the formation of a solid electrolyte interface (SEI)-layer [3, 21, 34, 35, 37]

The overall performance of the cell in regards to energy which can be utilised is its specific power, given as

$$U = C_s \int_{start}^{stop} V_{OC}(t)dt \tag{2.6}$$

Specific power is usually given as $^{Wh}/_{kg}$ [21, 35].

The life time of a galvanic cell is usually set to 80% of its nominal capacity [19]. This loss of capacity is due to unwanted irreversible reactions within the cell. This may be unwanted reactions with the separator, electrolyte, mechanical stress related to the electrochemical reactions, passive layer formation, electrolyte decomposition, lithium deposition or for $LiMn_2O_4$ the dissolution of manganese [38–41]. A cell can lose capacity both during cycling and storage. The overall lifetime of the battery is a combination of what is named the cycle life and shelf life. The cycle life is the number of full charges and discharges the cell can maintain before the cut-off point has been reached. The cell may still deteriorate when not in use, and the shelf life is the time the cell can be stored before the cut-off point is reached [36].

Safety will always be of high concern in the implementation of new technology, as accidents and issues will result in negative public perceptions and in severe cases grievous harm or death. Due to the spontaneous nature of the elecrochemical reaction and the use of

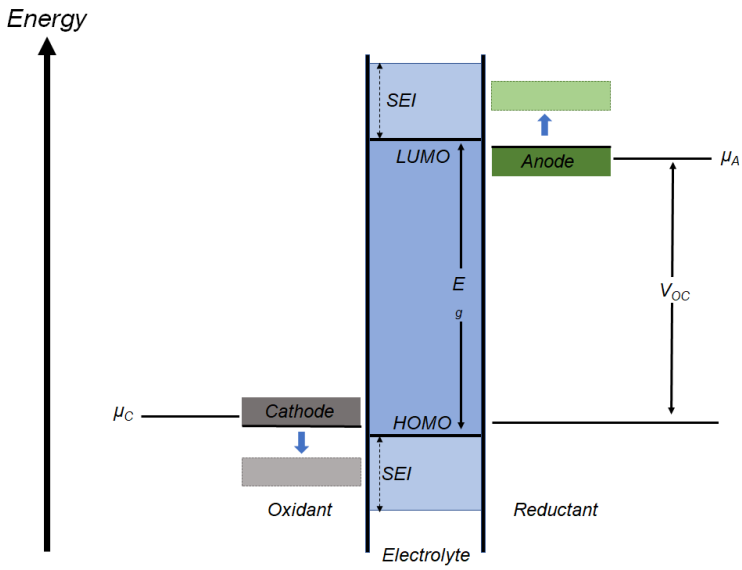


**Figure 2.2:** Relative energies of the anode and cathode and the permitted electrolyte window. $E_g$ is the energy separation between LUMO and HOMO of the electrolyte [3]

.

often reactive compounds as electrolyte, small issues within the cell can quickly spiral out of control and lead to grievous consequences [19, 42–44].

Lastly, the cost of implementation for both personal and public use will always be a factor. The cost is dependent on several factors, but can be approximated as the levelized cost of electricity ($LCOE$, in \$/KWh·cycle)

$$LCOE = \frac{C}{E \cdot n \cdot \eta} \tag{2.7}$$

Where $C$ is is the total cost of the storage system, both construction and operating cost, $E$ us the energy density per unit if mass, $n$ is the lifetime of the system in number of cycles and $\eta$ is the energy efficiency of the cell. From this the main goal for a battery should be clear, having a low cost of production and operation, a high energy density, long lifetime and high efficiency [6, 19].

## 2.2 Electrodes

As the sites of the electrochemical reactions and the link between the internal ionic circuit and the external electronic circuit, the properties of the electrodes are of paramount importance for LIBs [19, 21].

### 2.2.1 Intercalation electrodes

Due to their unsurpassed longevity compared to other electrodes utilised for galvanic cells, the intercalation electrode has become the type of choice for secondary cells [6].

An intercalation electrode is made from an open host structure, which permits diffusion of the charge carrier into and within its lattice. As a charged particle is inserted/extracted from the lattice during cycling, the host structure accepts or donates an electron form the external circuit in a spontaneous reaction to maintain electronneutrality. As an ion in a crystal structure always will be surrounded by ions of opposite charge, there is a barrier against ionic diffusion within a lattice. Further, an ion can only move between adjacent vacant sites. Thus to facilitate the electrochemical reactions, the host material should have an open crystal structure which alleviate internal $Li^+$-diffusion in the lattice. An typical example for this is $LiCoO_2$, shown in Figure 2.3. $LiCoO_2$ is made from a layered structure

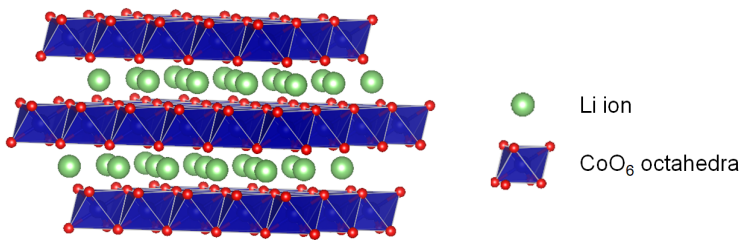


**Figure 2.3:** The layered $LiCoO_2$ structure [45], made with VESTA [23].

of alternating (111) planes of $Li^+$ and $[CoO_6]$-octahedra. The $CoO_6$-octahedra form a loose framework with two-dimensional channels for $Li^+$ transport, with a low barrier against $Li^+$-diffusion, as shown in Figure 2.4 [4–6, 21, 27, 46–48].

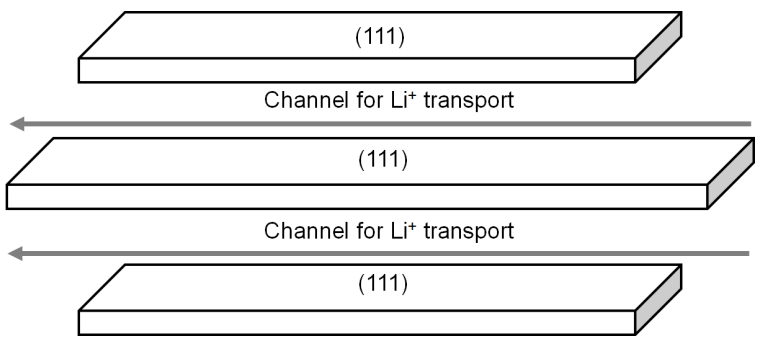


**Figure 2.4:** The layered $LiCoO_2$ structure [45], adapted from [49]

As the charge carrier does not react, but forces a reaction in the host material, the electrode should be made form materials with benifitial electrochemical properties. The free energy ($\Delta G$) of reaction should be high, with both high specific capacity and voltage. To maximise capacity, the amount of charge carrier which it can store should be as high as possible, with a reversible insertion/extraction mechanism. The material should be able

to react, and must thus contain at least one element which can change its oxidation state. Elements or systems with a high reduction potential are beneficial as they ensure a high electrical potential. To ensure longevity, the change in volume should be minimal, as any change in volume causes undesired strain upon the material. The rate of the intercalation reaction should be rapid, both during charge and discharge. To ensure this, the crystal structure of the host material should be open as to ease the $Li^+$-diffusion within its lattice. The material should be a mixed conductor, with high electronic and ionic conductivity. The material should be stable in regards to overcharge and overdischarge. And at last, it should be cheap, environmentally friendly and safe [5, 19, 29, 50].

No material used in modern practical cells fulfill all the demands mentioned to a perfect degree, for example $LiCoO_2$ is toxic and expensive. The most used intercalation electrode materials for LIBs are shown in Table 2.1. Common for all these materials are a modest

**Table 2.1:** Materials used as intercalation electrode materials for rechargable LIBs [6].

| | Material | Structure | Average voltage (V vs. Li \ $Li^+$) | Practical capacity (mAh/g) |
|---|---|---|---|---|
| Cathodes | $LiCoO_2$ | Layered | 3.9 | 140 |
| | $LiMn_2O_4$ | Spinel | 4.1 | 120 |
| | $LiFePO_4$ | Olivine | 3.45 | 160 |
| | $LiNi_{1/3}Mn_{1/3}Co_{1/3}O_2$ | Layered | 3.8 | 200 |
| | $LiNi_{0.8}Co_{0.15}Al_{0.05}O_2$ | Layered | 3.8 | 200 |
| Anodes | Graphite | Layered | 0.1 | 360 |
| | $Li_4T_5iO_{12}$ | Spinel | 1.5 | 175 |

capacity, but combined with a reversible insertion/extraction of $Li^+$ and thus a long lifetime [5, 6, 13].

### 2.2.2 The lithium anode and the solid electrolyte interface.

On the anode side, the $Li/Li^+$-anode would be ideal, due to having the lowest reduction potential amongst the metals ($-3.040$ V against the standard hydrogen electrode) and a theoretical capacity of 3860 mAh/g. However, due to dendrite formation which severely reduces its lifetime and safety issues, its implementation have proven impractical in commercial LIBs [51].

However, as it will be utilised during testing of cells in this thesis, some properties of it should be considered. The difference in electrical potential between the electrode and the electrolyte, results in the formation of a solid-electrolyte interface (SEI-layer) at the surface. The SEI-layer is made from the partial decomposition of electrolyte on the surface, and prevents further decomposition of electrolyte. Ideally the SEI-layer acts as an electronic insulator, but permits rapid transfer of $Li^+$ between the electrode and electrolyte. A thick SEI-layer is undesired as it inhibits the charge transfer and increases the internal resistance of the cell. The formation of the SEI-layer is accompanied by a capacity loss which usually occurs during the first cycle for commercial cells as $Li^+$ becomes trapped in the layer. This is will however not be an issue in this thesis, as the lithium anode will

provide $Li^+$ in far excess of the capacity of the active material This ensures that capacity loss due to SEI-formation can be ignored [37, 51].

## 2.3 $LiMn_2O_4$

$LiMn_2O_4$ have shown itself as a valid choice as a cathode material for lithium ion batteries, due to its low cost, high natural occurrence of manganese, non-toxicity and environmentally benign properties. With a theoretical capacity of 148 mA h/g, a practical capacity of 120 mAh/g alongside a average voltage against $Li/Li^+$ of $\approx$ 4 V, its energy density is high enough to be of interest for use in practical lithium ion batteries [5, 6, 9, 15, 52–54].

$LiMn_2O_4$ adopts the spinel structure in the $Fd\bar{3}m$ space group. The unit cell shown in Figure 2.5 shows a cubic structure, with a lattice parameter of 8.245 , with each cell consisting of 32 oxygen ions, 16 manganese ions and 8 lithium ions. The basis of the cell is the face centred cubic (fcc) stacking of $O^{2-}$, in which manganese occupies half the octahedral holes and $Li^+$ sites in one eighth of the tetrahedral positions. In regards to sites within the unit cell, oxygen occupies the 32e position, manganese the 16d position and lithium the 8a position [5, 27, 46, 55–58].

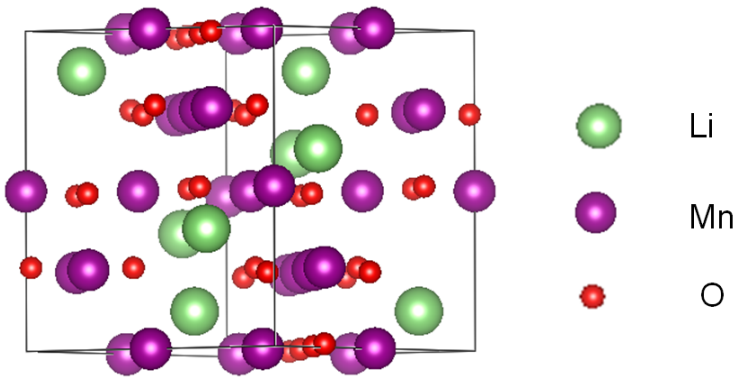


**Figure 2.5:** The unit cell of $LiMn_2O_4$, [55], made in VESTA [23].

The edge sharing $[MnO_6]$-octahedra form the stable host structure of the material in which interactions of manganese at the edges ensures an adequate electronic conductivity, as $e^-$ can move directly between metal ions. The octahedral arrangement as shown in Figure 2.6, leads to a structure of intersecting tunnels, shown in Figure 2.7. These tunnels provides channels for three dimensional lithium diffusion. $Li^+$ can move to and from 8a sites, through the adjacent 16c vacant site. This provide a network with a low barrier against $Li^+$-diffusion and insertion/extraction with a preservation of the original cubic framework. The practical capacity of 120 mAh/g corresponds to an insertion of $0.8Li^+$ per formula unit. [5, 15, 59].

Fully charged, the structure is delithiated and the insertion of $Li^+$ occurs in the 4 V region. As $Li^+$ is inserted, $Mn^{4+}$ is reduced to $Mn^{3+}$. Excess $Li^+$ can continuously be inserted until a maximum composition of $Li_2Mn_2O_4$ has been reached. This intercalation goes to the

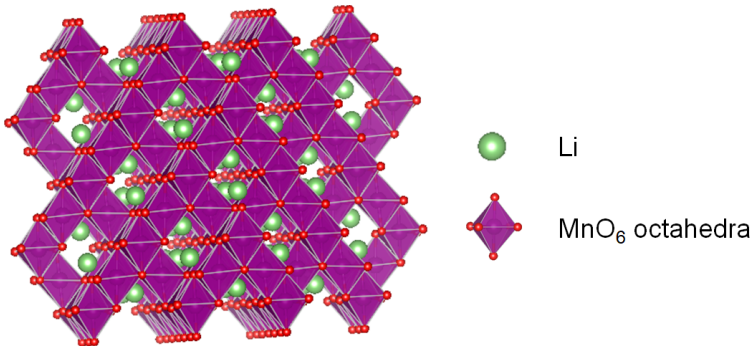


**Figure 2.6:** Shape of the edge sharing [$MnO_6$]-octahedra in $LiMn_2O_4$ and tunnels for $Li^+$-diffusion [55], made in VESTA [23].

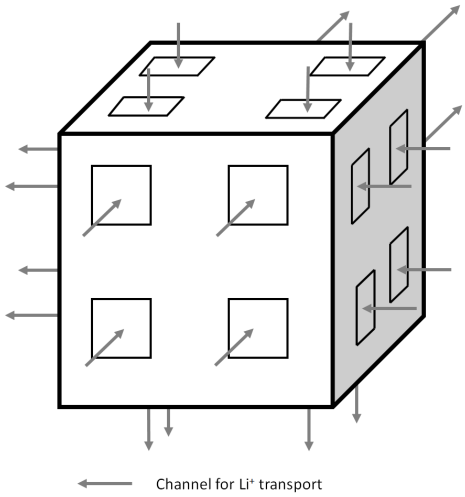


**Figure 2.7:** The diffusion tunnels in $LiMn_2O_4$, adapted from [49].

previously vacant 16c sites and occurs in the 3 V region. Even with a theoretical capacity of 296 mAh/g, the formation $Li_2Mn_2O_4$ is undesired, due to reduction of its structural integrity, due to Jahn-Teller distortion. As $Mn^{4+}$ with an electronic configuration of $[Ar]Mn^{4+}:3d^3(t_{2g}^3)$ is reduced to $Mn^{3+}$ with a electronic configuration of $[Ar]3d^4(t_{2g}^3e_g^1)$, the spin state changes from low to high spin as shown in Figure 2.8. This alters the preferred symmetry from

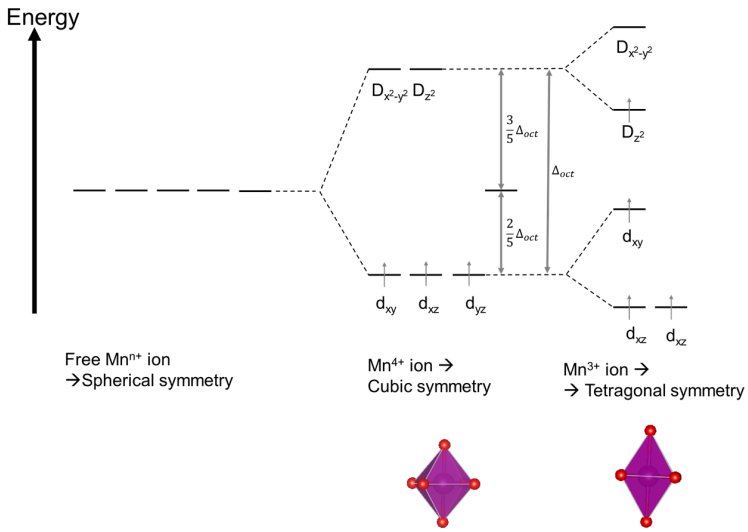


**Figure 2.8:** Molecular orbital diagram for $Mn^{4+}$ and the high spin state of $Mn^{3+}$. Alongside the preferred symmetry of the $MnO_6$-octahedra, adapted from [6].

cubic to tetragonal, which is accompanied by a volume expansion of 6.5%, resulting in a considerable strain in the structure. This damages the electrode and rapid capacity loss follows. Thus around 3 V, $LiMn_2O_4$ is not useful as an secondary lithium ion battery [5, 6, 15].

Further, even in the 4V range there is a loss of capacity, attributed to manganese dissolution into the electrolyte, Jahn-Teller distortion due to non-equilibrium cycling, formation of two cubic phases, loss of crystallinity and micro-strain present during cycling. The dissolution of manganese is considered to be the main source for capacity loss. As at elevated voltages, $Mn^{3+}$ can go through the following dissolution reaction

$$2\,Mn^{3+} \longrightarrow Mn^{2+} + Mn^{4+} \tag{2.8}$$

Where $Mn^{4+}$ remains in the structure while $Mn^{2+}$ dissolves into the electrolyte, which occurs especially at elevated temperatures and in the presence of HF [28, 60–62].

## 2.4 Electrolyte and the formation of HF

As mentioned briefly in Section 2.1.1, the large operating voltages present in LIBs, require electrolytes which can withstand the conditions. For LIBs the electrolyte are usually

a lithium salt dissolved in a organic medium, such as $LiBF_4$, $LiAsF_6$ $LiClO_4$ and most commonly $LiPF_6$. Even as $LiPF_6$ suffers some severe drawbacks, its overall properties such as conductivity, ionic mobility, dissociation constant and stability, still makes it the best candidate. $LiPF_6$ main issues are a low thermal stability and a spontaneous hydrolytic decomposition in the presence of trace amounts of water and alcohols. This hydrolytic decomposition results in the formation of reactive substances as HF, which lowers the overall performance of the cell, decomposes the electrodes and in worst case scenarios result in severe health hazards. As $LiPF_6$ is dissolved in a solvent, there is an equilibrium between the ionic dissociation and molecular dissociation compounds

$$\mathrm{LiPF_6} \rightleftharpoons \mathrm{Li^+} + \mathrm{PF_6}^- \tag{2.9}$$

$$\mathrm{LiPF_6} \rightleftharpoons \mathrm{LiF} + \mathrm{PF_5} \tag{2.10}$$

Where $PF_5$ as a strong Lewis acid reacts strongly and rapidly with water

$$\mathrm{PF_5} + \mathrm{H_2O} \rightleftharpoons \mathrm{POF_3} + 2\,\mathrm{HF} \tag{2.11}$$

Thus any trace amounts of water quickly becomes detrimental for the practical applications of the cell. [5, 63, 64].

## 2.5 Relation between particle morphology and electrochemical properties.

The size and shape of the particles which composes the cathode has a large influence on the electrochemical properties. As $Li^+$ diffusion occurs far faster in the electrolyte, than the solid bulk, the rate of the overall electrochemical reactions are dependent on the internal diffusion. Thus, large particles will result in an overall slower process as lithium most diffuse farther within the bulk phase. Further the use of samll particles have also shown the be beneficial, to minimise strain. As small particles will experience minimal change in volume, during cycling [16, 57, 65].

However smaller particles may inhibit overall performance as well. Even as smaller particle sizes will ease the $Li^+$ diffusion, the introduction of larger grain boundaries will have a negative effect. The introduction of small grain bound will reduce the conductivity of the cathode as $e^-$ most be transferred between grains. This increases the internal polarisation of the cell which alters the behaviour during charge and discharge [46, 47, 65, 66]

Published work exists on the influence of different morphologies of $LiMn_2O_4$. Porous microspheres have been used to increase the rate capability of $LiMn_2O_4$ as $Li^+$ can diffuse through the pores [18]. Further, samples with high surface areas can also mitigate this issue, as it shortens the internal $Li^+$ diffusion paths. However, a large surface area will also increase contact between $LiMn_2O_4$ and the electrolyte, which would result in However, a large surface area can quickly lead to a loss of electrochemical properties. As a large surface will aggravate the effect of HF present in the electrolyte [67].

## 2.6 Sol-Gel synthesis

The sol-gel synthesis has shown itself to be a viable option for the production of inorganic materials due to its simplicity, reliability and possibility to synthesise both simple and complex ceramic compounds, which include, $TiO_2$ [68], AlOOH [69], $Ce_2O(Co_3)_2$ [70], $(U,Pu)O_2$ [71], $ZrO_2$-$SiO_2$ glass fibers [72], $Ba_{0.6}Sr_{0.4}FeO_{3-\delta}$ [73] and of course $LiMn_2O_4$ [17, 27, 70, 74–80].

A sol is a dispersion of solid particles in a liquid medium, where the particles have at least one dimension in the colloidal scale, between 1 nm and 1 $\mu$m. While a gel is a non-fluid network, which extends through the liquid medium, made form either a polymer network or a network of agglomerates. Sol-gel synthesis thus consist of forming a colloidal sol of particles with the desired chemical composition and through ageing the solution turns into a gel, to prevent phase separation [27, 70, 78–81].

### 2.6.1 Citrate sol-gel synthesis

Citric acid, Figure 2.9 is a small organic acid which have proven itself useful in a wide range of sol-gel synthesis. As a weak triprotic acid, with all three acid groups able to depronate,

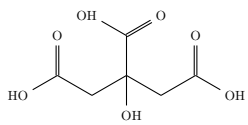


**Figure 2.9:** Citric acid

citric acid forms complexes with most metal ions and is thus an effective chelating agent, shown in Figure 2.10 [75, 78].

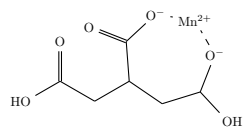


**Figure 2.10:** Citric acid coordinated to a Manganese ion

As metal ions are dissolved in water, water molecules will coordinate to said ions. This result in a weakening of the O-H bond on the coordinated water molecule and can thus depending on pH lead to deprotonation and hydrolysis as shown

$$[\mathrm{M(OH_2)}]^z + \rightleftharpoons [\mathrm{M{-}OH}]^{(z-1)+} + \mathrm{H}^+ \rightleftharpoons [\mathrm{M{=}0}]^{(z-2)+}\, 2\,\mathrm{H}^+ \tag{2.12}$$

By just dissolving metal salts, the removal of the solvent would lead to precipitation of the original salt or oxides/hydroxides. In the case of several dissolved metal ions, the precipitation would occur at different points due to differences in solubility. By forming a metal citric acid complex, the hydrolysis reaction is inhibited and the result is a more gel like substance with a homogeneous distribution of metal ions [78, 82].

As an acid, modifications of the pH have shown to impact citric acid and the resulting gel. As cations form complexes, deprotonation can enhance the cation bonding, prevent individual precipitation and a more homogeneous gel. The acid constant values of citric acid are given in Table 2.2 [78].

**Table 2.2:** The acid dissociation constant for citric acid for each deprotonation, alongside corresponding reaction.

| | Ka |
|---|---|
| $H_3Cit \rightleftharpoons H_2Cit^- + H^+$ | $7.10 \cdot 10^{-4}$ |
| $H_3Cit \rightleftharpoons H_2Cit^- + H^+$ | $1.68 \cdot 10^{-5}$ |
| $H_3Cit \rightleftharpoons H_2Cit^- + H^+$ | $6.40 \cdot 10^{-6}$ |

By dissolving metal salt precursors alongside citric acid, and evaporating water and allowing the gel to age an homogeneous gel should be the result. The gel can then be removed through pyrolysis in air, leaving the metaloxide [76, 78, 82].

### 2.6.2 The Pechini method

The Pechini synthesis, named after the original inventor is a modified sol-gel synthesis where alongside the metal cation precursors and complexing agent an polymeric agent is added [27, 78]

The polymeric agent is added to form the entire mixture into a polymeric network, which traps the metal ions as the solvent is removed. The main choice for polymeric agent is Ethylene glyole, shown in Figure 2.11, which is used alongside citric acid. Due

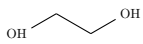


**Figure 2.11:** Ethylene glycol

to the hydroxyl groups, ethylene glycol can react with an organic acid or ester through a transesterification reaction. Along with citric acid, the following reaction occurs

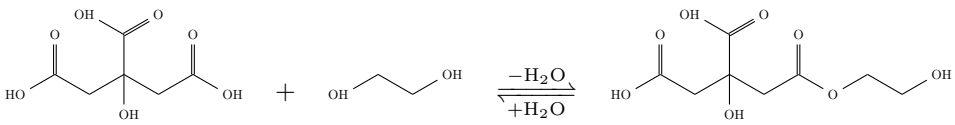


(2.13)

By continuously removing water from the system, the reaction is irreversible, and the system is thus turned into a covalent polymer network. This process is shown schematically in Figure 2.12. The sample is then heated to remove the organic components, as the polymeric gel will combust at high temperatures and leave a pure inorganic oxide [27, 78, 82].

### 2.6.3 Metal nitrate precursors alongside the sol-gel synthesis

In this thesis, metal nitrates serves as the precursors for the sol-gel synthesis. Which during heating experiences an rapid self-propagating combustion reaction. Around 200 °C there

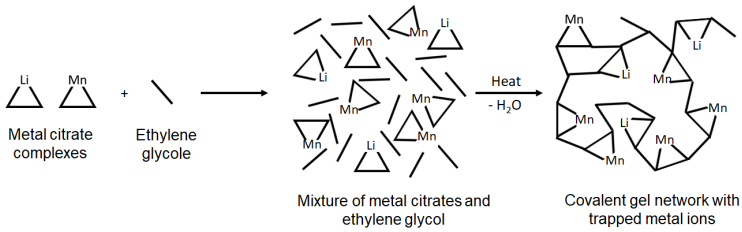


**Figure 2.12:** Schematic description for the pechini sol-gel synthsis, adapted from [78].

is usually a rapid loss of mass attributed to the decomposition of nitrates. This process is highly exothermic and results in a particle morphology with a high surface area, and a sponge like structure. The intensity of this reaction is highly dependent on the ratio of nitrates to citric acid. During the combustion the nitrates acts as oxidants while the organic components acts as a redundant. By altering the ratio through increasing the amount of organic components, the rate of the redox reaction is reduced, and the sample decomposes far more slowly [78, 83].

## 2.7 Coprecipitation synthesis for inorganic oxides

Coprecipitation have proven itself useful to synthesise inorganic oxides with a wide range of compositions and morphology's. Through coprecipitation intermediates are formed from dissolved solutes, which through further treatment provides the desired material as $LiMn_2O_4$ [27, 52, 84, 85].

The technique is based on precipitation of multi-component substances from a supersaturated solution. By having the concentration of solutes in a solution exceeding the solubility, the solution in termed to be supersaturated. The degree of supersaturation is given as

$$S = \frac{a}{a^*} \tag{2.14}$$

Where $a$ is the activity of solutes and $a^*$ is the activity at equilibrium. Or for dissolved ions

$$S = (\frac{IAP}{k_{sp,a}})^{\frac{1}{v}} \tag{2.15}$$

Where $IAP$ is the ionic activity product ($= a_{cations} + a_{anions}$), $k_{sp,a}$ is the activity based solubility constant and $v$ is the number of ions per formula unit of salt. As long as $S > 1$ the system is unstable and precipitation will spontaneously occur to lower the energy of the system, as the salt precipitates. The new solid phase has a lower free energy ($\Delta G_B$) than the previous dissolved phase. Precipitation from a homogeneous solution is not however instantaneous, due to the activation energy ($\Delta G^*$) required to form a new solid phase. As ions agglomerate and form a new solid phase, a new surface is also formed, with a non-zero surface energy ($\gamma$). Thus, the energetic gain of forming the new bulk phase ($\Delta G_B$) must compensate for the energetic cost of forming the new surface ($\Delta G_S$). As both $\Delta G_B$ and $\Delta G_S$ are dependent on the size of the particle. Particles where $\Delta G_S > \Delta G_B$, are not

stable and will disappear. The new phase is only stable when a critical size ($\Delta G_S = \Delta G_B$) have been reached, and the larger the size the more stable the new phase is, as shown in Figure 2.13. The critical size is a function of several parameters as chemical composition,

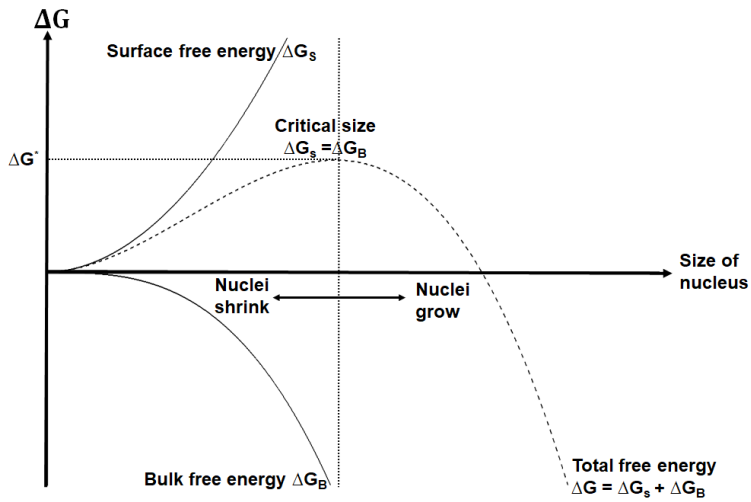


**Figure 2.13:** Diagram for the change in free energy of a precipitating particle, as a function of particle size. Adapted from [84].

temperature and naturally degree of supersaturation. For ions in a solution, this means that a particle must be formed due to fluctuations the solution, with a critical size to enable growth. When a particle of a stable size is formed, ions from the solution can b added to the particle which grows larger, in process known as crystal growth [84–88].

The formation of these nuclei is of high importance due to the effect they have on the morphology on the final product. Size and number of nuclei formed in the solution influences the particle size of the final product. Both formation of stable nuclei and subsequent growth consumes solutes and thus lowers $S$. The nucleation rate ($J$) is given as

$$J = A \exp \frac{-\Delta G^*}{k_B T} \tag{2.16}$$

Or alternatively as

$$J = k_j (S - 1)^j \tag{2.17}$$

Where $A$ is a pre-exponential factor and $K_B$ is Boltzmann constant, $k_j$ is the rate constant and $j$ is an exponential factor. As shown in Equation 2.17, there is a direct correlation between $S$, $J$ and $\Delta G^*$. If a high number if nuclei are formed, this will rapidly lower $S$ until $S = 1$ with only a limited time for growth is permitted. Here the all nuclei are formed around the same time resulting in a homogeneous size distribution in the precipitated product. In the opposite case if the number of nuclei formed per unit of time is low, the growth on the few particles formed will be the main reason for reducing $S$. While the formed particles grow, new stable nuclei are generated with a shorter growth time. Thus,

a low $S$ usually result in a more heterogeneous size distribution. By ensuring that $S$ is high when nucleation starts the chance of obtaining a precipitate product with a small and homogenous size distribution, while low degree of supersaturation usually result in a product with large particle size with a more heterogeneous size distribution [84–88].

Growth on stable nuclei occurs through attachment of solutes to the existing nuclei and is also an factor on the size and shape of finished particles. As solutes attach themselves to the surface of the particles, they are incorporated into their structure. Unsurprisingly the way they are incorporated is a significant factor in the size and shape of the final particle. The driving force for growth is the same as for nucleation, degree of supersaturation the higher the degree of supersaturation the more rapid the growth. In the case of slow (smooth) growth termed thermodynamic growth, added solutes are attached to the most stable sites. Which for a crystalline sample result in the final particle shape being an extension of the unit cell. For example an perfect cube for slowly precipitating NaCl. Faster (rough) growth, termed kinetic growth usually result on more rough particles as the solutes are incorporated onto sites rapidly. This usually result in more irregularly shaped particles. The relations between growth rate and particle shape is shown in Figure 2.14. This means that

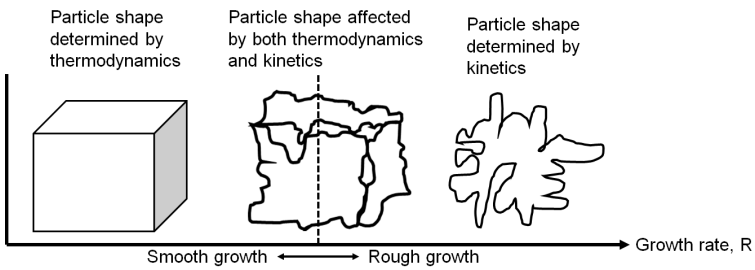


**Figure 2.14:** The shape of a crystalline particle with a cubic unit cell as a function of growth rate.

by modifying $S$ the growth rate can determine the shape of the crystalline particles formed [84, 85, 89].

### 2.7.1 Synthesis of $LiMn_2O_4$ through coprecipitation

So far this section have covered the formation of a solid phase from dissolved salts in a liquid phase, but with the exception of a few rare cases the precipitate will require further treatment to obtain a pure inorganic oxide. Often the precipitate formed does not have the desired chemical composition as a source of $O^{2-}$ is not readily available in a liquid medium. One way is to precipitate the metal cation followed by thermal decomposition of the anion to form the oxide. Metal salts with anions such as nitrate ($NO_3^{2-}$), carbonate ($CO_3^{2-}$), sulphate ($SO_4^{2-}$), oxalates ($C_2O_4^{2-}$) all decompose at high temperatures leaving an metal oxide. A scheme for this process is shown in Figure 3.3.

For $LiMn_2O_4$ the difference in solubility between lithium and manganese salt, shown in Table 2.3, indicates that the precipitation of manganese would occur at different points and thus result in several phases present in the final product. Thus trying to precipitate $LiMn_2O_4$ directly or through a common anion in ambient conditions would quickly prove

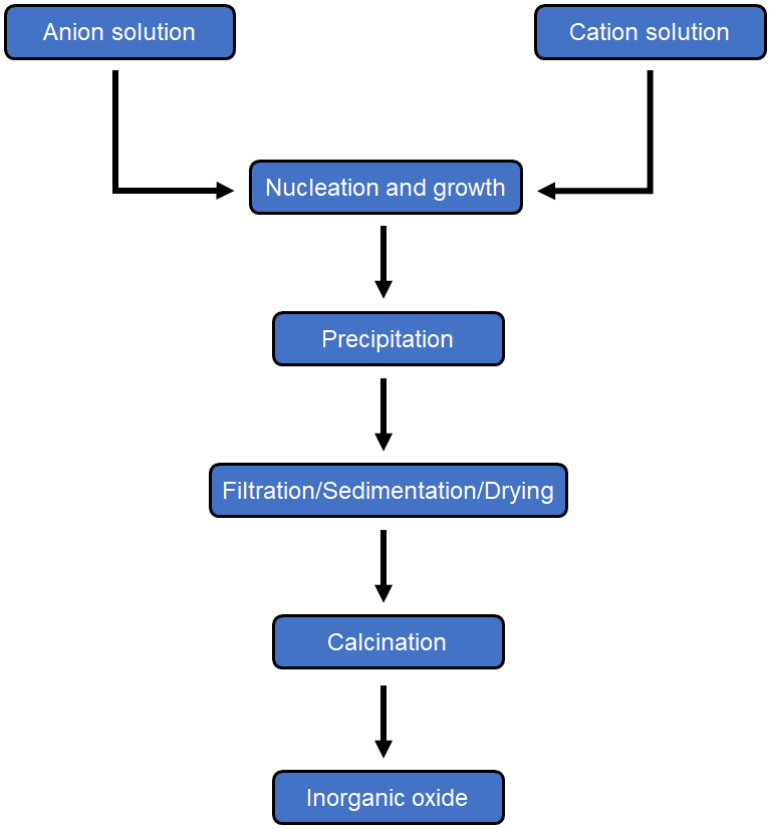


**Figure 2.15:** Scheme for the process of forming an inorganic oxide through co-precipitation

challenging.

$LiMn_2O_4$ have successfully been synthesised through precipitation of an manganese precursor which can be mixed with $Li^+$ through mechanical means, such as milling, grounding and etc. This followed by calcination have shown to yield a phase pure $LiMn_2O_4$ [16, 52, 53, 90].

Note should be taken on the resulting particle morphology, as it would dependent on shape of precipitating particle, mixing with $Li^+$ - source and calcination. The morphology of particles generated from co-precipitation, is influenced by several factors, from [16]

- Reagent concentration
- Nucleation and growth rate
- Ostwald ripening
- Collision with reactor walls and other particles
- Temperature

**Table 2.3:** Solubility of lithium and manganese salts used in this thesis, unless specified at $25\,^{\circ}\mathrm{C}$ [34]..

| Compound | Solubility [g/100 g] |
|---|---|
| $LiNO_3$ | 85 |
| $Li_2CO_3$ | 1.29 |
| $MnCO_3$ | 0.0065 |
| $Mn(NO_3)_2$ | Very soluble |
| $MN(CH_2CO_2)_2$ | $43^{5\,^{\circ}\mathrm{C}}$ |

- Influence and reaction with other components

The later point includes reactions with chelation agents, reversible of adsorption of other foreign species. By carefully monitoring synthesis conditions, irregular, cubic, sphericala and porous particles have been synthesised [16, 18, 52, 53, 90].

## 2.8 X-ray diffraction

After the discovery by Max von Laue in 1912 that X-rays passing through a solid crystal would be diffracted and produce a distinctive diffraction pattern, X-ray diffraction (XRD) have become an integral part in analysis of solid crystalline samples [91–93]. As a sample is irradiated by a collimated beam of monochromatic X-rays over a range of imminent angles, elastic collisions with atoms will scatter the rays. As the scattered rays interfere with each other, constructive interference of X-rays in phase will result in a diffracted ray. If the waves are in or out of phase, is determined by Bragg's law

$$n\lambda = 2dsin(\theta) \tag{2.18}$$

Where $n$ is an integer, known as the order of reflection, $\lambda$ is the wavelength of the X-rays, $d$ is the distance between two lattice planes, and $\theta$ is the diffraction angle between the the incoming X-rays and the normal of the crystal plane, as further shown in Figure 2.16 [91–96]. When the diffracted ray, exits the sample, its intensity will overshadow the imminent ray and the remnants of the waves that where out of phase and can thus be easily measured. By plotting the intensity as function of the angles ($2\theta$), Equation 2.18 can be used to determine the distance between the lattice planes [91–96].

For $LiMn_2O_4$, with the lattice parameters and atomic positions described in Section 2.3, the pattern can be calculated with Bragg's law in VESTA [23] and is shown in Figure 2.17.

When a crystalline powder is analysed, the different orientation and size of the crystals cause further wave interference. This non-complete destructive interference leads to a line broadening in the XRD-diffractogram, which can be related to particle dimension and size through the Scherrer formula

$$\langle L \rangle = \frac{K\lambda}{\beta cos\theta} \tag{2.19}$$

Where $\langle L \rangle$ is a measure of the dimension, in the direction perpendicular to the reflective plane, K is a constant (often 1), $\lambda$ is the wavelength if the X-rays, $\beta$ is the peak width at half

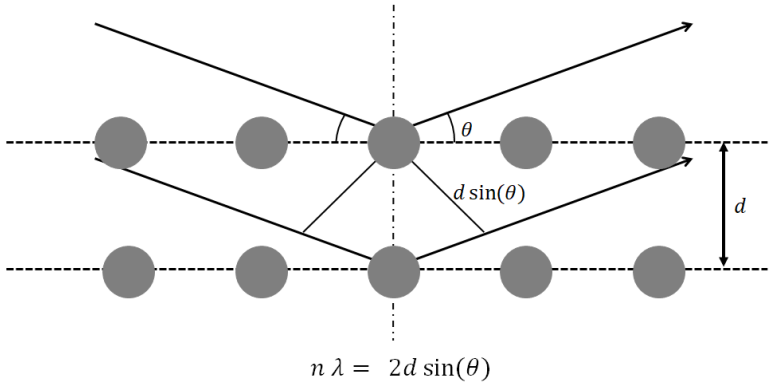


**Figure 2.16:** Working principle behind X-ray diffraction.

maximum and $\theta$ is the angle of the peak. Note, $\beta$ may also be affected by particle strain [93, 94, 96, 97].

## 2.9 The BET isotherm and surface analysis

The Brunauer-Emmett-Teller (BET) isotherm is a physical model which describes the adsorption of inert gases onto a solid surface. The model provides a useful tool for the determination of the surface area of a solid sample. By adsorbing an inert gas onto a surface cooled to the condensation temperature of said gas, the specific surface can be found by determining the number of molecules required to form a complete monolayer [94, 98, 99].

However, in practice a gas will not adsorb evenly upon a surface, resulting in the formation of mulitlayers, while at the same time some regions are uncovered. The size of the monolayer must then be found indirectly through the BET-isotherm. The derivation of said isotherm assumes that there is a dynamic equilibrium between the amount of adsorbed and free gas. It is assumed that molecules adsorb onto equivalent sites on the first layer. Adsorbed molecules serve as adsorption sites for subsequent adsorption. Interactions between adsorbates are ignored. Conditions for adsorption and desorption on layers beyond the first are equal and the the adsorption energy is equal to the condensation energy. And at the saturation pressure of adsorbing gas, the multilayer will grow to infinite thickness [94, 99].

Through the derivation of the BET-isotherm the following equation is used to determine the surface area of the sample

$$\frac{P}{V_a(P_0 - P)} = \frac{1}{\chi V_0} + \frac{(\chi - 1)}{\chi V_0}\frac{P}{P_0} = \eta + \alpha\frac{P}{P_0} \tag{2.20}$$

Where $P$ is the pressure, $V_a$ is the volume of gas adsorbed, $P_0$ is the saturation pressure, $\chi$ is a constant, describing the ratio of desorption between the first and second layer, $V_0$ is required adsorbed volume to form a complete monolayer on the sample. And $\alpha$ and $\eta$ are constant for the linear equation. Thus by measuring $V_a$ as a function of $P$ and plotting

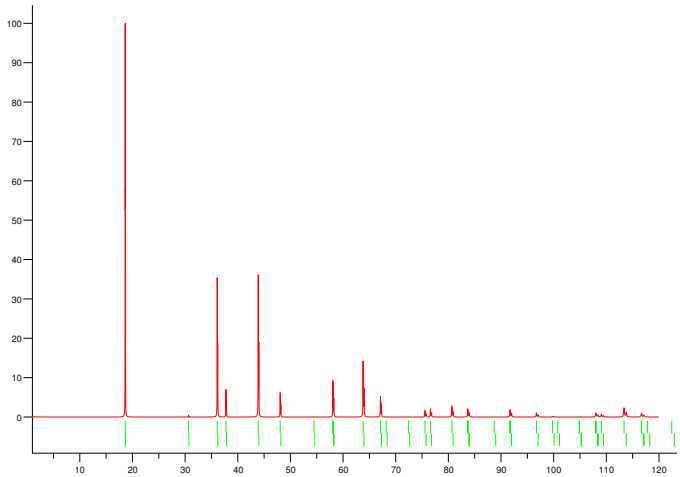


**Figure 2.17:** Theoretical XRD pattern for $LiMn_2O_4$, figure from VESTA [23], based on data from [55]. Note intensity is arbitrary and only reflects ideal relative height between peaks.

$\frac{P}{V_a(P_0-P)}$ versus $\frac{P}{P_0}$, a linear equation is found. $V_0$ is found form the equation as

$$V_0 = \frac{1}{\alpha + \eta} \tag{2.21}$$

And the surface area ($A$) follows as

$$A = A_0 \frac{PV_0}{k_B T} \tag{2.22}$$

Where $K_B$ is Boltzmann constant (=$1.381 \cdot 10^{-23}$ J K$^{-1}$) [94, 99].

## 2.10 Scanning electron microscopy and Energy-Dispersive spectroscopy

Scanning electron microscopy (SEM) is an imaging technique which offers far better magnification than optical microscopes. By bombarding a sample with a high energy beam of convergent electrons, magnifications up to 300 000 times can be reached, and information about particle morphology, topology and surface composition can be obtained. As the surface is scanned, the interactions between the sample and the electron beam generates a list of signals in the form of emitted electrons and X-rays, as shown in Figure 2.18. The SEM-apparatus will primarily generate the image and information based on the backscattered electrons (BSE), secondary electrons (SE) and emitted X-rays [94, 95, 100].

BSE are electrons from the injected beam that are scattered due to elastic and inelastic collisions with the specimen. Their energy are dependent on the incident beam, and are

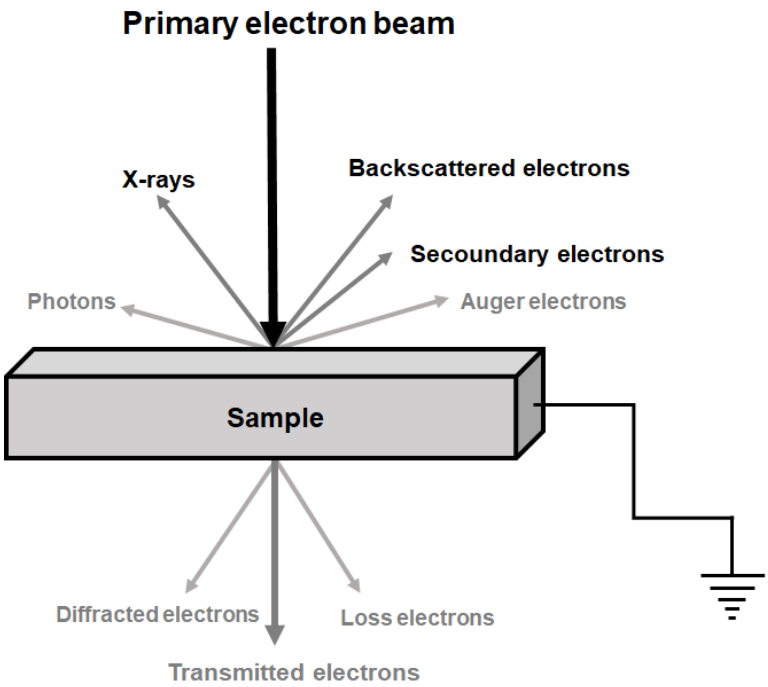


**Figure 2.18:** Interaction between a sample and an electron beam, adapted from [94].

equal or less than said beam. The fraction of BSE are dependent on atomic number and thus the heavier the element, the larger the fraction of BSE. The BSE image will reflect the chemical composition of the sample, even if it can't be used for elemental identification [94, 95, 100].

The injected electrons also lead to the emission of free and valence electrons from the sample. The energy of these are far lower than the BSE, and thus only emitted from the surface while those emitted from within are quickly reabsorbed. The amount of SE that is detected is inversely proportional with the angle between the electron beam and the normal of the surface. By monitoring the amount of SE, an image of the morphology and topography of the sample is generated [94, 95, 100, 101]

The high energy of the electron beam also leads to excitation of inner-shell electrons. The subsequent relaxation will lead to the emission of characteristic X-rays. As the energy is only dependent on the atomic band gap of the exited atom, it can identify the excited atom. This technique named Energy-disperse X-ray spectroscopy (EDS), can analyse the elemental composition of the surface of the sample. And information about, which elements are present, their occurrence as well their distribution can be obtained By scanning the surface, the elemental composition can be mapped and the distribution of surface elements can be obtained. Some importance is related to the resolution and discrimination of the instrument. As many elements emit characteristic X-rays with similar wavelength. Thus overlapping peaks may quickly lead to errors in the measurement if the user is not careful

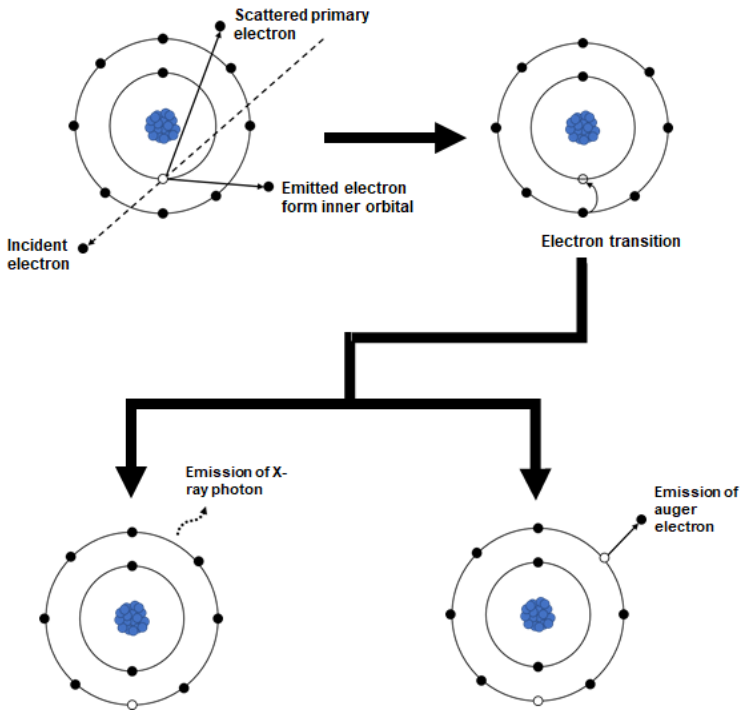


**Figure 2.19:** Ionisation of an inner orbital, followed by relaxation by electron transition. The relaxation is followed by the emission of a auger electron or a characteristic X-ray photon.

[94, 95, 100, 102].

SEM offers an effective toll in the analysis of particle morphology. The large magnification present offers a direct way to observe the sizes and shapes of the particles. Further EDS can be used to scan the surface, to determine elemental composition of places of interest [94, 100, 101].

## 2.11 Electrochemical characterisation

Even with the information about phase purity and particle morphology obtained from the other characterisation techniques, the electrochemical properties are still unknown. Thus, full evaluation of the material for use in high-voltage LIBs should follow after electrochemical analysis. In its simplest form, the material of interest is used to assemble a working galvanic cell, which is repeatedly charged and discharged in order to evaluate its electrochemical properties [19, 48].

Usually the active material is used as a cathode against the pure metallic lithium anode, in an assembly termed a half cell. As the metallic lithium anode provides $Li^+$ in far excess of what can be intercalated into the active material this has a number of benefits. Firstly the capacity is only determined by the active material, and the $Li^+$ trapped in the SEI-layer does

not impact the electrochemical properties of the cell. Further as mentioned in Equation 2.5 in Section 2.1.1, the $V_{OC}$ of a galvanic cell is a function of the chemical potential of both the cathode and anode. For intercalation electrodes the chemical potential is given as

$$\mu = (\frac{\partial G}{\partial x}) \tag{2.23}$$

Where $x$ is the amount of intercalated lithium. Thus, changes in the chemical composition leads to changes in chemical potential. As only the properties of synthesised samples is of interest in this thesis, $\mu_A$ should be constant as to not influence the measured voltage of the cell. As long as the metallic lithium anode provides $Li^+$ in far excess this is ensured as the changes in chemical composition during cycling is minimal and thus changes to its chemical potential. Then as long as this is the case, changes in $V_{OC}$ should only be influenced by changes in $\mu_C$ which occurs during cycling [6, 21, 48, 103, 104].

When an assembled cell is cycled, the current passing through and operating voltage can easily be measured, and form this valuable information about capacity, operating voltage, energy density, capacity loss and information about electrochemical reactions be obtained. By plotting cell voltage as a function of current passing through the cell, the behaviour of the voltage as a function of state of charge or discharge is obtained. This is termed a current-voltage diagram, and among other things gives information about the power ($P$) as

$$P = I \cdot V_{oc,t} \tag{2.24}$$

Where $I$ is the electric current and $V_{oc,t}$ is the open circuit voltage at time $t$. In this thesis it is of higher interest of looking at the behaviour of $V_{oc}$ as a function of specific capacity, this is done by dividing passing current for a single charge or discharge with the mass of active material. Ideally $V_{oc}$ should be constant and drop to 0 in a single step during discharge to maximize the energy and power density of the cell. This is however not the case for real systems, as $V_{oc}$ drops as the cell is discharged. $LiMn_2O_4$ have a distinct charge-discharge curve consisting of two plateaus, with a voltage small voltage drop around $1/3$ of its spent capacity [5, 19].

As loss of capacity is one of the large challenges of using $LiMn_2O_4$ as the active material for LIB cathodes, monitoring changes in capacity as a function of charge-discharge cycle is of high interest. Changes in cell capacity is easily found by measuring capacity both during charge ($Q_{charge}$) and discharge ($Q_{discharge}$). Comparison of $Q_{charge}$ and $Q_{discharge}$ yields information about cell efficiency. The cell efficiency is an indication of energetic loss for the system during a cycle, as more energy is used to charge the cell, than what is received during discharge. Cell efficiency is given as either coulometric efficiency ($q_{ah}$) and energy efficiency ($q_{wh}$)

$$q_{ah} = \frac{Q_{discharge}}{Q_{charge}} \cdot 100\% \tag{2.25}$$

$$q_{wh} = q_{ah} \frac{\bar{V}_{oc,discharge}}{\bar{V}_{oc,charge}} \cdot 100\% \tag{2.26}$$

Where $\bar{V}_{oc,discharge}$ is the average terminal voltage during discharge and $\bar{V}_{oc,charge}$ is the average terminal voltage during charge. As $q_{ah}$ <1, there is a difference in cell

capacity during charge and discharge, due to incomplete and irreversible electrochemical reactions and insertion/extraction of $Li^+$. This value is however rather high for LIBs, often approaching 100 %. $q_{wh}$ is the difference in available work during each charge and discharge. As $q_{wh}$ is dependent on cell voltage, internal resistance present during both charge and discharge will lower the overall efficiency.

The capacity a cell can deliver is not only dependent on active material and cycle number, rate of charge and discharge will also affect the system. This is given as the C rate

$$\mathrm{C} = \frac{\text{Discharge current}}{\text{Nominal capacity (In ampere hours)}} \tag{2.27}$$

A higher C rate indicates a higher current passing through the cell, which will lead to higher internal resistance and polarisation. As cells are usually cycled between an upper and lower voltage value, the higher electrical resistance will lower the available cell capacity. Thus the capacity for an electrochemical active material is given at a defined C-rate, often C/20 [19, 25, 105].

The measurements and possible results and plots presented so far does not give any information about the chemical reactions which occurs during cell cycling. One way to do this is plotting the differential capacity ($dQ/dV$) as a function of voltage, in a technique termed differential capacity analysis. The corresponding plot yields a fingerprint for the materials tested, and cell with similar composition should yield similar plots. As the entire cycle, both charge and discharge are plotted, the plot yields a cyclic voltagram. The analysis yields information about at which voltages the reactions occur at, with the presence of characteristic peaks. $LiMn_2O_4$ when cycled against $Li/Li^+$ have a characteristic differential capacity plot. Two plateaus around 3.8 V and 4.1 V is common as the this is the region where most of the electrochemical reactions occur around these voltages. An poor $LiMn_2O_4$ sample will have additional peaks around 3.3 V and 4.5V, the peak around 3.3 V indicates oxygen deficiency present while the peak around 4.5 V indicates the replacement of $Li^+$ sites with $Mn^{4+}$ ions. Further uses for differential capacity analysis is to compare different cycles, by plotting dQ/dV as a function of both V and cycle number (n). Through this changes between in the electrochemical reaction between different cycles can be monitored [25, 106–108].

# Chapter 3

# Experimental

All pure chemicals, solvent used for synthesis, milling and as a dispersion medium is shown in Table 3.1.

**Table 3.1**

| Name | Formula | Purity | Producer |
|---|---|---|---|
| Lithium Nitrate | $LiNO_3$ | 99 % | Alfa Aesar |
| Manganese nitrate tetrahydrate | $LiNO_3 \cdot 4H_2O$ | 97. 5 % | ACROS Organics ™ |
| Citric Acid | $C_6H_8O_7$ | 99 % | Sigma-Aldrich |
| Ethylene glycol | $C_2H_6O_2$ | 99.8 % | Sigma-Aldrich |
| Ammonia (25 %) | $NH_3$ | $>$ 99.9 % | Sigma-Aldrich |
| Nitric acid (65 %) | $HNO_3$ | $>$ 99.9 % | Sigma-Aldrich |
| Manganese acetate tetrahydrate | $Mn(CH_3CO_2)_2$ | $\geq$ 99.0 % | Merck Group |
| Ammonium bicarbonate | $NH_4HCO_3$ | $\geq$ 99.5 % | Sigma-Aldrich |
| Ethanol (96%) | $C_2H_5OH$ | $<$ 1 ppm | VWR International |
| Isopropanol | $C_3H_8O$ | $<$ 5 ppm | VWR International |
| 1-Ethyl-2-pyrrolidone (NVP) | $C_5H_9NO$ | 98 % | Sigma-Aldrich |
| Polyvinylidene fluoride (PVDF) | $-(C_2H_2F_2)n-$ | 100 % | Solvay S.A. |
| Carbon black | C | $>$ 95 % | Imerys Graphite & Carbon |
| Diethyl carbonate | $(C_2H_5O)_2CO$ | $\geq$ 99 % | Sigma-Aldrich |

## 3.1 Synthesis of active material

### 3.1.1 Standarisation of $Mn(NO_3)_2$

To accurately monitor the stochiometry of $Mn(NO_3)_2 \cdot 4H_2O$, a standardised solution was made according to [109].

$Mn(NO_3)_2 \cdot 4H_2O$ was dissolved in deionised water. 5 porcelain crucibles was heated to 600 °C for 6 hours. The crucibles was cooled to 400 °C, removed from the furnace and cooled in a desiccator and weighted. 5 - 10 mL of the $Mn(NO_3)_2 \cdot 4H_2O$ solution was

transferred to each crucible. The crucibles was weighted with the added $Mn(NO_3)_2 \cdot 4H_2O$ - solution and transferred to a furnace. The samples was heated to 600 °C to ensure removal of all traces of water and organics and ensuring complete decomposition of $Mn(NO_3)_2$ to $Mn_2O_3$. The samples and crucibles was cooled to 400 °C, transferred to a desiccator, cooled to room temperature and weighted. Concentration of $Mn(NO_3)_2$ was determined from the average of the measurements, with standard deviation of a order of $10^{-7}$.

### 3.1.2 Sol-gel synthesis

The general procedure behind synthesis of $LiMn_2O_4$ through sol-gel synthesis were dissolving metal ions, complexion agent (citric acid) and optionally ethylene glycol, $HNO_3$ and $NH_3$ in deionised water. Followed by ageing of gel, drying/combustion, calcination and milling. The process is based in work from Zhang et al. [74], Yang et al. [76] and Bulut et al. [110].

$LiNO_3$ was dried at 95 °C overnight under vacuum, while a standardised $Mn(NO_3)_2$-solution was prepared as described in Section 3.1.1. Other chemical used was used without further treatment. $LiNO_3$ and $Mn(NO_3)_2$ were mixed in stochiometric proportions, either 1:2 or 1.05:2 ratio. Citric acid was added in stochiometric proportions to total number of metal ions in a 1:1 or 1:2 ratio. Optionally, ethylene glycol was added in stochiometric proportions to citric acid in a 1:2 ratio. In some samples the pH was modified through the addition of $NH_3$ or $HNO_3$. $NH_3$ or $HNO_3$ was added dropwise after all other components, to the solution under stirring, until desired pH was obtained. The gel was left to age under stirring on a hot plate at 85 °C overnight.

Depending on ratio of metal ions to citric acid the gel was either combusted or dried. Samples were the metal ion:citric acid ratio was 1:1 experienced a sudden and violent combustion around 205 °C, attributed to the decomposition of nitrates [78, 83]. To control this reaction, a long combustion tube was used. The gel was added to the tube, which was put on a hotplate on 250 °C. The sample was heated until a sudden combustion reaction occurred, as shown in Figure 3.1. The combustion yielded a fine black powder. Samples

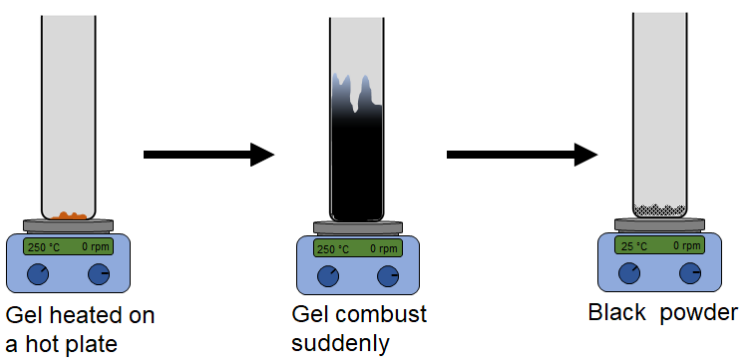


**Figure 3.1:** Illustration of gel combustion

with a metal ion:citric acid ratio of 1:2, the combustion reaction was not observed, these

samples were dried overnight at 150 °C. Dry gel was grinned into a fine powder by hand with mortar and pestle.

All samples were calcined for 20 hours at different temperatures. Calcined powder was wet milled overnight in isopropanol, in a 4.5 cm diameter plastic flask with Zirconia 5 mm diameter (Nikkato Corporation, 95 % $ZrO_2$, 5 % $Y_2O_3$) milling balls at 205 rpm overnight. An complete overview of the synthesis process is shown in Figure 3.2

Information about different stochiometric ratios used, calcination temperature, combustion or drying and corresponding sample id can be found on Table 3.2. In general the synthesis aimed at producing 3 grams of $LiMn_2O_4$, with the exception of sol-gel CA2, where 10 grams was produced, masses used can be found in Table 3.3.

**Table 3.2:** The different parameters used in the sol-gel synthesis, and the corresponding sample id. Note, CA = citric acid, MI = Total amount of metal ions in solution, EG = ethylen glycol, UA = pH was not activly modified in the sample.

| Molar ratio $Li^+ : Mn^{2+}$ | Molar ratio CA : MI | Ratio CA : EG | pH | Combustion /Drying | Calc. T [°C] | Sample id. |
|---|---|---|---|---|---|---|
| 1:2 | 1:1 | 1:2 | UA | Combusted | 400 | Sol-gel 400 |
| 1:2 | 1:1 | 1:2 | UA | Combusted | 500 | Sol-gel 500 |
| 1:2 | 1:1 | 1:2 | UA | Combusted | 600 | Sol-gel 600 |
| UA 1:2 | 1:1 | 1:2 | UA | Combusted | 700 | Sol-gel 700 |
| 1:2 | 1:1 | 1:2 | UA | Combusted | 800 | Sol-gel 800 |
| 1:2 | 1:1 | 1:2 | 1 | Combusted | 500 | Sol-gel pH 1 |
| 1:2 | 1:1 | 1:2 | 1.25 | Combusted | 500 | Sol-gel pH 1.25 |
| 1:2 | 1:1 | 1:2 | 1.5 | Combusted | 500 | Sol-gel pH 1.5 |
| 1:2 | 1:1 | 1:2 | 3 | Combusted | 500 | Sol-gel pH 3 |
| 1:2 | 1:1 | 1:2 | 4 | Combusted | 500 | Sol-gel pH 4 |
| 1.05:2 | 1:2 | 1:0 | UA | Drying | 500 | Sol-gel CA2 |

**Table 3.3:** Masses of reagents used for sol-gel synthesis in this thesis. Note, the mass of $Mn(NO_3)_2$ has been omitted due it being added from standardised solutions, with different concentrations.

| Mass finished sample [g] | Molar ratio $Li^+ : Mn_2^+$ | Molar ratio MI CA [g] | Molar ratio CA EG [g] | Mass $LiNO_3$ [g] | Mass CA [g] | Mass EG [g] |
|---|---|---|---|---|---|---|
| 3 | 1:1 | 1:1 | 1:2 | 1.9051 | 9.5626 | 6.1786 |
| 3 | 1.05:2 | 1.05:2 | 1:0 | 2.0004 | 9.7219 | 0 |
| 10 | 1:05:2 | 1.05:2 | 1:0 | 4.0008 | 32.4065 | 0 |

XRD measurements was obtained for all samples, further SEM images was obtained from sol-gel 800 (before milling) and sol-gel CA2. Sol-gel CA2 was selected for further electrochemical testing and EDS surface analysis.

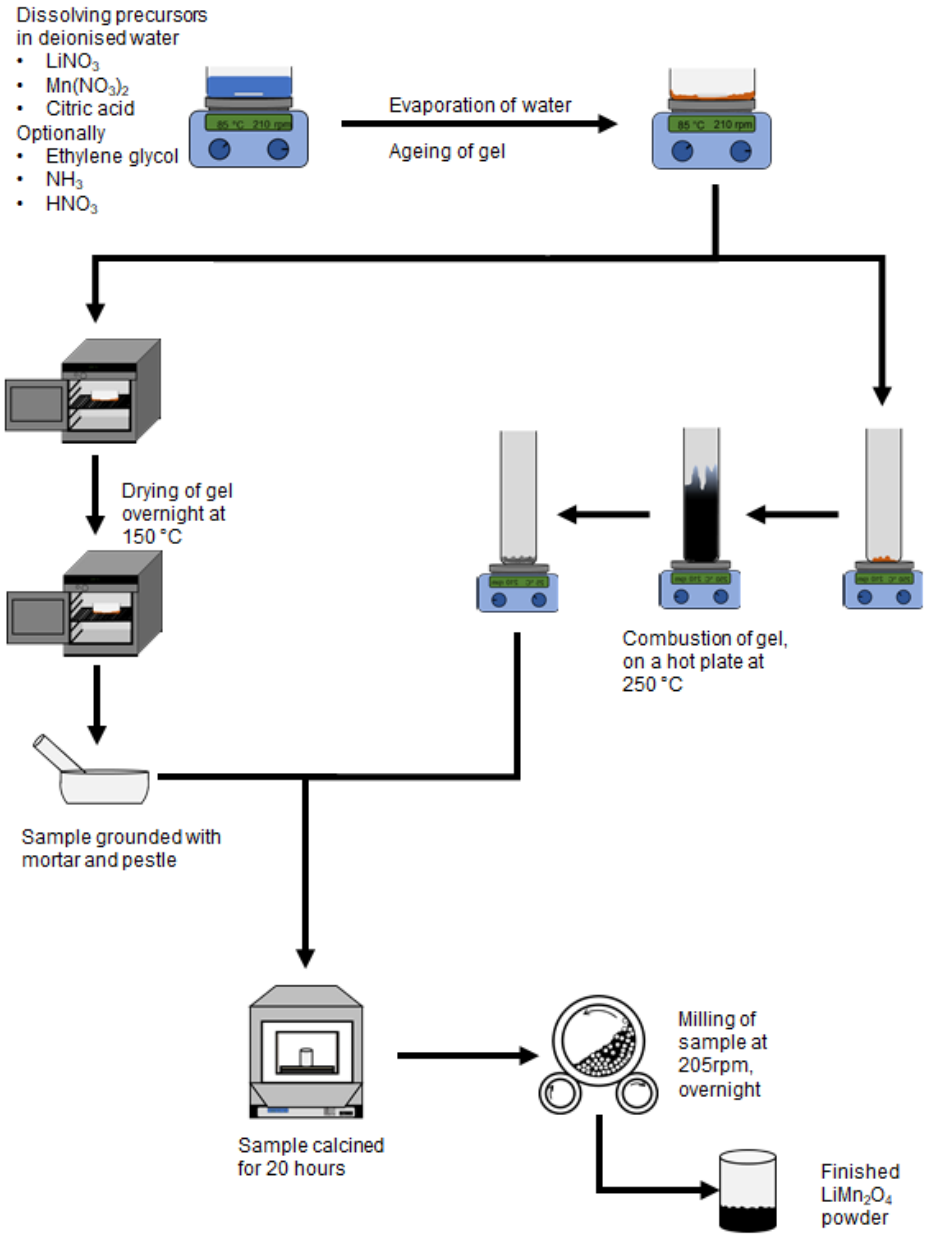


**Figure 3.2:** Schematic illustration of the sol-gel procedure for synthesis of $LiMn_2O_4$, and the order the of steps. The diverging line indicates difference in the treatment of different samples.

### 3.1.3 Coprecipitation

Synthesis of $LiMn_2O_4$ through coprecipitation followed in general the following procedure. Precipitation of $MnCO_3$, filtration, drying/heat treatment, mixing with $Li^+$ followed by calcination. The molar ratios, mixing techniques was based on work done by Xiao et al. [18], Zhou et al [61] and Robinson and Koening [16].

Coprecipitation of $MnCO_3$ was done by mixing a solutions of $Mn^{2+}$ salt and $NH_4HCO_3$. $Mn(CH_3CO_2)_2 \cdot 4H_2O$ or $Mn(NO_3)_2$ ( standardised solution as described in Section 3.1.1) was used as $Mn^{2+}$ source, mainly dependent on availability. Both $Mn^{2+}$ and $NH_4HCO_3$ was completely dissolved before mixing. Precipitation started by rapid addition of $NH_4HCO_3$ to the $Mn^{2+}$ solution, the solution turned instantly form transparent pink to white. The solution was left to precipitate for 20 minutes under stirring on a hot plate at 35 °C. Separation of solid precipitate was done through vacuum filtration with a Whatman filter paper (589/2 grade, ashless / blue ribbon). Precipitate was washed once with deionised water and once with 96 % ethanol.

Separated solid was turned into either $MnO_2$ or $MnCO_3$ intermediate. $MnO_2$ was obtained through heat treatment of sample at 400 °C for 4 hours. $MnCO_3$ was obtained by drying sample at 120 °C.

Both intermediate ($MnCO_3$ or $MnO_2$) and $LiNO_3$, were dried overnight at 95 °C. All mixing was done with an excess molar lithium ratio of 5 %. Three different mixing techniques were attempted:

- Mixing intermediate with $LiNO_3$ by hand with mortar and pestle for 5 minutes, in a small amount of isopropanole.
- Wet ball milling at 205 rpm for 1 hour in isopropanol, with Zirconia 5 mm diameter (Nikkato Corporation, 95 % $ZrO_2$, 5 % $Y_2O_3$) milling balls. Followed by drying in a rotavapor.
- Dissolving $LiNO_3$ in 40mL deionised water, followed by dispersion of intermediate. Sample left to dry under stirring on a hot plate for 24 hours at 40 °C. This was followed by manual grounding by mortar and pestle for 5 minutes. Note this sample was milled after calcination.

Mixture of intermediate and $LiNO_3$ was calcined for 10 hours at either 700 °C or 600 °C. An full overview over the process is shown in Figure 3.3.

A full overview of the different samples, synthesis parameters, mixing technique and calcination temperature, can be found in Table 3.4. XRD measurements was done for all samples. SEM images were obtained for sample precipitate $MnCO_3$ mortar and pestle 75 mL was and precipitate Mn̨O2 water dispersion. Precipitate Mn̨O2 water dispersion were selected for further EDS and electrochemical analysis.

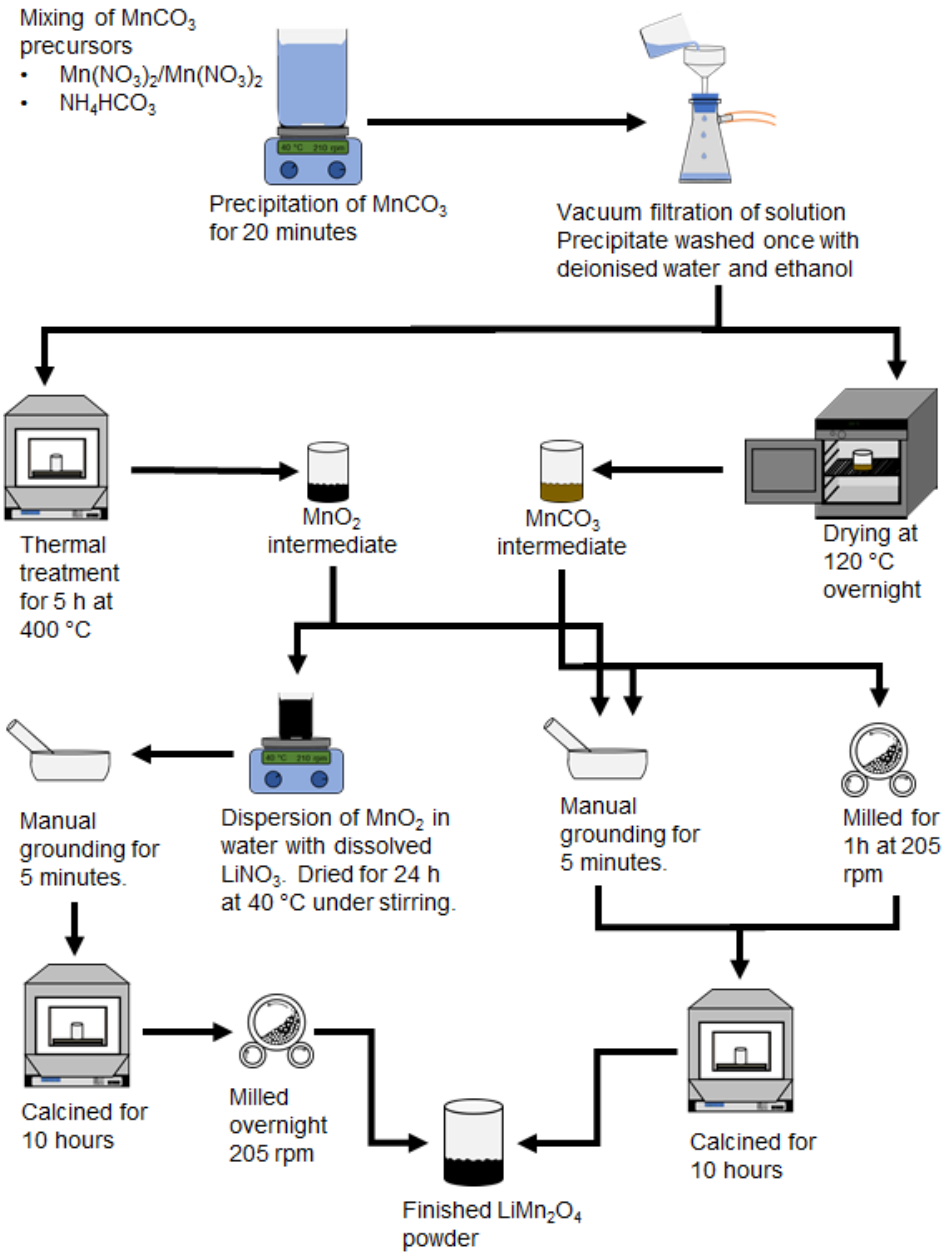


**Figure 3.3:** Schematic illustration of synthesis of $LiMn_2O_4$ through coprecipitation. The lines show the order of the steps. Diverging lines indicates difference in sample handling.

**Table 3.4:** Different parameters used for the synthesis of $LiMn_2O_4$ through coprecipitation and corresponding sample id.

| $Mn^{2+}$ precursor and mass of precursor (g) | Mass NH4HCO3 | VH20 (mL) | $MnO_2$/ $MnCO_3$ | Mixing technique | Calc. T (C) | Sample id. |
|---|---|---|---|---|---|---|
| $Mn(CH_2CO_2)_2$ 6.7070 g | 2.7520 | 75 | $MnO_2$ | Mortar and pestle | 700 | Precipitate $MnO_2$ mortar and pestle |
| $Mn(CH_2CO_2)_2$ 6.7070 g | 2.7520 | 75 | $MnCO_3$ | Mortar and pestle | 700 | Precipitate $MnCO_3$ mortar and pestle, 75 mL |
| $Mn(CH_2CO_2)_2$ 6.7070 g | 2.7520 | 500 | $MnCO_3$ | Mortar and pestle | 700 | Precipitate $MnCO_3$ mortar and pestle, 500 mL |
| $Mn(CH_2CO_2)_2$ 6.7081 g | 2.7618 | 75 | $MnCO_3$ | Ball milling | 700 | Precipitate $MnCO_3$ ball milling, 75 mL |
| $Mn(CH_2CO_2)_2$ 6.7097 g | 2.7590 | 500 | $MnCO_3$ | Ball milling | 700 | Precipitate $MnCO_3$ ball milling 500 mL |
| $Mn(NO_3)_2$ 16. 7980 g | 16.6627 | 800 | $MnO_2$ | Water dispersion with dissolved $LiNO_3$, followed by mortar and pestle. | 600 | Precipitate $MnO_2$ water dispersion |

## 3.2 Characterisation

### 3.2.1 X-ray diffraction

X-ray diffraction was done with a Bruker D8 focus X-ray Diffractometer (D8 focus). The instrument utilise a Cu K$\alpha$ radiation source with a wavelength of 1.54  and a LynxEye ™ SuperSpeed Detector. All analysis in D8 focus used a constant slit of 1 mm, and was done from 15 to 95 $2\theta$ with 0.04 $2\theta$ steps.

Analysis of $LiMn_2O_4$ and other powder was done in standard sample holders. Cathode casts was analysed in a deep sample holder on top of a small amount of amorphous modelling clay, to ensure correct height, this was done for current collector without cathode cast, non-cycled cast and cathode cast after electrochemical measurements.

Phase analysis was done with comparing the peaks with reference samples for the PDF+4 2019 database [111] in the EVA software [112].

### 3.2.2 Scanning electron microscopy and Energy-dispersive X-ray spectroscopy

All SEM images was taken in an Zeiss Supra 55VP apparatus with a thermal field emission gun and a Everhart-Thornley Secondary Electron Detector. All images was taken with an accelerating voltage of 10 kV and a working distance of 10 - 13 mm. EDX scanning and mapping was done under high voltage conditions, with a EDAX, OCTANE PRO -A detector. Analysis of $LiMn_2O_4$ particles and prepared cathodes both cycled and non-cycled was done alongside analysis of the cross section of a cathode.

All samples was attached to conductive carbon tape, either on top or on the side of a metallic pin, as shown in Figure 3.4. Analysis of following $LiMn_2O_4$ powder from, sol-gel 800 (before ball milling), sol-gel CA2, precipitate $MnCO_3$ mortar and pestle 75 mL and precipitate $MnO_2$ water dispersion. With the exception of sol-gel 800, all $LiMn_2O_4$ powder samples was dispersed in small amounts of 96 % ethanol in a ultrasonic bath, to crush soft agglomerates. A single drop of the dispersion was added to the top of the carbon tape, and allowed to dry. Powder from sol-gel 800 where applied directly to the top. Excess sample were removed by blowing air onto the tape. Analysis of cathode casts was done by cutting a small slice of it, and applying it to the carbon tape. Analysis of both top of cast and cross section between the cast and current collector was done. To inspect the top of the cast, the slice was applied to the top of the metallic pin. The cross section was inspected by applying the cast to the side of the metallic pin, with the cross section pointing up. Prepared samples was inserted into the analysis chamber which was evacuated.

### 3.2.3 Surface analysis

Surface analysis was done in a Tristar 3000 Surface Area and Porosity analyser. Samples with a mass between 0.0939 grams and 0.1302 grams was degassed overnight at 120 °C. $N_2$ was used as adsorbing gas at 77 K. The overall surface area was found using the BET-equation 2.20.

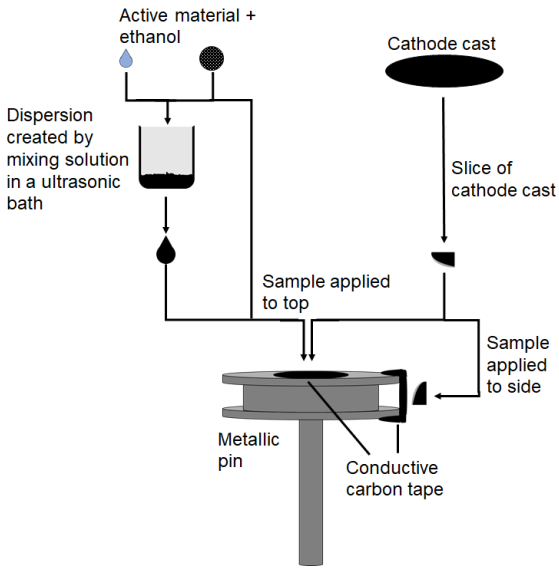


**Figure 3.4:** Sample preparation for SEM-analysis

## 3.3 Half cell manufacture

Components used for half cell assembly is shown in Table 3.5.

**Table 3.5:** Components used for assembly of lithium half cells

| Component | Composition and additional information | Producer |
|---|---|---|
| Current collector | Aluminum foil, 0.025 mm thick<br>99.45 % metal basis | Alfa aesar |
| Electrolyte | 1 M Lithum hexaflourphosphate ($LiPF_6$)<br>on 50:50 by volume ethylene carbonate (EC)<br>and diethylcarbonate (DC).<br>Battery grade purity, $<$ 15 ppm H20,<br>$<$ 50 ppm HF. | Sigma-Aldrich |
| Separator | Celgard ™2320, 20 $\mu$m Micropourous<br>Trilayer Membrane (PP/PE/PP) | Celgard R |
| Anode | Lithium foil 99 % metal basis,<br>0.75 mm thick | Alfa aesar |
| Casing, spacer,<br>rubber ring | CR2016 set | Hoshen Corp. |

### 3.3.1 Preparation of working electrode

Working electrodes were made by tape casting a slurry onto a aluminium foil current collector. Prepared $LiMn_2O_4$-samples was mixed with carbon black to increase conductivity, PVDF was used as binder and NEP used as solvent. Carbon black and PVDF was both dried overnight at 120 °C under vacuum. PVDF was dissolved in NEP, by mixing the components in a 1:20 ratio by mass, and left to stir overnight. All components was mixed in a steel jar, which was shacked in a Retsch Mixer Mill MM 400 (Shaker mill) for 30 minutes with a frequency of 30 Hz. A slice of the current collector was cleaned with 96 % ethanol and spread evenly to ensure a homogeneous surface without any air bobbles present. The mixed slurry was casted onto the current collector with a RK K-Control Coater model 101 (Tape caster) with a thickness of 200 $\mu$m. Prepared cast was dried overnight at 60 °C, followed by 3 hours at 120 °C under vacuum.

Two different compositions was used to assemble the cathode casts, one with 5 % PVDF by mass and one with 10 % PVDF by mass. Mass of material and % by weight composition can be found in Table 3.6 an 3.7.

**Table 3.6:** Mass used to assemble cathode cast with 5 % weight PVDF by mass, alongside wt % of components

| | Mass[g] | wt. % wet sample | wt. % solid sample |
|---|---|---|---|
| Active material | 0.5 | 28.8 | 85 |
| Carbon black | 0.059 | 3.4 | 10 |
| PVDF | 0.029 | 1.7 | 5 |
| PVDF in NEP | 0.585 | - | - |
| Ekstra NEP | 0.588 | 66.1 | - |

**Table 3.7:** Mass used to assemble cathode cast with 10 % weight PVDF by mass, alongside wt % of components

| | Mass (g) | wt. % wet sample | wt. % solid sample |
|---|---|---|---|
| Active material | 0.5 | 26.7 | 80 |
| Carbon black | 0.0625 | 3.3 | 10 |
| PVDF | 0.0625 | 3.3 | 10 |
| PVDF in NEP | 1.25 | - | - |
| Ekstra NEP | 0.0625 | 66.7 | - |

### 3.3.2 Half cell assembly

Circular cathodes with a diameter of 1 6mm were cut from the cast, weighed and transferred to a Mbraun glove box. Assembly of 2016 (diameter 20 mm, height 1.6 mm) coin cells was done in an inert argon atmosphere with $P_{H2O}$ and $P_{O2} < 0.1$ PPM. The cells were assembled according to the following set-up, also shown in Figure 3.5. The rubber ring was inserted into the bottom casing followed by the cathode. 20 $\mu$L of 1 M $LiPF_6$ in a 50:50 ethylene carbonate and diethylcarbonate by volume electrolyte solution was added to the top of

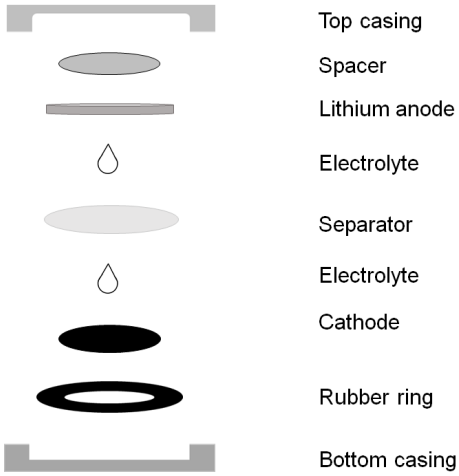


**Figure 3.5:** Schematic of the coin assembly process, in the order the components are added, from bottom to top.

the cathode. 18mm diameter of separator circular sheets was put on top,followed by an additional 20 $\mu$L of electrolyte. The counter electrode was prepared by cutting a 16 mm diameter circular piece from the lithium foil. The spacer was added, followed by the top casing. The cells were hermetically sealed in Hoshen Automatic Coin Cell Crimper.

### 3.3.3 Coin cell dissaembly

Some cycled cells was dissembled to study the effect cycling had on the active material and cathode. Handling was done in an inert argon atmosphere with $P_{H2O}$ and $P_{O2}$ <0.1 PPM, in Mbraun glove box. A Hoshen Corp Coin Cell Disassembling Tool was used to open the coin cells. Cycled cathodes was then washed in a diethylcarbonate solution to remove traces of electrolyte.

### 3.3.4 Electrochemical measurements

**Table 3.8:** Cycling programmes used in this thesis.

| Programe | C - rate | Number of cycles |
|---|---|---|
| Rate | C/20 | 6 |
| | C/10 | 5 |
| | C/5 | 5 |
| | C/20 | 5 |
| Life | C/2 | 200 |

All measurements was done on a LAHNE CT2001A-Battery testing station with a current density of 10 mAh. All cycling was done on a room with a controlled temperature

of 20 °C. The half cells were allowed to relax for 12 hours before cycling started. Two different cycling programs were used, shown in Table 3.8. However, no useful results were obtained from the life assessment.

# Chapter 4

# Results

## 4.1 Phase Characterisation and surface area

This section covers the phase analysis of the phase pure samples, alongside X-ray diffraction obtained from $MnCO_3$ and $MnO_2$ intermediates. Reference samples used for phase characterisation is shown in Table 4.1.

**Table 4.1:** Reference samples used in this thesis for phase analysis and Rietveld refinement, all from the PDF-4 +2019 database [111].

| Compound | Number | Symmetry | Space group |
|---|---|---|---|
| $LiMn_2O_4$ | 00-035-0782 | Cubic | Fd-3m(227) |
| $Mn_2O_3$ | 00-041-1442 | Cubic | Ia-3(206) |
| $MnCO_3$ | 00-044-1472 | Rhombohedral | R-3c(167) |

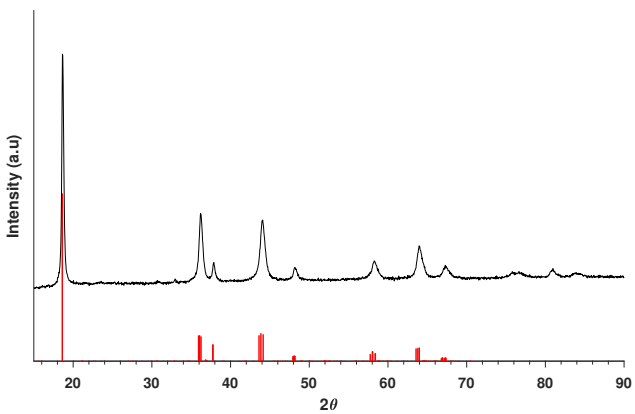


**Figure 4.1:** X-ray diffracotgram for sample sol-gel CA2, red lines are $LiMn_2O_4$ reference sample.

The X-ray diffractogram of sample sol-gel CA2 is shown in Figure 4.1. The measurements shown clear narrow peaks, characteristic for $LiMn_2O_4$. There is however a single small peak around 33 $2\theta$, which indicates the presence of a $Mn_2O_3$ secondary phase.

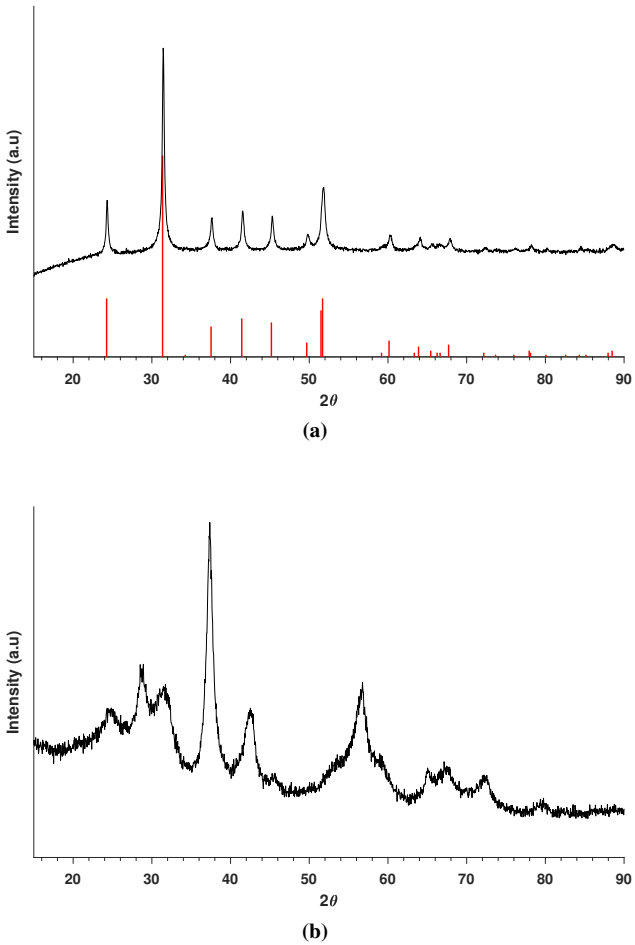


**Figure 4.2:** XRD measurement of intermediates for coprecipitation. (a) is $MnCO_3$ with red lines representing $MnCO_3$ reference sample. (b) is the diffractogram of $MnO_2$

Figure 4.2 shows X-ray diffraction measurements of the intermediates for synthesis of $LiMn_2O_4$ through coprecipitation. The diffractogram of $MnCO_3$ (Figure 4.2a) shows a crystalline phase, which fits well to the $MnCO_3$-reference sample. The peaks in the diffractogram of $MnO_2$ (Figure 4.2b), have far less characteristic peaks and far more distinct background. No fitting reference sample for $MnO_2$ was found, attributed to the general tendency of poor quality diffractograms with diffuse and broad peaks and high background [113].

The diffractogram of precipitate $MnO_2$ water dispersion is shown in Figure 4.3. All

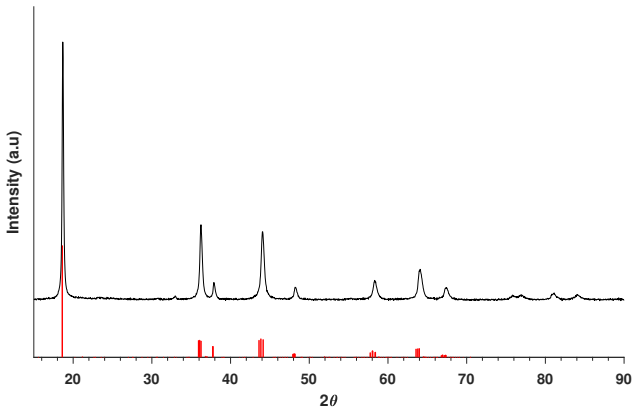


**Figure 4.3:** XRD measurement of sample precipitate $MnO_2$ water dispersion. Red lines are $LiMn_2O_4$ reference sample.

characteristic peaks for $LiMn_2O_4$ can be found in the sample. The small peaks around 33 $2\theta$, which indicates the presence of a small amount of a secondary $Mn_2O_3$ phase. The surface area for sol-gel CA2 and precipitate $MnO_2$ water dispersion found through the BET isotherm is shown in Table 4.2. The measured surface area between the samples are around the same. The measured surface area indicates an average particle size below 1 $\mu$m [95].

**Table 4.2:** Measured surface area of samples used for electrochemical cycling and Gaussian error in measurement.

| Sample | Surface area |
|---|---|
| Sol-gel CA2 | $8.1063 \pm 0.2186$ |
| Precipitate $MnO_2$ water dispersion | $7.8714 \pm 0.1756$ |

## 4.2 Particle morphology

This section presents the particle morphology of finished $LiMn_2O_4$ powder from procedure sol-gel 800 (Figure 4.4a and 4.4c), precipitate $MnCO_3$ mortar and pestle 75 mL (Figure 4.4b and 4.4d), sol-gel CA2 (Figure 4.5a, 4.5c and 4.5e) and precipitate $MnO_2$ water dispersion (Figure 4.5b, 4.5d and 4.5f).

The SEM image of sol-gel 800 and precipitate $MnCO_3$ mortar and pestle 75 mL shown in figure 4.4 shows two distinctly different morphologies. Sol-gel 800 have a rough surface in the overview image (Figure 4.4a) which makes the sample appear foam like. he larger magnification of sol-gel 800 (Figure 4.4c) shows that the particle is composed of several smaller defined particles with a variety of particle sizes. The particles from precipitate $MnCO_3$ mortar and pestle 75 mL (Figure 4.4a and Figure 4.4a) have a much more distinct morphology with particles of similar size and shape. All particles here are highly porous

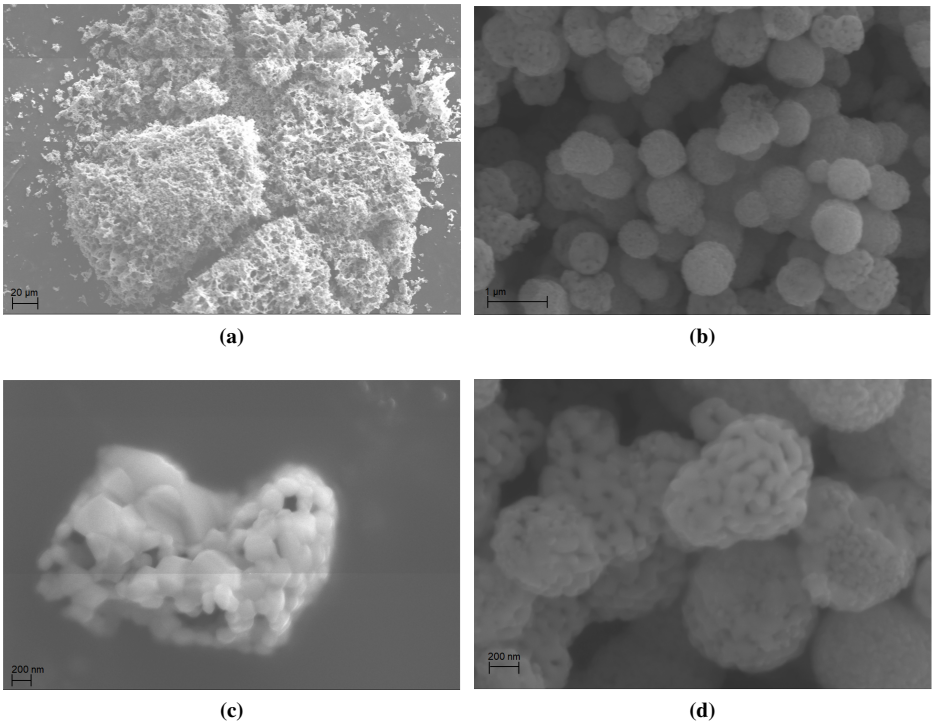


**Figure 4.4:** SEM image of sol-gel 800 (a) and (c) and precipitated $MnCO_3$ mortar and pestle 75 mL (b) and (d). Note magnification differs between images and samples.

with an overall ellipsoid morphology. While some deviations does appear, it seems to be the result of two or more ellipsoid particles which have grown together.

The morphology of sol-gel CA2 and precipitate $MnO_2$ water dispersion appears quite similar, as shown in Figure 4.5. Both samples result in irregularly shaped particles with a wide size distribution. The SEM images of sol-gel CA2 (shown in Figure 4.5a, 4.5c and 4.5e) shows particles with a large surface area and highly irregular shapes. All particles appear as assemblies of many smaller particles, grown together in a random pattern. There is also a wide size distribution among the smaller particles, ranging from below 100 nm up to around 500 nm The morphology of particles from precipitate $MnO_2$ water dispersion (shown in Figure 4.5b, 4.5d and 4.5e) appears as mixture of different types of morphologies. Either as large compact shapes with clearly defined edges, a highly irregular open foam like shape or a mixture if the two. The size among the observed particles also shown a wide variety as some of the larges compact shapes have a length of several $\mu$m.

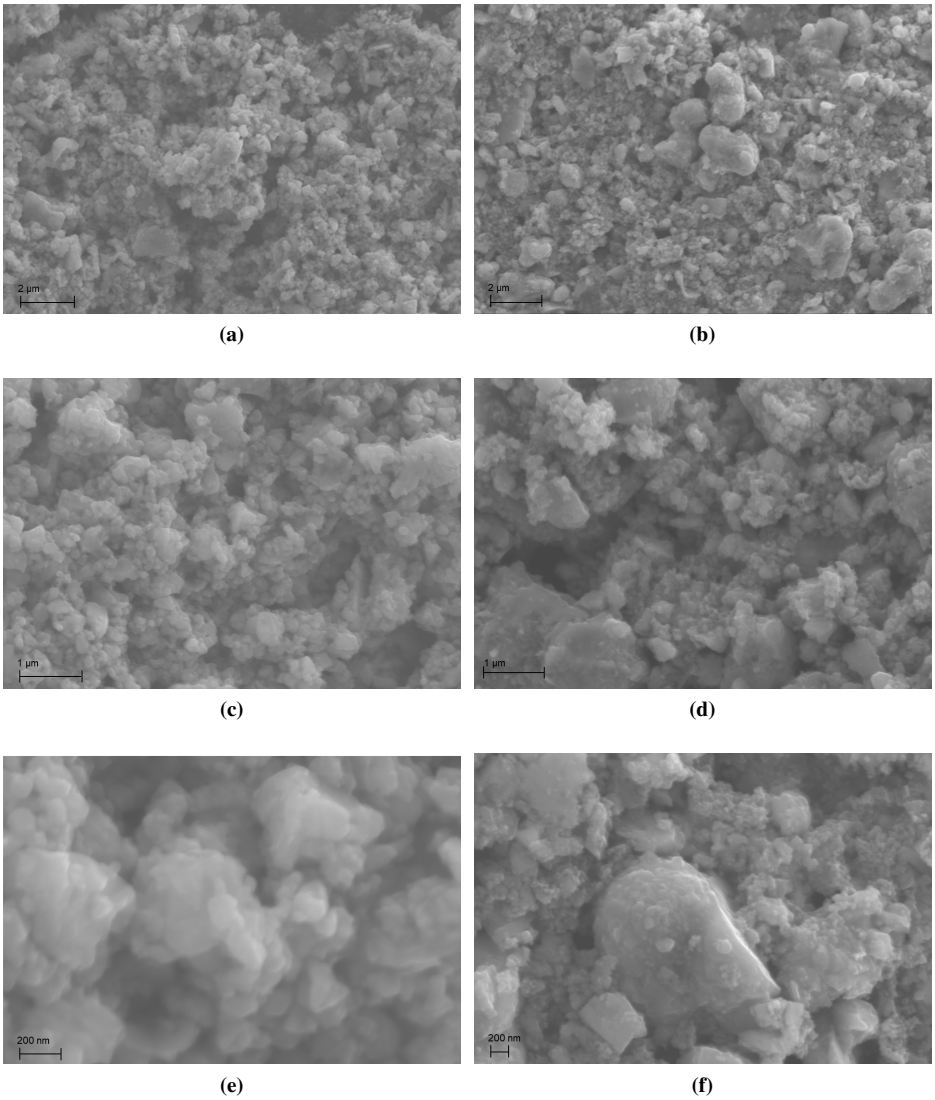


**Figure 4.5:** SEM images of $LiMn_2O_4$ particles. Image (a), (c) and (e) is from sample sol-gel CA2, while (b), (d) and (e) is from sample precipitate $MnO_2$ water dispersion. Note, magnification is not the same between the images.

## 4.3 Electrochemical analysis, phase analysis and morphology of cathode cast.

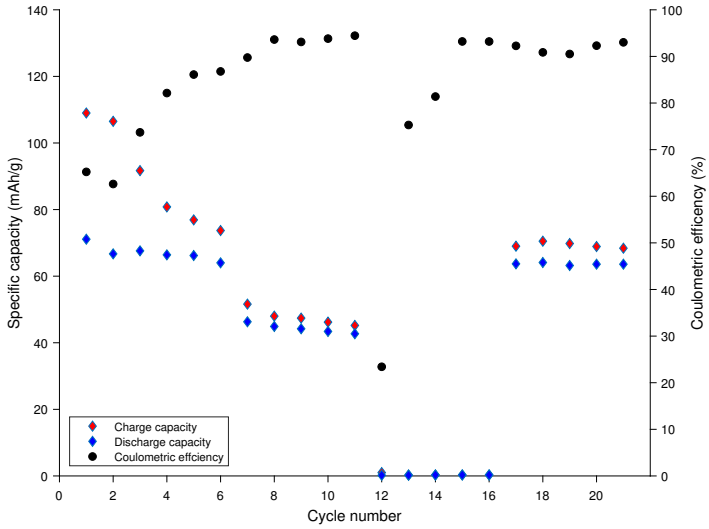


**Figure 4.6:** Galvanostatic cycling of half-cell assembled from $LiMn_2O_4$ obtained from sol-gel CA2 procedure, with a 5 wt.% cathode cast.

This section covers obtained electrochemical data and changes in cathodes before and after cycling. First the results obtained form cast with 5 wt. % PVDF is presented, for $LiMn_2O_4$ obtained from both sol-gel CA2 and precipitate $MnO_2$ water dispersion, followed by analysis of the cathode casts before and after cycling. Then the electrochemical properties of cast with 10 wt. % PVDF is presented. A full overview of cycling properties of all cells presented can be found in Table A.2, in Appendix A.3.

The rate capability galvanostatic cycling sol-gel CA2 with 5 wt. % PVDF. Figure 4.6, shows a low initial capacity of 71.1 mAh/g during the first discharge. There is a noticeable loss of discharge capacity with each cycle. Between the different C-rates, switching from C/20 to C/10 resulted in drop in available discharge capacity of around 33 %. At cycling rate C/5 there is next to no available capacity in the cell. The charge-discharge curves for the same cell shown in Figure 4.7 shows that there is a large polarization present between corresponding charge and discharge cycles. Which results in a difference in terminal voltage between charge and discharge, and a lower overall energy efficiency. The discharge curve consist of two plateaus, characteristic for $LiMn_2O_4$ [5], which is present to a far lower degree for the charge curves. The last five cycles at C/20 shows rather stable cycle capacity around 63 mAh/g, close to the initial values. The differential capacity analysis of the first and last cycle, Figure 4.8, shows two clear peaks around 4 and 4.15 V for charge and 4.1 and 3.95 V for discharge. During cycling the size of the peaks have been reduced and, and a the dQ/dV for discharge have been moved to a lower voltage. No peaks indicating other

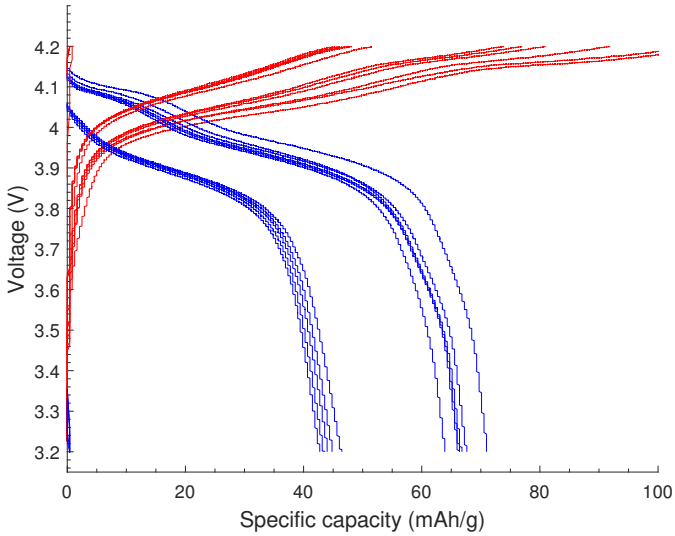


**(a)**

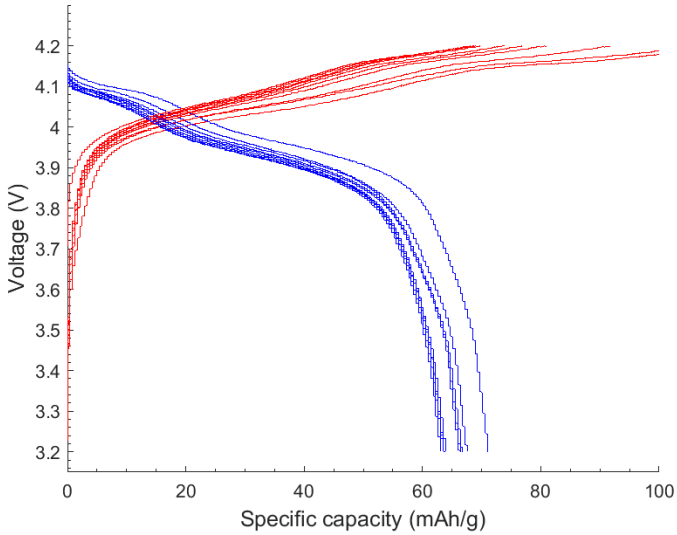


**(b)**

**Figure 4.7:** Charge-discharge curves for chLiMn2O4 from sol-gel CA2 sample, with 5 wt. % PVDF. (a) is cycle 1-16, (b) is cycle 1-6 and 17-21.

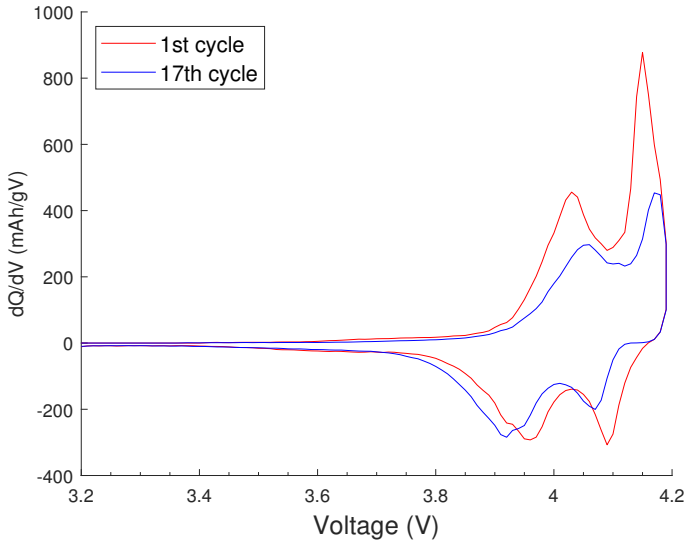


**Figure 4.8:** Differential capacity analysis of first and last cycle of $LiMn_2O_4$ obtained from sol-gel CA2 procedure, with cast containing 5 wt. % PVDF.

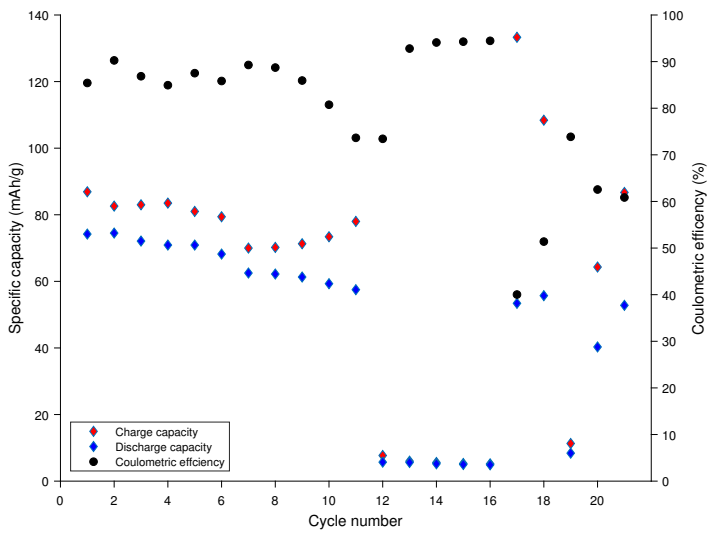


**Figure 4.9:** Galvanostatic cycling of cathode assembled with product obtained from precipitate $MnO_2$ water dispersion procedure and 5 wt % PVDF in cast.

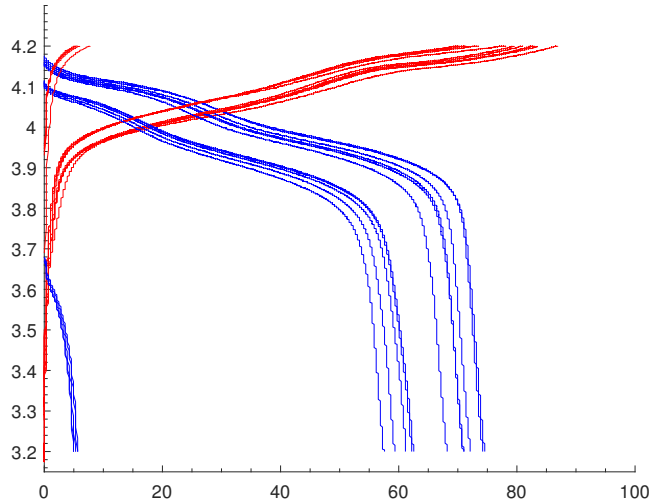


**(a)**

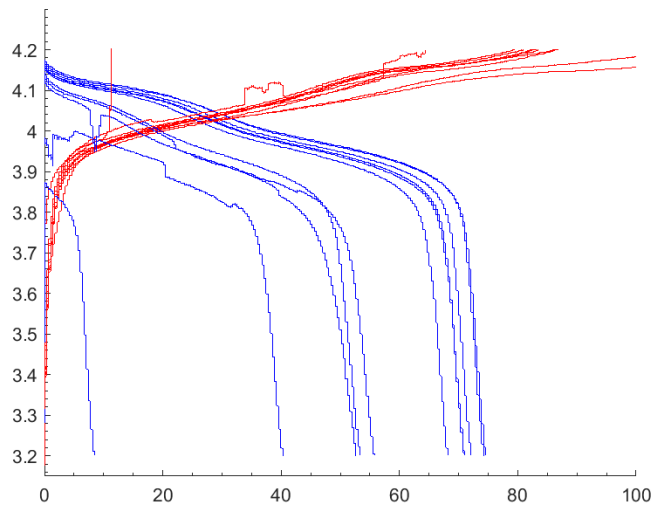


**(b)**

**Figure 4.10:** Charge-discharge curves for $LiMn_2O_4$ obtained from precipitate $MnO_2$ water dispersion procedure with 5 wt. % PVDF in cast. Cycle 1-16 is shown in (a), while cycle 1-6 and cycle (17-21) is shown in (b). Note in figure (b), curve with lowest capacity is cycle 19, while cycle 21 have regions with sudden changes in voltage.

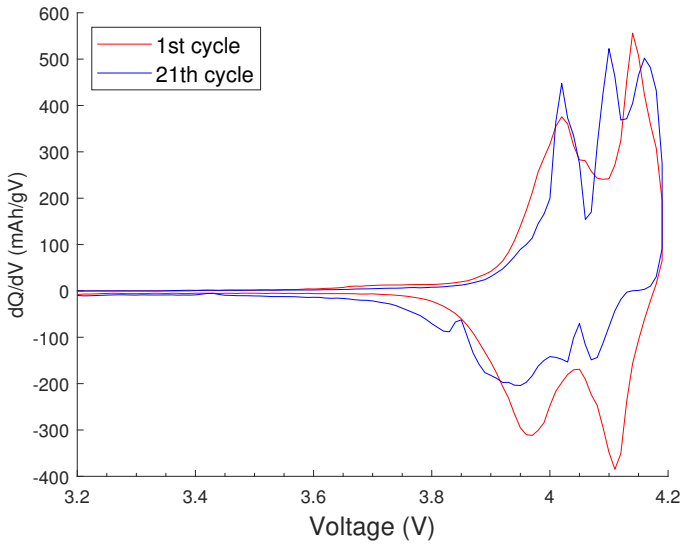


**Figure 4.11:** Differential capacity analysis of first and last cycle for half cell assembled with $LiMn_2O_4$ from precipitate $MnO_2$ water dispersion procedure with 5 wt. % PVDF in cast.

reactions are present.

The galvanostatic cycling of half-cells obtained from precipitate $MnO_2$ showed low but stable initial capacity for the first 16 cycles. As shown in Figure 4.9, there is little change in available discharge capacity when the C-rate changes from C/20 to C/10, and even a small amount of discharge capacity is available at C/5. However, there is a large derviation amoung the 5 last cycles. Cycle 17 is a rather sharp drop in available charge and discharge capacity, while the capacity increased for the last two cycles. The charge-discharge curves shown in Figure 4.10 shows fairly stable behaviour during the first 16 cycles. However as shown in Figure 4.10b the charge discharge curves during the last five cycles have large deviations from each other, with sudden voltage changes present in the last cycle. The sudden changes in cell voltage is results in changes in the differential capacity analysis (Figure 4.11), as there is sudden peaks present in the dQ/dV curve as an result.

To analyse if difference in the $LiMn_2O_4$ cathode cast could be observed before and after cycling, dissembled cells were analysed through XRD and SEM, and compared with non-cycled cast. The diffractograms of cathode casts made from sol-gel CA2 and precipitate $MnO_2$ water dispersion with 5 % wt. PVDF, shown in Figure 4.12, shows high peaks around 27, 44.5, 65 and 78.2 $2\theta$, which is attributed to the current collector. All new peaks fit with peaks intruduced by the current collector. Both samples shows an decrease in intensity relatively to the current collector after cycling, but no shift or the appearance of new peaks or disappearance of excising peaks. The change in relative heigth between cathode casts can be attributed to a loss of mass in the cast during cycling and handling.

Sem images of cathode cast, both cycled and non-cycled, shown in Figure 4.13 shows little difference in particle morphology before and after cycling. Both the cast made from

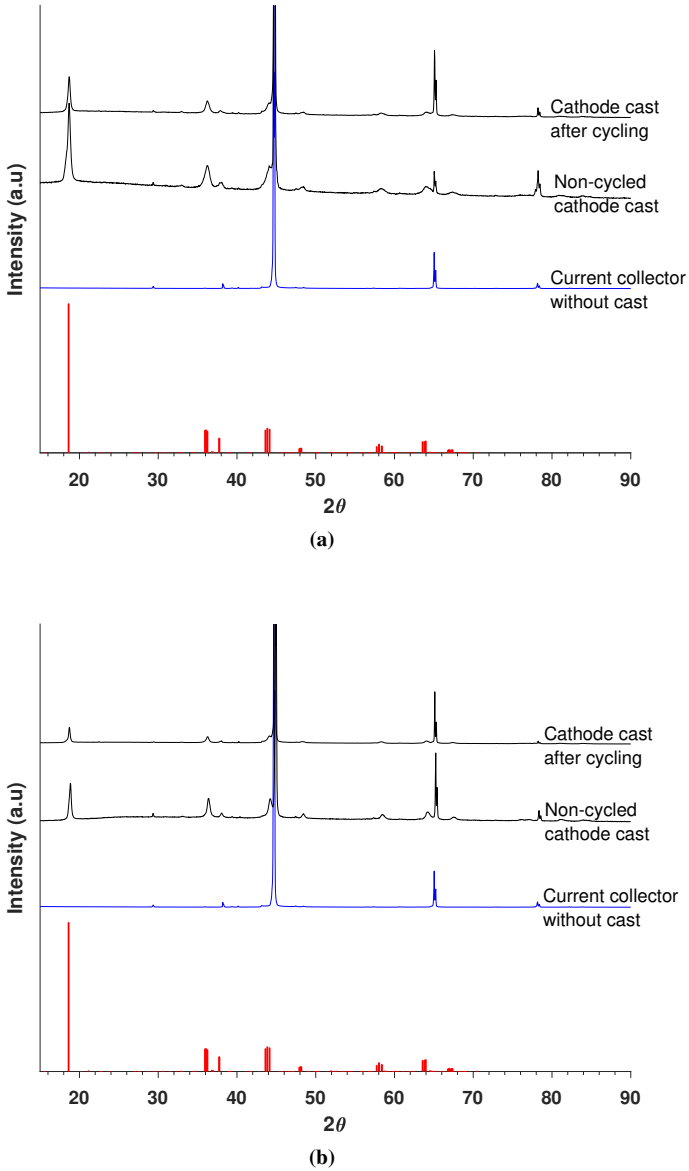


**Figure 4.12:** XRD measurements of cathode casts both cycled and non-cycled alongside LiMn2O4 reference sample (red lines) and current collector without cast (blue line). (a) is cathodes made from sample sol-gel CA2, while (b) is casts made from sample precipitate $MnO_2$. Note, intensity of all diffractograms have been normalised with regards to each other.

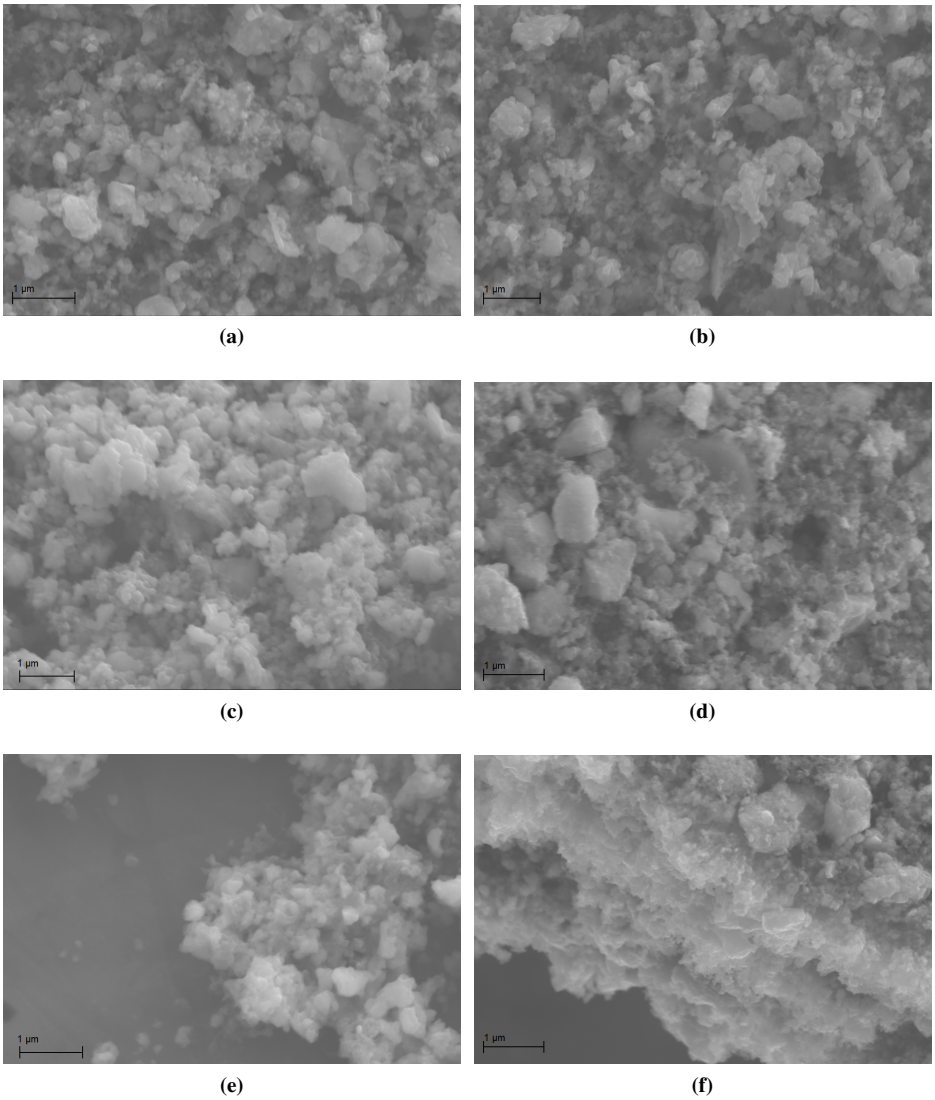


**Figure 4.13:** SEM images of cathode casts from product made through sol-gel CA2 procedure ((a), (c) and (e)) and from precipitate $MnO_2$ water dispersion, both with 5 % wt. PVDF. (a) and (b) are top of cast before cycling, while (c), (d), (e) and (f) is after the cathode have been electrochemically cycled. Here (c) and (d) are the surface of the cast and (e) and (f) is form regions where the current collector can be seen. Note, magnification is not the same between images.

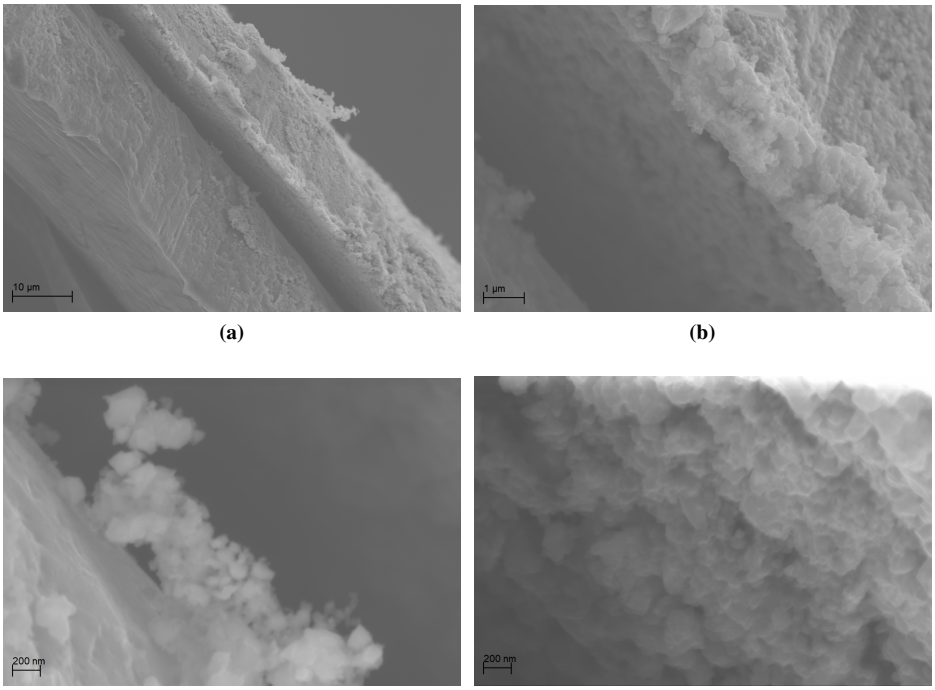


**(a)** **(b)**

**(c)** **(d)**

**Figure 4.14:** SEM image of cross section of cathode cast non-cycled made from $LiMn_2O_4$ obtained from sol-gel CA2, with 5 % PVDF in cast. Note images are not of the same magnitude. (a) and (b) gives and overview of a void present in the cross section, (c) shows a small part of the cathode cast still present on the surface of the current collector, while (d) shows the underside of the cathode cast.

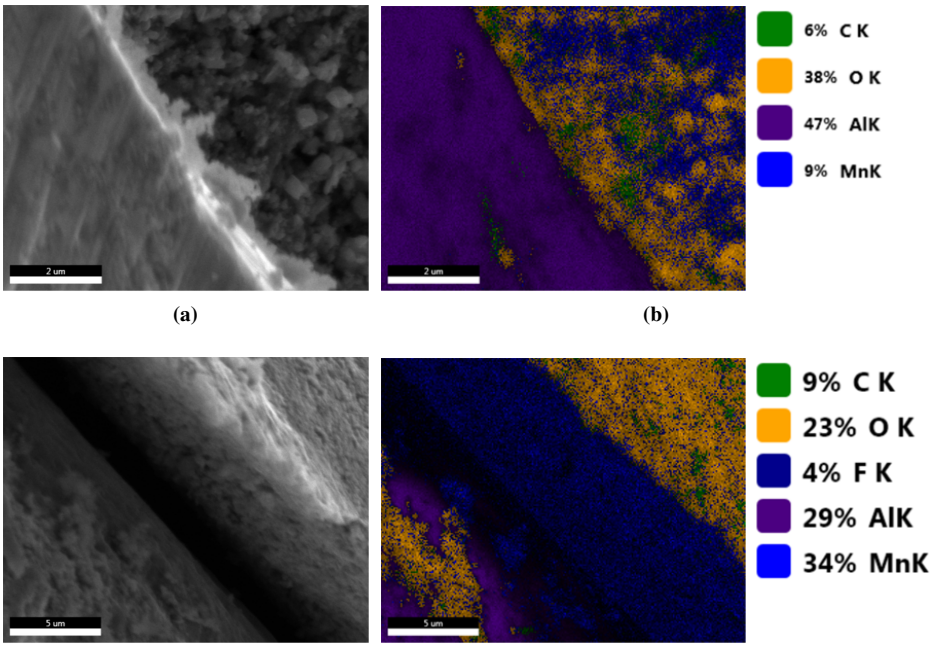


**Figure 4.15:** EDS mapping of cross section of cathode cast made from product from sol-gel CA2 with 5 % wt. PVDF. Image (a) is image region of location where the current collector and cathode cast is connected, while (b) is elemental mapping of said area. (c) is image region of location where a void is present between current collector and cathode cast and (d) is elemental map of said area.

sol-gel CA2 and precipitate $MnO_2$ water dispersion does not show any large difference in general surface composition between non-cycled. Any difference in particle morphology or size is hard to analyse due to the inhomogeneity of the initial material. The only observable difference was the regions where the cathode cast had been removed (Figure 4.13e and 4.13f). The edge shown for precipitate $MnO_2$ water dispersion (Figure 4.13f) have a far smoother side than the overall surface of the cycled cathode cast. While the cast assembled from sol-gel CA2, the region where the current collector could be seen, contained particles with much the same size and shape as before.

The SEM images (Figure 4.14) of the cross section of a non-cycled cathode cast made from the sol-gel CA2 procedure with 5 % wt. PVDF showed a void between the . current collector and the cathode cast. The void is fairly large with a length of around 5 $\mu$m. Some small amounts of the cathode cast is present on top of the current collector as shown in Figure 4.14c. The underside of the cast appears fairly ordered, as shown in Figure 4.14d. The EDS mapping done on two points at this cross section, shown in Figure 4.15, shows some difference in the regions where the cast have loosened and not. Most notably the EDS mapping in Figure 4.15d shown far more oxygen, on top of the current collector, compared to the EDS mapping shown in Figure 4.15b. Further fluoride is only detected on

the underside of the cathode cast and between the current collector and the cast.

To ensure better connection between $LiMn_2O_4$ cathode cast and current collector, the fraction of PVDF was increased to 10 wt. %. This was done with $LiMn_2O_4$ from both sol-gel CA2 and precipitate $MnO_2$ water dispersion.

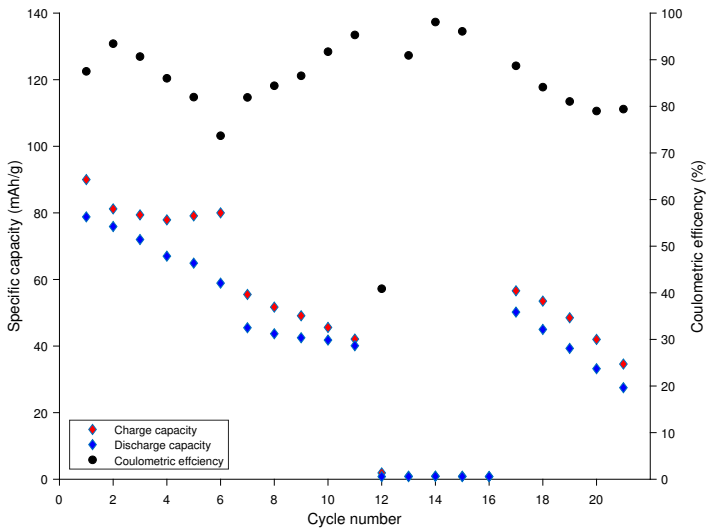


**Figure 4.16:** Galvanostatic cycling of half-cell assembled with $LiMn_2O_4$ from the sol-gel CA2 procedure, with cast with 10 wt. % PVDF.

For the half-cells assembled from cathode casts with 10 wt. % PVDF with $LiMn_2O_4$ form sol-gel CA2 procedure, the galvonstatic cycling showed a similar low capacity. As shown in Figure 4.16, there is a high initial discharge capacity present for the first cycle. The cell does however experience rapid capacity during the first 6 cycles, which is not present for the next 5 cycles with a C/10 C-rate. Next to no capacity is available during cycling at C/5. The last five cycles experienced rapid capacity fading. The charge-discharge curves shown in Figure 4.17, indicates that the characteristic shape for charge and discharge of $LiMn_2O_4$ is present. The curve is present in the last five cycles (Figure 4.17b) as well. This change is also shown in Figure 4.18 with the difference in the first and last cycle indicates a loss of available capacity during the reactions, and no other side reactions can be observed.

The half cells obtained from $LiMn_2O_4$ precipitate $MnO_2$ water dispersion with 10 % PVDF in the cathode cast showed the worst electrochemical properties. As shown in Figure 4.19 there is a constant loss in capacity as the cell is cycled, before the cell experienced sudden collapse in cycle 17. The charge-discharge curves, shown in Figure 4.20 shows a large difference in capacity between the first 6 cycles. Cycle 7 to 11 at C/10 C-rate have a far smaller loss in capacity. For cycle 17, the charge curve have a rather similar shape as the five first, as the charge capacity for this cycle is rather high. The discharge capacity on the other hand is next to nothing. The differential capacity analysis of cycle 1 and 17 (Figure

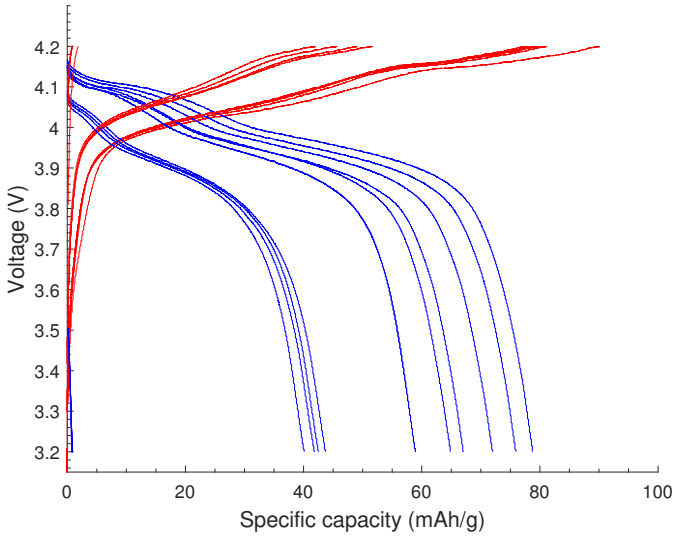


**(a)**

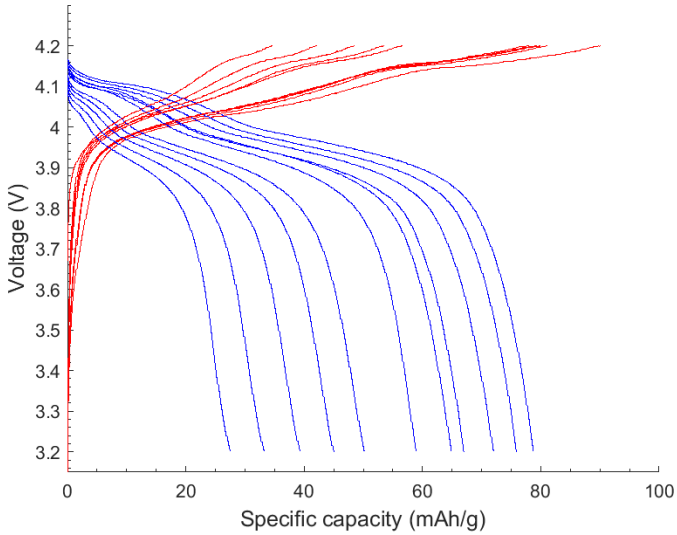


**(b)**

**Figure 4.17:** Charge-discharge curve of half-cell with $LiMn_2O_4$ from the sol-gel CA2 procedure and 10 wt. % PVDF. Cycle 1-16 is shown in (a) and cycle 1-6 and 17-21 is shown in (b).

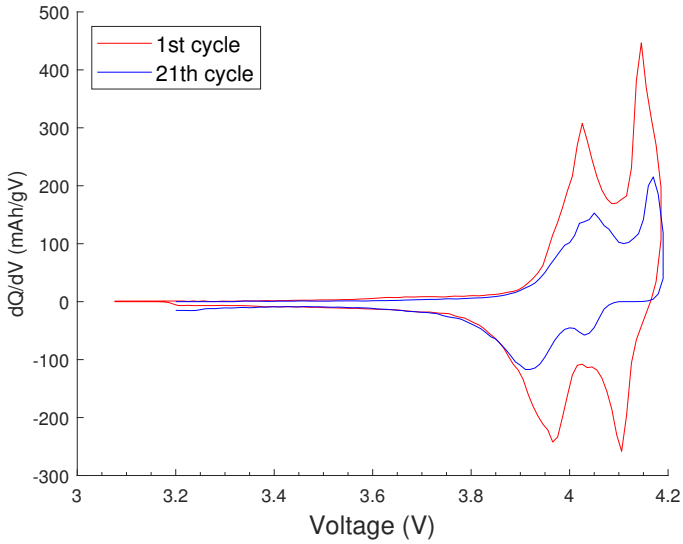


**Figure 4.18:** Differential capacity analysis of first and last cycle of half-cell assembled from $LiMn_2O_4$ obtained from sol-gel CA2 procedure, with 10 wt. % PVDF in cast.

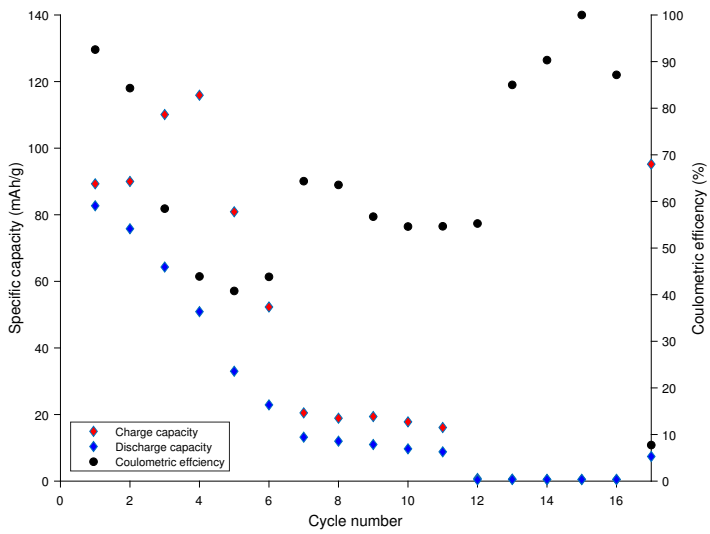


**Figure 4.19:** Galvanostatic cycling of half-cells assembled with $LiMn_2O_4$ from the precipitate $MnO_2$ water dispersion procedure and 10 wt. % PVDF in cathode cast.

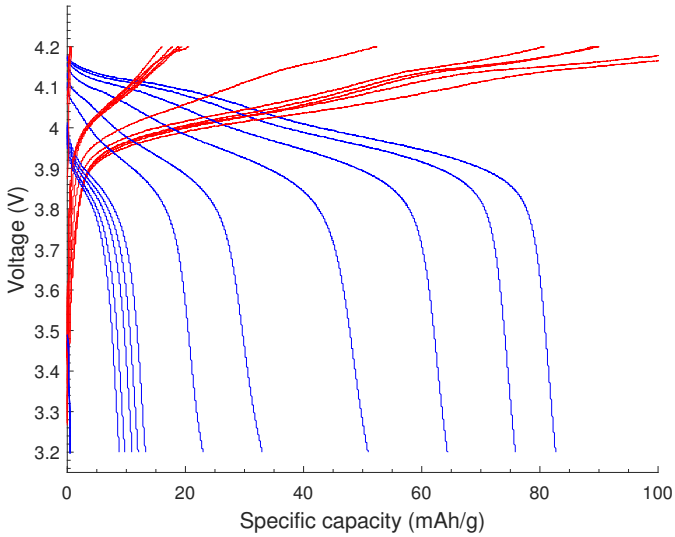


**(a)**

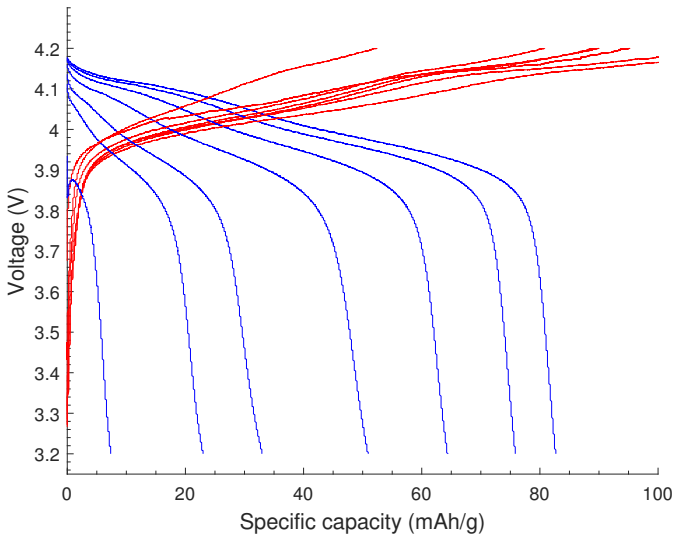


**(b)**

**Figure 4.20:** Charge discharge curves of half-cells with $LiMn_2O_4$ from the precipitated $MnO_2$ water dispersion procedure with 10 wt. % PVDF in cathode cast. (a) showns cycle 1-16 while cycle 1-6 and 17 is shown in (b).

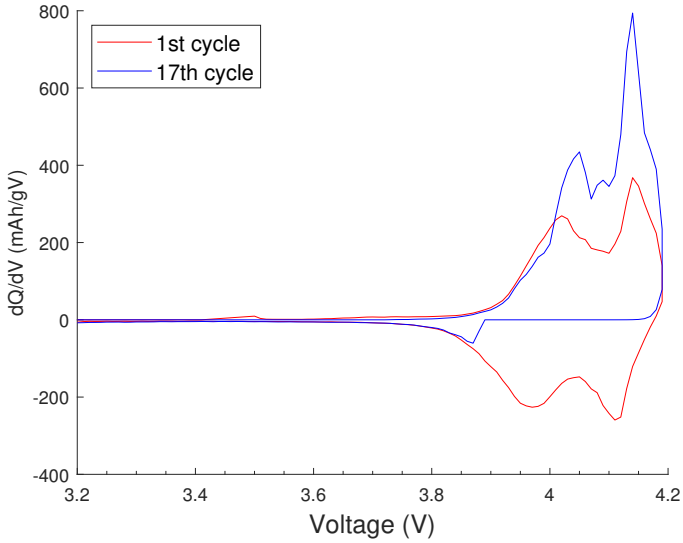


**Figure 4.21:** Differential capacity analysis curves of cycle 1 and 17 for half-cell with $LiMn_2O_4$ from the precipitate $MnO_2$ water dispersion procedure with 10 % PVDF in cathode casts.

4.21), shows that the last cycle heavily differs from the usual fingerprint for $LiMn_2O_4$, especially during discharge. As the characteristic peak around 4 V is lacking.

# Chapter 5

# Discussion

## 5.1 Relation between synthesis technique and particle morphology

The different particle morphologies obtained in this thesis shown that the influence to synthesis procedure have a large impact on the size and shape of the synthesis particles. This is especially the case for samples obtained from coprecipitation.

The SEM images of sample obtained through procedure precipitate $MnCO_3$ mortar and pestle, shows particles with an overall regular shape and homogenous particle distribution. The porous structure of the finished product can be attributed to the porous shape of $MnCO_3$ intermediate, which it often exhibit when formed through coprecipitation [18, 114]. However as shown In the X-ray diffraction date (Figure A.3 in Appendix A.1), the phase purity of $LiMn_2O_4$ obtained from precipitate $MnCO_3$ mortar and pestle was far to low to use in high voltage LIBs.

Comparing the size and shape of particles of precipitate $MnCO_3$ mortar and pestle 75 mL to precipitate $MnO_2$ water dispersion shows that the impact of the ratio of $Mn^{2+}$ to $NH_4HCO_4$ and the use of $MnO_2$ as intermediate greatly altered the microstructure of the finished sample. Precipitate $MnO_2$ water dispersion showed far greater size inhomogeneity and large deviation in particle morphology. The ratio and concentration of $NH_4HCO_3$ and $Mn^{2+}$-source can heavily impact final particle morphology as this will affect degree of supersaturation. Robinson and Koenig [16] have shown that altering the solution chemistry during precipitation will heavily impact the morphology of the finished product. The work done in this thesis was not able to replicate those results due to among other different $Mn^{2+}$ salt, different techniques used for mixing among others. The impact of switching between $Mn(CH_3CO_2)_2$ and $Mn(NO_3)_2$ as $Mn^{2+}$ source cannot be ignored. The formation of chelates, reaction with $CH_3CO_2^-$ and $NO_3^-$. And trapping of anions within the precipitating particles can also affect overall particle morphology [84, 115, 116]. However no study on the effect of $Mn^{2+}$ precursor on particle morphology have been found.

In general little difference in the microstructure of $LiMn_2O_4$ obtained from sol-gel synthesis was shown. A large sponge like structure is shown for $LiMn_2O_4$ obtained from sol-gel 800, which is not present for sol-gel CA2. However, the SEM image of sol-gel

800 was obtained before the sample was ball milled which explains the large open particle shown in Figure 4.4a. Comparing single particles (Figure 4.4c and Figure 4.5e) shows that both products obtained similar particle morphologies. The small crystals that are forming the larger particle in sol-gel 800 is slightly larger than the ones shown in sol-gel CA2, which can be attributed to the different calcination temperatures [17, 27, 110, 117]. The open structure present for both sol-gel 800 and sol-gel CA2 comes from the rapid decomposition of nitrates and the subsequent reaction with the organic gel components. Even as sol-gel CA2 did not experience the rapid decomposition the overall impact on the microstructure of the sample is not affected to any large extent. Thus, the combustion reaction can be omitted, without any large impact on particle morphology. The sol-gel synthesis could also have been done without with other easily soluble lithium and manganese salts. As sulphates, carbonates and acetates will decompose at high temperatures, but a far slower rate leaving a more compact overall structure [17, 57, 78].

## 5.2 Electrochemical performance

The electrochemical result from both sol-gel CA2 and $MnO_2$ water dispersion was inadequate for use in high-voltage LIBs. Both procedures yielded samples which exhibited low initial capacity, a large loss of initial capacity during cycling, large difference in terminal voltage during cycling, horrendous properties at high C-rates combined with large variance between samples. With regards to initial capacity precipitate $MnO_2$ water dispersion preformed marginally better than sol-gel CA2, but deteriorated far faster. A comparison of

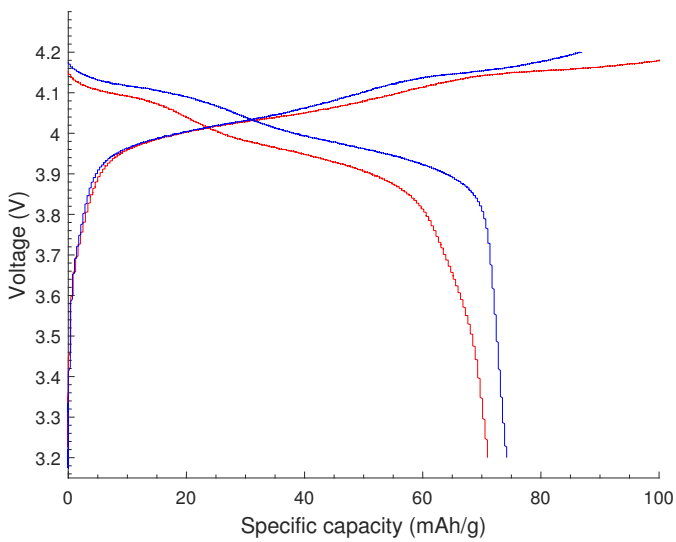


**Figure 5.1:** Comparision if the first charge discharge cycle, between the sol-gel CA2 (red) and precipitate $MnO_2$ water dispersion (blue), both from cast with 5 % PVDF.

the first charge discharge cycles for sol-gel CA2 and precipitate $MnO_2$ water dispersion

(both form cast with 5 % PVDF) (Figure 5.1), shows that behaviour during charge is similar. However there the terminal voltage of sol-gel CA2 is lower during discharge, which indicates larger polarisation and larger internal resistance during discharge [19].

The possible reasons for the poor performance of the half-cells may be attributed to

- Particle size
- Low degree of crystallinity
- Poor connection between active material and cathode cast
- Poor cast composition
- Particle strain

The average size of $LiMn_2O_4$ particles will have a huge impact on the electrochemical properties of the system. If the overall size is to large, the internal diffusion of $Li^+$ would increase, resulting in poorer electrochemical properties. However chapter12pacity and rate properties have been obtained for far larger and more compact particles, than those used in this thesis [65, 90]. The issue may however be related to low particle size, especially for half cells assembled from precipitate $MnO_2$ water dispersion procedure. This will also be an issue for sol-gel CA2, as even as the overall surface is more compact, compared to precipitate $MnO_2$ water dispersion. The overall particle size is still rather small compared to other works. The large surface area of both samples obtained, indicates that the particle size and shape can be an issue. As the large electrode-electrolyte interface present will aggravate the dissolution of manganese, due to the presence of HF, resulting in a larger capacity loss [65, 90].

The small particles present may lead to an overall reduction in particle performance, due the added resistance of electron transfer between grain boundaries and different particles [53, 65, 66].

A highly crystalline sample is essential to access the full capacity of $LiMn_2O_4$, as an amorphous structure would inhibit the internal $Li^+$.-diffusion as imperfections may block the $Li^+$ transition between 8a and 16c sites. The degree of crystallisation is heavily dependent on synthesis structure. For the sol-gel procedure, the sample will be amorphous before calcination and choice of calcination temperature is therefore essential [117] The X-ray diffractogram for sol-gel CA2, shows a fairly high background compared to peak height, compared to precipitate $MnO_2$ as shown in Figure 5.2. As the noisy background present indicated more presence of amorphous secondary phases in the sample [93, 118]. The increase the degree of crystallinity within the sample, the calcination temperature should have been higher [110, 117].

Some comparison was done of cathode cast before and after cycling, through both XRD and SEM imaging, but only of cast with 5 % PVDF by weight. The results from X-ray diffraction showed a difference in relative peak height, to the peaks present for the current collector without applied cast. Further as shown in Figure 4.13e and 4.13f there is regions of the cast present after cycling, where the cast have been removed from the current collector which would indicate poor connection between current collector and cathode cast. This compared with the void present in Figure 4.14 indicates poor cathode cast current adhesion. The presence of fluoride on the current collector in Figure 4.15d indicated that there was

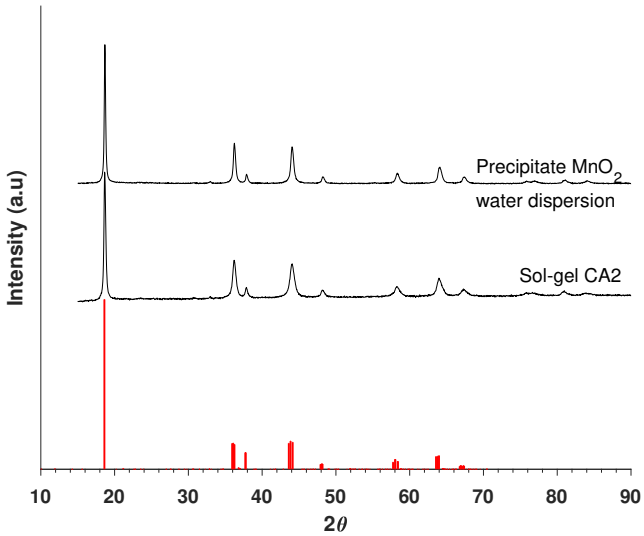


**Figure 5.2:** Comparison of X-ray diffractogram obtained from sol-gel CA2 and precipitate $MnO_2$ water dispersion procedure, alongside $LiMn_2O_4$ reference sample (red lines). Note, height of peaks have been normalised.

not enough binder in the solution to keep the cast adhered to the current collector. Attempts to remedy this was done by increasing the amount of PVDF to 10 % by mass. As both half cells with 10 wt. % PVDF in the cathode cast did not show an increase in electrochemical properties, this indicates that the connection between cathode cast and current collector was more than adequate, or the amount of PVDF in the cast was not the issue. Further $LiMn_2O_4$ cathode casts with 10 wt. % PVDF have been shown successfully to achieve chapter12pacity results, for samples with far larger surface area [53]. This indicated that the amount of PVDF in the cast was not the issue.

A poor and inhomogeneous cathode cast can result in poor and variable electrochemical properties. If the mixing of components is inadequate, this will introduce variations in the cast and measurements in the half cells. Thus, the effects longer mixing times and different amount of NEP in cast should be analysed.

Research on the effect on ball milling on $LiMn_2O_4$ have shown that it quickly introduces considerable strain in the individual particles [119]. As the strain will introduce distortions within the lattice, this alters the $Li^+$ diffusion path and may lead to higher polarisation during galvanostatic cycling [97].

Even if some small difference was present between sol-gel CA2 and precipitate $MnO_2$ water dispersion, the difference was not considerable. The challenge of obtaining phase pure $LiMn_2O_4$ through coprecipitation, prevented the synthesis of a wide range of particles as porous, compact spheres and cubes. Further the impact of calcination temperature on the electrochemical properties on $LiMn_2O_4$ should have been analysed.

Both samples exhibited poor capabilities at high C-rates. This can be attributed to the

large degree of polarisation which each sample showed. As the C-rate increases, so to does the electrical resistance within the cell, which would reduce the materials properties at high C-rates [19].

Assessment of the viability and changes in galvanostatic cycling at elevated temperatures was not carried out. This due to the poor performance the cells exhibited at 20 °C. As the capacity fading for $LiMn_2O_4$ is said to be far more severe at elevated temperatures [120]. Thus investigation into the effect of particle morphology on galvanostatic cycling remains an interesting field of research.

# Chapter 6

# Conclusion

Phase pure $LiMn_2O_4$ was synthesised through both sol-gel synthesis and coprecipitation, and the later technique proved able to synthesise particles with wildly different morphologies. This did not result in an material with the desired capacity or longevity. There is no lack of literature supporting the both synthesis techniques as viable for the formation $LiMn_2O_4$ with the desired capacity and different morphologies than the ones presented in this work [15–18, 57].

Both samples tested electrochemically was of similar morphology and, no large difference was observed between them. However due to slightly better performance after 16 cycles, sol-gel CA2 proved to be the marginally better synthesis technique. Synthesis of $LiMn_2O_4$ through coprecipitation proved that the technique could be used design particles with a with range of morphologies. But the mixing of intermediate with $LiNO_3$ proved to be crucial to obtain a phase pure material. The sol-gel synthesis with nitrate precursors proved to be able to form an open morphology reliably. Both techniques have potential to produce $LiMn_2O_4$ with a wide variety of morphologies, with synthesis through coprecipitation providing the largest option of possible results.

Further, the poor properties exhibited can be attributed to samples with a morphology which was not compatible for use in high voltage LIBs. A large number of samples with a large amount of a $Mn_2O_3$ secondary phase was synthesised, showing the importance of stochiometric control and proper mixing for to obtain a phase pure material.

# Chapter 7

# Further work

The first step in further research, should be in the optimisation of both synthesis techniques, as the electrochemical results was far from optimal. For sol-gel synthesis, the properties of samples calcinated at different temperatures should be evaluated. Sol-gel synthesis should also be done with different metal salt, as the less energetic decomposition of them would result in a more compact structure. From coprecipitation a reliable way to synthesise phase pure $LiMn_2O_4$ with the desired morphology should be found. This could yield particles with cubic, spheric and microporous morphology. Full investigation into the effect of the different morphologies should be done through galvanostatic cycling.

More information of the electrochemical behaviour of $LiMn_2O_4$ and the impact of different morphologies should be done through electrochemical impedance spectroscopy. As this technique offers a way to analyse rate kinetics within the system, and how it differs for different morphologies of $LiMn_2O_4$.

The capacity fading of $LiMn_2O_4$ is known to be far more severe at elevated temperatures. The influence of particle morphology on galvanostatic cycling at elevated temperatures should be investigated.

Further, research into stable ways to reduce the impact om manganese dissolution and Jahn-Teller distortion in $LiMn_2O_4$ should be done, such as surface doping, the addition of nickel in the structure and synthesising $LiMn_2O_4$ in a core-shell structure.

# Bibliography


[1] OECD. *Energy: The Next Fifty Years*. 1999. ISBN 1-280-08100-7.

[2] IPCC. *Climate Change 2013: The Physical Science Basis. Contribution of Working Group I to the Fifth Assessment Report of the Intergovernmental Panel on Climate Change*. Cambridge University Press, Cambridge, United Kingdom and New York, NY, USA, 2013. ISBN ISBN 978-1-107-66182-0.

[3] John B. Goodenough and Youngsik Kim. Challenges for Rechargeable Li Batteries. *Chemistry of Materials*, 22(3):587–603, 2010. doi: 10.1021/cm901452z.

[4] Akira Yoshino. The Birth of the Lithium-Ion Battery. *Angewandte Chemie International Edition*, 51(24):5798–5800, 2012. doi: 10.1002/anie.201105006.

[5] Arumugam Manthiram and Theivanayagam Muraliganth. *Lithium Intercalation Cathode Materials for Lithium-Ion Batteries*, chapter 12, pages 341–375. John Wiley Sons, Ltd, 2011. ISBN 9783527637188. doi: 10.1002/9783527637188.ch12.

[6] Chaofeng Liu, Robert C. Mass, Guozhong Cao, Yanwei Li, and Liqiang Mai. Energy storage through intercalation reactions: electrodes for rechargeable batteries. *National Science Review*, 4(1):26–53, 12 2016. ISSN 2095-5138. doi: 10.1093/nsr/nww093.

[7] Hui Xia, Zhentao Luo, and Jianping Xie. Nanostructured limn2o4 and their composites as high-performance cathodes for lithium-ion batteries. *Progress in Natural Science: Materials International*, 22(6):572 – 584, 2012. ISSN 1002-0071. doi: https://doi.org/10.1016/j.pnsc.2012.11.014.

[8] S.E. Olsen, S. Olsen, M. Tangstad, and T. Lindstad. *Production of Manganese Ferroalloys*. Tapir Akademisk Forlag, 2007. ISBN 9788251921916.

[9] J. Emsley. *Nature's Building Blocks: An A-Z Guide to the Elements*. Popular science. Oxford University Press, 2003. ISBN 9780198503408.

[10] Arumugam Manthiram, Katharine Chemelewski, and Eun-Sung Lee. A perspective on the high-voltage $LiMn_{1\cdot 5}Ni_{0\cdot 5}O_4$ spinel cathode for lithium-ion batteries. *Energy & Environmental Science*, 7(4):1339–1350, 2014. ISSN 1754-5692. doi: 10.1039/C3EE42981D.

[11] Jun-Yu Piao, Shu-Yi Duan, Xi-Jie Lin, Xian-Sen Tao, Yan-Song Xu, An-Min Cao, and Li-Jun Wan. Surface Zn doped $LiMn_2O_4$ for an improved high temperature performance. *Chem. Commun.*, 54:5326–5329, 2018. doi: 10.1039/C8CC01878B.

[12] Liwei Su, Yu Jing, and Zhen Zhou. Li ion battery materials with coreshell nanostructures. *Nanoscale*, 3:3967–3983, 2011. doi: 10.1039/C1NR10550G.

[13] Seung-Taek Myung, Hyung-Joo Noh, Sung-June Yoon, Eung-Ju Lee, and Yang-Kook Sun. Progress in High-Capacity CoreShell Cathode Materials for Rechargeable Lithium Batteries. *The Journal of Physical Chemistry Letters*, 5(4):671–679, 2014. doi: 10.1021/jz402691z. PMID: 26270835.

[14] Hong-Ming Zhou, Yu-Hua Zhu, Jian Li, Wen-Jiao Sun, and Zhong-Zhong Liu. Electrochemical performance of Al2O3 pre-coated spinel LiMn2O4. *Rare Metals*, 38(2):128–135, Feb 2019. ISSN 1867-7185. doi: 10.1007/s12598-014-0418-9.

[15] Nanostructured $LiMn_2O_4$ and their composites as high-performance cathodes for lithium-ion batteries. *Progress in Natural Science: Materials International*, 22(6): 572 – 584, 2012. ISSN 1002-0071. doi: https://doi.org/10.1016/j.pnsc.2012.11.014.

[16] J. Pierce Robinson and Gary M. Koenig. Tuning solution chemistry for morphology control of lithium-ion battery precursor particles. *Powder Technology*, 284:225 – 230, 2015. ISSN 0032-5910. doi: https://doi.org/10.1016/j.powtec.2015.06.070.

[17] Yang-Kook Sun, In-Hwan Oh, and Kwang Yul Kim. Synthesis of Spinel $LiMn_2O_4$ by the Sol-Gel Method for a Cathode-Active Material in Lithium Secondary Batteries. *Industrial & Engineering Chemistry Research*, 36(11):4839–4846, 1997. doi: 10.1021/ie970227b.

[18] Haowen Xiao, Yourong Wang, Kai Xie, Siqing Cheng, and Xianzhong Cheng. High capacitance $LiMn_2O_4$ microspheres with different microstructures as cathode material for aqueous asymmetric supercapacitors", journal = "Journal of Alloys and Compounds. 738:25 – 31, 2018. ISSN 0925-8388. doi: https://doi.org/10.1016/j.jallcom.2017.12.143.

[19] Karsten Pinkwart and Jens Tbke. *Thermodynamics and Mechanistics*, pages 1–26. Wiley-VCH Verlag GmbH & Co. KGaA, 2011. ISBN 9783527637188. doi: 10.1002/9783527637188.ch1.

[20] John B. Goodenough and Kyu-Sung Park. The Li-Ion Rechargeable Battery: A Perspective. *Journal of the American Chemical Society*, 135(4):1167–1176, 2013. ISSN 0002-7863. doi: 10.1021/ja3091438.

[21] Oldham K.B., Myland J.C., and Bond A.M. *Electrochemical Science and Technology: Fundamentals and Applications*. Wiley, 2012. ISBN 9780470710845.

[22] Naoaki Yabuuchi, Kei Kubota, Mouad Dahbi, and Shinichi Komaba. Research Development on Sodium-Ion Batteries. *Chemical Reviews*, 114(23):11636–11682, 2014. ISSN 0009-2665. doi: 10.1021/cr500192f.

[23] K. Momma and F. Izumi. Vesta 3 for three-dimensional visualization of crystal, volumetric and morphology data. `http://jp-minerals.org/vesta/en/`, 2011.

[24] Kenta Ooi, Yoshitaka Miyai, and Shunsaku Katoh. Recovery of Lithium from Seawater by Manganese Oxide Adsorbent. *Separation Science and Technology*, 21 (8):755–766, 1986. doi: 10.1080/01496398608056148.

[25] F Scholz and A. M Bond. *Electroanalytical Methods*. Springer Verlag, 2nd, rev. and extended ed. edition, 2010. ISBN 3642029140.

[26] T. Riley, C. Tomlinson, and A.M. James. *Principles of Electroanalytical Methods*. Analytical Chemistry by Open Learning. Wiley, 1987. ISBN 9780471913306.

[27] William E. Lee. David W. Richerson. *Modern Ceramic Engineering: Properties, Processing, and Use in Design, Fourth Edition*. CRC Press, 2018. ISBN 978-1-4987-1691-8.

[28] Debasish Mohanty, Jianlin Li, Shrikant C. Nagpure, David L. Wood, and Claus Daniel. Understanding the structure and structural degradation mechanisms in high-voltage, lithium-manganeserich lithium-ion battery cathode oxides: A review of materials diagnostics. *MRS Energy amp; Sustainability*, 2:E15, 2015. doi: 10.1557/mre.2015.16.

[29] Koji Nishio and Nobuhiro Furukawa. *Practical Batteries*, pages 27–85. Wiley-VCH Verlag GmbH & Co. KGaA, 2011. ISBN 9783527637188. doi: 10.1002/9783527637188.ch2.

[30] Werner Bhnstedt. *Separators*, pages 285–340. Wiley-VCH Verlag GmbH & Co. KGaA, 2011. ISBN 9783527637188. doi: 10.1002/9783527637188.ch11.

[31] Roy l'Abee, Fabien DaRosa, Mark J. Armstrong, Moritz M. Hantel, and Djamel Mourzagh. High temperature stable Li-ion battery separators based on polyetherimides with improved electrolyte compatibility. *Journal of Power Sources*, 345:202–211, 2017. ISSN 0378-7753. doi: http://dx.doi.org/10.1016/j.jpowsour.2017.02.005.

[32] Pankaj Arora and Zhengming Zhang. Battery Separators. *Chemical Reviews*, 104 (10):4419–4462, 2004. ISSN 0009-2665. doi: 10.1021/cr020738u.

[33] K. Vignarooban, R. Kushagra, A. Elango, P. Badami, B. E. Mellander, X. Xu, T. G. Tucker, C. Nam, and A. M. Kannan. Current trends and future challenges of electrolytes for sodium-ion batteries. *International Journal of Hydrogen Energy*, 41 (4):2829–2846, 2016. ISSN 0360-3199. doi: http://doi.org/10.1016/j.ijhydene.2015.12.090.

[34] A. Blackman, L.R. Gahan, G.H. Aylward, and T.J.V. Findlay. *Aylward and Findlay's SI Chemical Data*. John Wiley & Sons Australia, 2013. ISBN 9780730302469.

[35] Chaofeng Liu, Zachary G. Neale, and Guozhong Cao. Understanding electrochemical potentials of cathode materials in rechargeable batteries. *Materials Today*, 19(2):109–123, 2016. ISSN 1369-7021. doi: http://dx.doi.org/10.1016/j.mattod.2015.10.009.

[36] Martin Winter and Jrgen Otto Besenhard. *Lithiated Carbons*, pages 433–478. Wiley-VCH Verlag GmbH & Co. KGaA, 2011. ISBN 9783527637188. doi: 10.1002/9783527637188.ch15.

[37] Emanuel Peled, Diane Golodnitsky, and Jack Penciner. *The Anode/Electrolyte Interface*, pages 479–523. Wiley-VCH Verlag GmbH & Co. KGaA, 2011. ISBN 9783527637188. doi: 10.1002/9783527637188.ch16.

[38] Chengliang Wang, Yaoguo Fang, Yang Xu, Liying Liang, Min Zhou, Huaping Zhao, and Yong Lei. Manipulation of Disodium Rhodizonate: Factors for Fast-Charge and Fast-Discharge Sodium-Ion Batteries with Long-Term Cyclability. *Advanced Functional Materials*, 26(11):1777–1786, 2016. ISSN 1616-3028. doi: 10.1002/adfm.201504537.

[39] Katherine J. Harry, Daniel T. Hallinan, Dilworth Y. Parkinson, Alastair A. MacDowell, and Nitash P. Balsara. Detection of subsurface structures underneath dendrites formed on cycled lithium metal electrodes. *Nat Mater*, 13(1):69–73, 2014. ISSN 1476-1122. doi: 10.1038/nmat3793.

[40] Jinwang Tan and Emily M. Ryan. Computational study of electro-convection effects on dendrite growth in batteries. *Journal of Power Sources*, 323:67–77, 2016. ISSN 0378-7753. doi: http://dx.doi.org/10.1016/j.jpowsour.2016.05.012.

[41] Xiangchun Zhang, Myoungdo Chung, HyonCheol Kim, Chia-Wei Wang, and Ann Marie Sastry. *Mechanics of Battery Cells and Materials*, pages 877–904. Wiley-VCH Verlag GmbH & Co. KGaA, 2011. ISBN 9783527637188. doi: 10.1002/9783527637188.ch26.

[42] Kai Liu, Yayuan Liu, Dingchang Lin, Allen Pei, and Yi Cui. Materials for lithium-ion battery safety. *Science Advances*, 4(6), 2018. doi: 10.1126/sciadv.aas9820.

[43] V. Ruiz, A. Pfrang, A. Kriston, N. Omar, P. Van den Bossche, and L. Boon-Brett. A review of international abuse testing standards and regulations for lithium ion batteries in electric and hybrid electric vehicles. *Renewable and Sustainable Energy Reviews*, 81:1427 – 1452, 2018. ISSN 1364-0321. doi: https://doi.org/10.1016/j.rser.2017.05.195.

[44] Daniel H. Doughty. *Battery Safety and Abuse Tolerance*, pages 905–938. Wiley-VCH Verlag GmbH & Co. KGaA, 2011. ISBN 9783527637188. doi: 10.1002/9783527637188.ch27.

[45] Qiyin Lin, Qingan Li, Kenneth E. Gray, and John F. Mitchell. Vapor Growth and Chemical Delithiation of Stoichiometric LiCoO2 Crystals. *Crystal Growth & Design*, 12(3):1232–1238, 2012. doi: 10.1021/cg201238n.

[46] Anthony R. West. *Solid State Chemistry and its Applications, 2nd Edition, Student Edition*. Wiley, 2014. ISBN 978-1-119-94294-8.

[47] Richard J. D. Tilley. *Understanding Solids: The Science of Materials, 2nd Edition*. Wiley, 2013. ISBN 978-1-118-42328-8.

[48] Yujie Zhu, Tao Gao, Xiulin Fan, Fudong Han, and Chunsheng Wang. Electrochemical Techniques for Intercalation Electrode Materials in Rechargeable Batteries. *Accounts of Chemical Research*, 2017. ISSN 0001-4842. doi: 10.1021/acs.accounts.7b00031.

[49] Zhou Haitao. *Nanostructured cathode materials for Li-ion batteries*. PhD thesis, 2013.

[50] M. Stanley Whittingham. Lithium Batteries and Cathode Materials. *Chemical Reviews*, 104(10):4271–4302, 2004. doi: 10.1021/cr020731c. PMID: 15669156.

[51] Xin-Bing Cheng, Rui Zhang, Chen-Zi Zhao, and Qiang Zhang. Toward Safe Lithium Metal Anode in Rechargeable Batteries: A Review. *Chemical Reviews*, 117(15): 10403–10473, 2017. doi: 10.1021/acs.chemrev.7b00115.

[52] Hao Zheng, Ting Wang, Rongfei Zhao, Jinsong Chen, and Lin Li. $LiMn_2O_4$ microspheres as high-performance cathode materials for Li-ion batteries. *IOP Conference Series: Earth and Environmental Science*, 108(2):022011, jan 2018. doi: 10.1088/1755-1315/108/2/022011.

[53] Xiaoling Xiao, Jun Lu, and Yadong Li. $LiMn_2O_4$ microspheres: Synthesis, characterization and use as a cathode in lithium ion batteries. *Nano Research*, 3(10):733–737, Oct 2010. ISSN 1998-0000. doi: 10.1007/s12274-010-0037-1.

[54] Daichun Tang, Yang Sun, Zhenzhong Yang, Liubin Ben, Lin Gu, and Xuejie Huang. Surface Structure Evolution of $LiMn_2O_4$ Cathode Material upon Charge/Discharge. *Chemistry of Materials*, 26(11):3535–3543, 2014. doi: 10.1021/cm501125e.

[55] A. Mosbah, A. Verbaere, and M. Tournoux. Phases $Li_xMnO_2$ lambda rattachees au type spinelle. *Materials Research Bulletin*, 18:1375–1381, 1983.

[56] Jaephil Choa and Michael M. Thackeray. Structural Changes of $LiMn_2O_4$ Spinel Electrodes during Electrochemical Cycling. *Journal of The Electrochemical Society*, 146(10):3577–3581, 1999. doi: 10.1149/1.1392517.

[57] K. Ragavendran, H.L. Chou, L. Lu, Man On Lai, B.J. Hwang, R. Ravi Kumar, S. Gopukumar, Bosco Emmanuel, D. Vasudevan, and D. Sherwood. Crystal habits of $LiMn_2O_4$ and their influence on the electrochemical performance. *Materials Science and Engineering: B*, 176(16):1257 – 1263, 2011. ISSN 0921-5107.

[58] W.D. Callister and A.G. Rethwisch. *Material Science and Engineering*. Wiley, 2010. ISBN 978-0-470-50586-1.

[59] Xiaoling Xiao, Jun Lu, and Yadong Li. $LiMn_2O_4$ microspheres: Synthesis, characterization and use as a cathode in lithium ion batteries. *Nano Research*, 3(10):733–737, Oct 2010. ISSN 1998-0000. doi: 10.1007/s12274-010-0037-1.

[60] S. Demirel, E. Oz, S. Altin, A. Bayri, E. Altin, and S. Avci. Enhancement of battery performance of $LiMn_2O_4$: correlations between electrochemical and magnetic properties. *RSC Adv.*, 6:43823–43831, 2016. doi: 10.1039/C6RA05032H.

[61] Yu bo ZHOU, Yuan fu DENG, Wei hao YUAN, Zhi cong SHI, and Guo hua CHEN. Synthesis of spinel $LiMn_2O_4$ microspheres with durable high rate capability. *Transactions of Nonferrous Metals Society of China*, 22(10):2541 – 2547, 2012. ISSN 1003-6326. doi: https://doi.org/10.1016/S1003-6326(11)61498-2.

[62] Jun Lu, Chun Zhan, Tianpin Wu, Jianguo Wen, Yu Lei, A Jeremy Kropf, Huiming Wu, Dean J Miller, Jeffrey W Elam, Yang-Kook Sun, Xinping Qiu, and Khalil Amine. Effectively suppressing dissolution of manganese from spinel lithium manganate via a nanoscale surface-doping approach. *Nature Communications*, 5:5693, dec 2014.

[63] Michael Stich, Mara Gttlinger, Mario Kurniawan, Udo Schmidt, and Andreas Bund. Hydrolysis of $LiPF_6$ in Carbonate-Based Electrolytes for Lithium-Ion Batteries and in Aqueous Media. *The Journal of Physical Chemistry C*, 122(16):8836–8842, 2018. doi: 10.1021/acs.jpcc.8b02080.

[64] Ken Tasaki, Katsuya Kanda, Shinichiro Nakamura, and Makoto Ue. Decomposition of $LiPF_6$ and Stability of $PF_5$ in Li-Ion Battery Electrolytes: Density Functional Theory and Molecular Dynamics Studies. *Journal of The Electrochemical Society*, 150(12):A1628–A1636, 2003. doi: 10.1149/1.1622406.

[65] Ting-Feng Yi, Xin-Guo Hu, Chang-Song Dai, and Kun Gao. Effects of different particle sizes on electrochemical performance of spinel $LiMn_2O_4$ cathode materials. *Journal of Materials Science*, 42(11):3825–3830, Jun 2007.

[66] R Vacassy, H Hofmann, N Papageorgiou, and M Grtzel. Influence of the particle size of electrode materials on intercalation rate and capacity of new electrodes. *Journal of Power Sources*, 81-82:621 – 626, 1999. ISSN 0378-7753. doi: https://doi.org/10.1016/S0378-7753(99)00232-3.

[67] Yige Sun, Chengjun Xu, Baohua Li, Jinzao Xu, Yan-Bing He, Hongda Du, and Feiyu Kang. Synthesis of single-crystalline limn2o4 with different dimensional nanostructures for li-ion batteries. *International Journal of Electrochemical Science*, 9:6387–6401, 11 2014.

[68] Muhamad Zamri Yahaya, Mohd Asyadi Azam, Mohd Asri Mat Teridi, Pramod Kumar Singh, and Ahmad Azmin Mohamad. Recent Characterisation of Sol-Gel Synthesised $TiO_2$ Nanoparticles. In Usha Chandra, editor, *Recent Applications in Sol-Gel Synthesis*, chapter 6. IntechOpen, Rijeka, 2017. doi: 10.5772/67822.

[69] Terho Kololuoma, Jaakko Leppniemi, Himadri Majumdar, Rita Branquinho, Elena Herbei-Valcu, Viorica Musat, Rodrigo Martins, Elvira Fortunato, and Ari Alastalo. Gravure printed solgel derived AlOOH hybrid nanocomposite thin films for printed electronics. *J. Mater. Chem. C*, 3:1776–1786, 2015. doi: 10.1039/C4TC02022G.

[70] Larry L. Hench and Jon K. West. The sol-gel process. *Chemical Reviews*, 90(1): 33–72, 1990. doi: 10.1021/cr00099a003.

[71] E.R. Merz, C.E. Walter, and G.M. Pshakin. *Mixed Oxide Fuel (Mox) Exploitation and Destruction in Power Reactors*. Nato Science Partnership Subseries: 1. Springer Netherlands, 2013. ISBN 9789401722889.

[72] Sol-gel-derived silica preforms for optical fibers. *Journal of Non-Crystalline Solids*, 178:272 – 283, 1994. ISSN 0022-3093. doi: https://doi.org/10.1016/0022-3093(94)90296-8.

[73] Guanghu He, Zhengwen Cao, Wenyuan Liang, Yan Zhang, Xin Liu, Jrgen Caro, and Heqing Jiang. Codoping Strategy To Improve Stability and Permeability of $Ba_0 \cdot {}_6Sr_0 \cdot {}_4FeO_3\delta$-Based Perovskite Membranes. *Industrial & Engineering Chemistry Research*, 55(39):10386–10393, 2016. doi: 10.1021/acs.iecr.6b02134.

[74] Peifeng ZHANG, Huiqing FAN, Yunfei FU, Zhuo LI, and Yongli DENG. Synthesis and electrochemical properties of sol-gel derived $LiMn_2O_4$ cathode for lithium-ion batteries. *Rare Metals*, 25(6, Supplement 1):100 – 104, 2006. ISSN 1001-0521. doi: https://doi.org/10.1016/S1001-0521(07)60053-9.

[75] Lei Jia-heng, Sun Yu-bin, Chen Yong-xi, Wang Jin-rong, and Xue Li-hui. Sol-gel synthesis of normal spinel $LiMn_2O_4$ and its characteristics. *Journal of Wuhan University of Technology-Mater. Sci. Ed.*, 17(3):1–4, Sep 2002. ISSN 1993-0437. doi: 10.1007/BF02838527.

[76] A citric acid method to prepare $LiMn_2O_4$ for lithium-ion batteries. *Solid State Ionics*, 121(1):79 – 84, 1999. ISSN 0167-2738. doi: https://doi.org/10.1016/S0167-2738(98)00532-3.

[77] Effect of various synthetic parameters on purity of $LiMn_2O_4$ spinel synthesized by a solgel method at low temperature. *Journal of Power Sources*, 101(1):86 – 89, 2001. ISSN 0378-7753. doi: https://doi.org/10.1016/S0378-7753(01)00657-7.

[78] A. E. Danks, S. R. Hall, and Z. Schnepp. The evolution of solgel chemistry as a technique for materials synthesis. *Mater. Horiz.*, 3:91–112, 2016. doi: 10.1039/C5MH00260E.

[79] Rachel A. Caruso and Markus Antonietti. SolGel Nanocoating: An Approach to the Preparation of Structured Materials. *Chemistry of Materials*, 13(10):3272–3282, 2001. doi: 10.1021/cm001257z.

[80] Sumio Sakka. *History of the SolGel Chemistry and Technology*, pages 3–29. Springer International Publishing, Cham, 2018. ISBN 978-3-319-32101-1. doi: 10.1007/978-3-319-32101-1_87.

[81] P. J. Flory. Introductory lecture. *Faraday Discuss. Chem. Soc.*, 57:7–18, 1974. doi: 10.1039/DC9745700007.

[82] C. Jeffrey Brinker and George w. Scherer. *Sol-Gel Science: The Physics and Chemistry of Sol-Gel Processing*. Academic Press, INC., 1990. ISBN 0-12-134970-5.

[83] Yuanyuan Li, Lihong Xue, Lingfang Fan, and Youwei Yan. The effect of citric acid to metal nitrates molar ratio on solgel combustion synthesis of nanocrystalline lamno3 powders. *Journal of Alloys and Compounds*, 478(1):493 – 497, 2009. ISSN 0925-8388. doi: https://doi.org/10.1016/j.jallcom.2008.11.068.

[84] J.W. Mullin. *Crystallization, 4th edition.* Chemical, Petrochemical & Process. Butterworth-Heinemann, 2001. ISBN 0750648333.

[85] Allan S. Myerson and Rajiv Ginde. 2 - crystals, crystal growth, and nucleation. In Allan S. Myerson, editor, *Handbook of Industrial Crystallization (Second Edition)*, pages 33 – 65. Butterworth-Heinemann, Woburn, second edition edition, 2002. ISBN 978-0-7506-7012-8. doi: https://doi.org/10.1016/B978-075067012-8/50004-5.

[86] Peter G Vekilov. Nucleation. *Crystal growth & design*, 10(12):5007–5019, nov 2010. ISSN 1528-7483. doi: 10.1021/cg1011633.

[87] I. M. Kolthoff. Theory of Coprecipitation. The Formation and Properties of Crystalline Precipitates. *The Journal of Physical Chemistry*, 36(3):860–881, 1931. doi: 10.1021/j150333a008.

[88] D. Kashchiev and G. M. van Rosmalen. Review: Nucleation in solutions revisited. *Crystal Research and Technology*, 38(78):555–574. doi: 10.1002/crat.200310070.

[89] James J. De Yoreo and Peter Vekilov. Principles of Crystal Nucleation and Growth. *Reviews in Mineralogy Geochemistry - REV MINERAL GEOCHEM*, 54:57–93, 01 2003. doi: 10.2113/0540057.

[90] Xiang Ming He, Jian Jun Li, Yan Cai, Yaowu Wang, Jierong Ying, Changyin Jiang, and Chunrong Wan. Preparation of spherical spinel $LiMn_2O_4$ cathode material for lithium ion batteries. *Journal of Solid State Electrochemistry*, 9(6):438–444, Jun 2005. ISSN 1433-0768. doi: 10.1007/s10008-004-0593-y.

[91] Andrei A. Bunaciu, Elena gabriela Udritioiu, and Hassan Y. Aboul-Enein. X-Ray Diffraction: Instrumentation and Applications. *Critical Reviews in Analytical Chemistry*, 45(4):289–299, 2015. doi: 10.1080/10408347.2014.949616.

[92] P.C Hemmer. *Faste stoffers fysikk*. Tapir, Trondheim, 1987. ISBN 8251908159.

[93] B.D. Cullity and S.R. Stock. *Elements of X-ray diffraction, 3rd edition*. Prentice Hall, 2001. ISBN 0201610914.

[94] I Chorkendorff. *Concepts of modern catalysis and kinetics*. Weinheim, 3rd ed. edition, 2017. ISBN 9783527332687.

[95] G. Cao and Y. Wang. *Nanostructures and Nanomaterials: Synthesis, Properties, and Applications*. World Scientific series in nanoscience and nanotechnology. World Scientific, 2011. ISBN 9789814322508.

[96] Charles Kittel. *Introduction to solid state physics*. Wiley, Hoboken, N.J, 8th ed. edition, 2005. ISBN 9780471415268.

[97] Jinhan Yao, Chaoqi Shen, Pinjie Zhang, Duncan H. Gregory, and Lianbang Wang. Enhanced cycle ability of spinel $LiMn_2O_4$ by controlling the phase purity and structural strain. *Journal of Physics and Chemistry of Solids*, 73(11):1390 – 1395, 2012. ISSN 0022-3697. doi: https://doi.org/10.1016/j.jpcs.2012.07.006.

[98] Stephen Brunauer, P. H. Emmett, and Edward Teller. Adsorption of Gases in Multimolecular Layers. *Journal of the American Chemical Society*, 60(2):309–319, 1938. ISSN 0002-7863. doi: 10.1021/ja01269a023.

[99] The bet method of analysis of gas adsorption data and its relevance to the calculation of surface areas. *Surface Technology*, 4(2):121 – 160, 1976. ISSN 0376-4583. doi: https://doi.org/10.1016/0376-4583(76)90024-8.

[100] T. Kogure. Chapter 2.9 - electron microscopy. In Faza Bergaya and Gerhard Lagaly, editors, *Handbook of Clay Science*, volume 5 of *Developments in Clay Science*, pages 275 – 317. Elsevier, 2013. doi: https://doi.org/10.1016/B978-0-08-098259-5.00011-1.

[101] Weilie Zhou, Robert Apkarian, Zhong Lin Wang, and David Joy. *Fundamentals of Scanning Electron Microscopy (SEM)*, pages 1–40. Springer New York, New York, NY, 2007. ISBN 978-0-387-39620-0. doi: 10.1007/978-0-387-39620-0_1.

[102] J. Goldstein, D.E. Newbury, D.C. Joy, C.E. Lyman, P. Echlin, E. Lifshin, L. Sawyer, and J.R. Michael. *Scanning Electron Microscopy and X-Ray Microanalysis: Third Edition*. Springer US, 2003. ISBN 0-306-47292.

[103] Archana Kayyar, Jiajia Huang, Mojtaba Samiee, and Jian Luo. Construction and testing of coin cells of lithium ion batteries. *Journal of visualized experiments : JoVE*, (66):e4104–e4104, aug 2012. ISSN 1940-087X. doi: 10.3791/4104.

[104] Vivian Murray, David S. Hall, and J. R. Dahn. A Guide to Full Coin Cell Making for Academic Researchers. *Journal of The Electrochemical Society*, 166(2):A329–A333, 2019. doi: 10.1149/2.1171902jes.

[105] Robert Spotnitz. *Separators for Lithium-Ion Batteries*, pages 693–717. Wiley-VCH Verlag GmbH & Co. KGaA, 2011. ISBN 9783527637188. doi: 10.1002/9783527637188.ch20.

[106] A. J. Smith and J. R. Dahn. Delta Differential Capacity Analysis. *Journal of The Electrochemical Society*, 159(3):A290–A293, 2012. doi: 10.1149/2.076203jes.

[107] Lauren M. Marzocca and Terrill B. Atwater. Differential Capacity-Based Modeling for In-Use Battery Diagnostics, Prognostics, and Quality Assurance. Unpublished, 2018. Accessed: 2019-05-20.

[108] Akiya Kozawa, Kohei Yamamoto, and Masaki Yoshio. *Electrochemistry of Manganese Oxides*, pages 125–148. Wiley-VCH Verlag GmbH & Co. KGaA, 2011. ISBN 9783527637188. doi: 10.1002/9783527637188.ch4.

[109] Nikolai Helth Gauks and Kara Poon. Thermogravimetric Standarization of Cation Solutions. Unpublished, 2017.

[110] Emrah Bulut, Ahmet Örnek, and Mahmut Özacar. Effect of Calcination Temperature on Synthesis of $LiMn_2O_4$ Cathode Active Nanoparticles for Rechargeable Li-Ion Batteries. *Advanced Science, Engineering and Medicine*, 3(1-2):67–71, 2011. ISSN 2164-6627. doi: doi:10.1166/asem.2011.1072.

[111] ICDD: The International Centre for Diffraction Data. Pdf-4+ 2019, 2019. URL `http://www.icdd.com/index.php/pdf-4/`.

[112] Bruker. Diffrac.eva, version 4.2. URL `https://www.bruker.com/products/x-ray-diffraction-and-elemental-analysis/x-ray-diffraction.html/`.

[113] Jrg H. Albering. *Structural Chemistry of Manganese Dioxide and Related Compounds*, pages 87–123. Wiley-VCH Verlag GmbH & Co. KGaA, 2011. ISBN 9783527637188. doi: 10.1002/9783527637188.ch3.

[114] Yuanfu Deng, Yubo Zhou, Zhicong Shi, Xue Zhou, Xie Quan, and Guohua Chen. Porous $LiMn_2O_4$ microspheres as durable high power cathode materials for lithium ion batteries. *J. Mater. Chem. A*, 1:8170–8177, 2013. doi: 10.1039/C3TA11563A.

[115] M.T. McCall and M.E. Tadros. Effects of additives on morphology of precipitated calcium sulfate and calcium sulfite implications on slurry properties. *Colloids and Surfaces*, 1(2):161 – 172, 1980. ISSN 0166-6622. doi: https://doi.org/10.1016/0166-6622(80)80003-5.

[116] Seniz Ucar, Sindre H. Bjrny, David C. Bassett, Berit L. Strand, Pawel Sikorski, and Jens-Petter Andreassen. Transformation of brushite to hydroxyapatite and effects of alginate additives. *Journal of Crystal Growth*, 468:774 – 780, 2017. ISSN 0022-0248. doi: https://doi.org/10.1016/j.jcrysgro.2016.11.019. The 18th International Conference on Crystal Growth and Epitaxy (ICCGE-18).

[117] M.N Rahaman. *Sintering of ceramics*. CRC Press, Boca Raton, Fla, 2008. ISBN 9780849372865.

[118] R. A. Young, editor. *The Rietveld method*. Oxford University Press, 1993. ISBN 0198555776.

[119] Tom Eriksson. *LiMn2O4 as a Li-Ion Battery Cathode: From Bulk to Electrolyte Interface*. PhD thesis, 2001.

[120] Kyung Yoon Chung, Hung Sui Lee, Won-Sub Yoon, James McBreen, and Xiao-Qing Yang. Studies of $LiMn_2O_4$ Capacity Fading at Elevated Temperature Using In Situ Synchrotron X-Ray Diffraction. *Journal of The Electrochemical Society*, 153(4): A774–A780, 2006. doi: 10.1149/1.2172565.

# Appendix A

# Supplementary data

## A.1 Phase characterisation

This section covers phase analysis of samples not used for electrochemical analysis. Sol-gel samples calcinated at different temperatures are shown in Figure A.1, sol-gel samples with pH modification is shown in Figure A.2 and samples made through coprecipitation in Figure A.3. All samples shows the characteristic peaks for $LiMn_2O_4$ around 19, 36, 44 and 64 $2\theta$. However peaks at 33 $2\theta$ is present in a large number of samples alongside peaks around 23 and 55 $2\theta$, which have been attributed to the presence of a $Mn_2O_3$ secondary phase.

A secondary phase identified as $Mn_2O_3$ is present in many samples here, In general, increase in calcination temperature results in more narrow peaks and less noise present in the diffractograms as shown in Figure A.1. The presence of a secoundary phase of $Mn_2O_3$ is present in particular in sample sol-gel 500, sol-gel 600, sol-gel 700. A secondary phase of $Mn_2O_3$ is present in all samples with pH modification as shown in Figure A.2, in general the lower the pH the less the presence of $Mn_2O_3$. The of $Mn_2O_3$ od in particular present in sol-gel pH 2.25 and sol-gel 4. The X-ray diffractogram for selected $LiMn_2O_4$ samples made through coprecipitation is shown in Figure A.3. These samples all shows characteristic peaks for $Mn_2O_3$, especially samples where intermediate and $LiNO_3$ was mixed by hand with mortar and pestle. Samples where mixing was done through ball milling shows a far lower presence of the $MnCO_3$ secondary phase, but its presence is still significant.

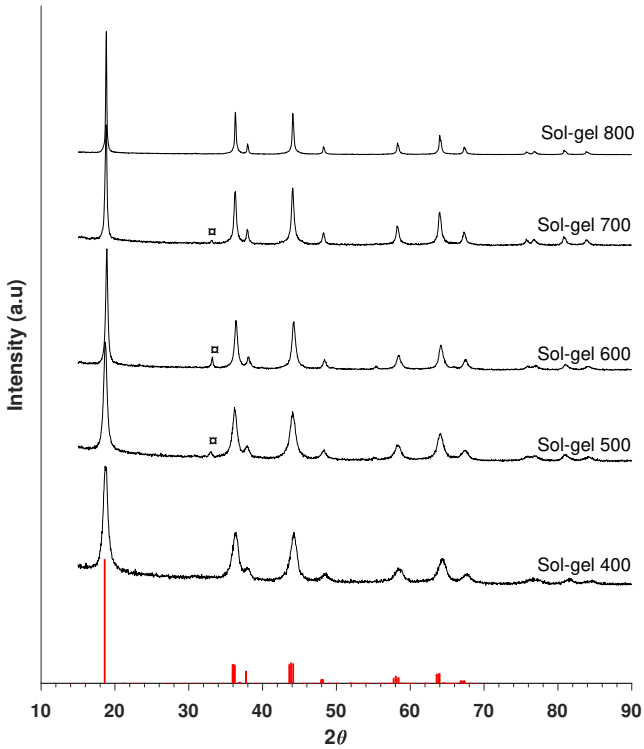


**Figure A.1:** X-ray diffraction of sol-gel samples calcined at different temperatures. Red lines represents $LiMn_2O_4$ reference sample, while ¤ marks characteristic peaks for a $Mn_2O_3$ secondary phase. Note, height of all peaks have been normalised.

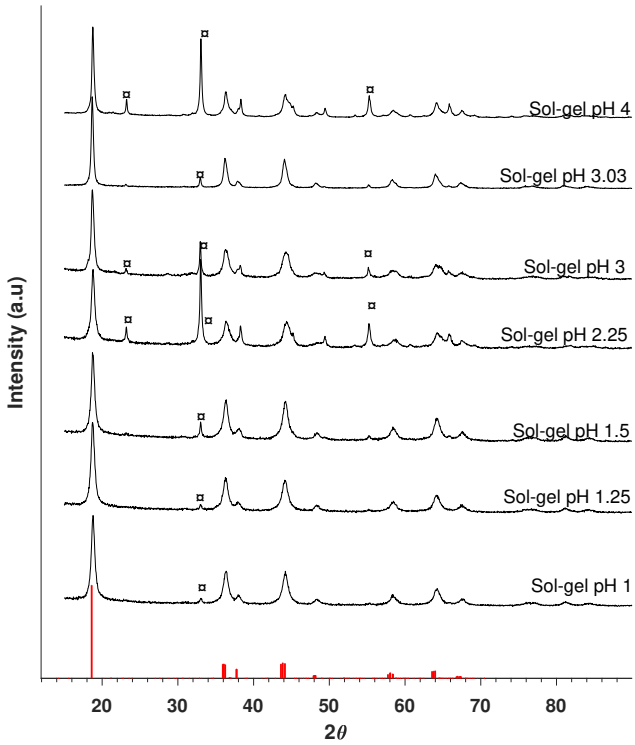


**Figure A.2:** X-ray diffraction of sol-gel samples with active pH modification. Red lines are $LiMn_2O_4$reference sample, while ¤ marks characteristic peaks for a $Mn_2O_3$ secondary phase. Note, height of all peaks have been normalised.

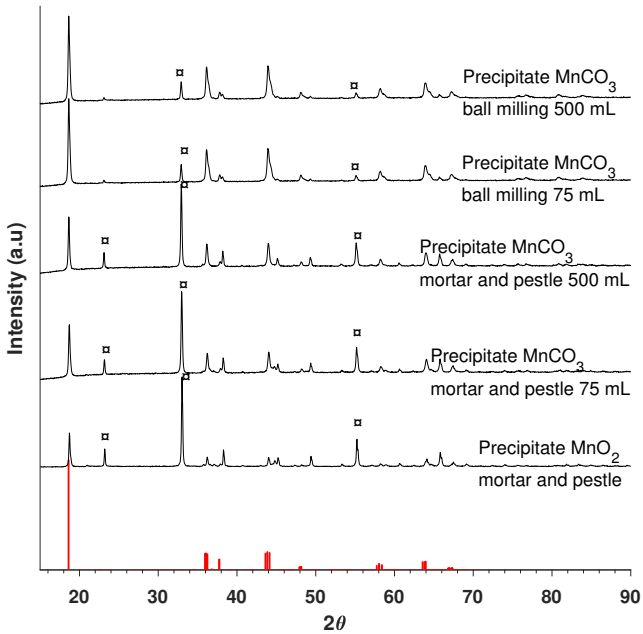


**Figure A.3:** XRD measurement of selected $LiMn_2O_4$ samples synthesised through coprecipitation. Red lines are $LiMn_2O_4$ reference samples, while ¤ marks the presence of a $Mn_2O_3$ secondary phase. Note, intensity if all heights are normalised.

## A.2 Energy dispersive X-ray spectroscopy

The energies of the elements detected in Figure 4.15b and 4.15d is shown in Table A.1. Spectrum for cross section mapping of electrode with void present (Figure 4.15d) is shown in Figure A.4. The spectrum for EDS mapping of cross section without void (Figure 4.15b) is shown in Figure A.5.

**Table A.1:** Characteristic energies of the elements detected in this thesis with EDS.

| Element | Energy of characteristic X-ray [kV] |
|---|---|
| Li | - |
| Mn | 5.898 |
| | 0.637 |
| O | 0.523 |
| C | 0.277 |
| F | 0.677 |
| Al | 1.486 |
| | 0.073 |

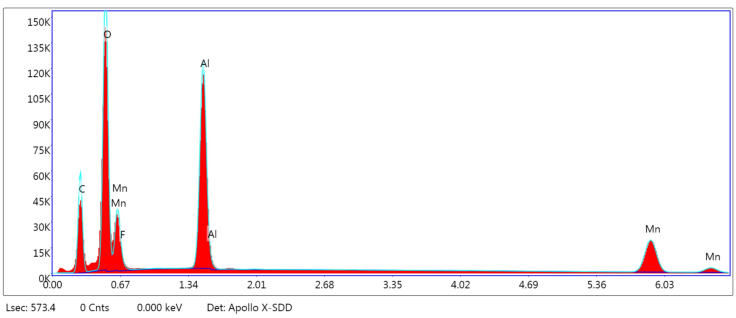


**Figure A.4:** Spectrum for region mapped

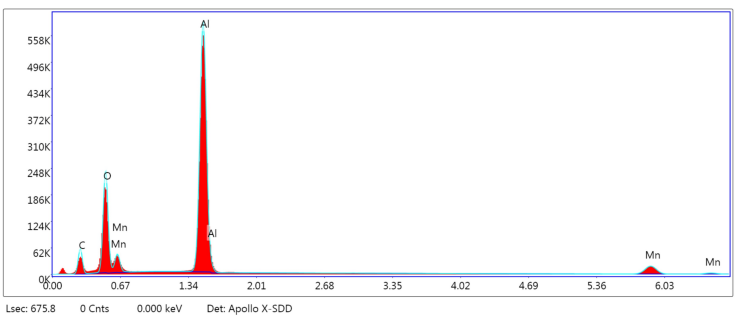


**Figure A.5:** Spectrum for region mapped

## A.3 Electrochemical results

This section contains an overview of the electrochemical results presented in Section 4.3, shown in Table A.2.

**Table A.2:** Full overview over the cells presented in this thesis

| Cycle number | Sample | Sol-gel CA2 5 wt. % PVDF | Sol-gel CA2 10 wt. % PVDF | Precipitate $MnO_2$ water dispersion 5 wt. % PVDF | Precipitate $MnO_2$ water dispersion 10 wt. % PVDF |
|---|---|---|---|---|---|
| $1^{st}$ | Charge capacity (mAh/g) | 109.0 | 90.0 | 86.9 | 89.3 |
| | Discharge capacity (mAh/g) | 71.1 | 81.2 | 74.2 | 82.7 |
| | Coulometric efficiency (%) | 65.23 | 87.51 | 85.42 | 92.58 |
| | Energy efficiency (%) | 69.18 | 94.28 | 90.07 | 97.61 |
| $6^{th}$ | Charge capacity (mAh/g) | 73.7 | 80.0 | 79.4 | 52.3 |
| | Discharge capacity (mAh/g) | 64.0 | 58.9 | 68.2 | 22.9 |
| | Coulometric efficiency (%) | 86.78 | 73.70 | 85.84 | 43.83 |
| | Energy efficiency (%) | 82.91 | 70.69 | 83.71 | 41.18 |
| $7^{th}$ | Charge capacity (mAh/g) | 51.6 | 55.5 | 70.0 | 20.5 |
| | Discharge capacity (mAh/g) | 46.3 | 45.5 | 62.5 | 13.2 |
| | Coulometric efficiency (%) | 89.76 | 81.92 | 89.28 | 64.35 |
| | Energy efficiency (%) | 83.99 | 78.57 | 85.73 | 59.53 |
| $11^{th}$ | Charge capacity (mAh/g) | 45.2 | 42.1 | 78.0 | 16.1 |
| | Discharge capacity (mAh/g) | 42.7 | 40.1 | 57.5 | 8.8 |
| | Coulometric efficiency (%) | 94.45 | 95.32 | 73.65 | 54.67 |
| | Energy efficiency (%) | 88.22 | 89.20 | 70.40 | 50.14 |
| $12^{th}$ | Charge capacity (mAh/g) | 1.0 | 1.9 | 7.7 | 0.8 |
| | Discharge capacity (mAh/g) | 0.2 | 0.8 | 5.7 | 0.4 |
| | Coulometric efficiency (%) | 23.42 | 40.88 | 73.44 | 55.27 |
| | Energy efficiency (%) | 18.79 | 33.86 | 62.59 | 45.58 |
| $16^{th}$ | Charge capacity (mAh/g) | 0.3 | 0.8 | 5.2 | 0.5 |
| | Discharge capacity (mAh/g) | 0.3 | 0.8 | 4.9 | 0.5 |
| | Coulometric efficiency (%) | 93.20 | 100 | 94.46 | 100 |
| | Energy efficiency (%) | 73.55 | 0.8108 | 79.60 | 71.34 |
| $17^{th}$ | Charge capacity (mAh/g) | 69.0 | 56.6 | 133.3 | 95.2 |
| | Discharge capacity (mAh/g) | 63.7 | 50.2 | 53.4 | 7.4 |
| | Coulometric efficiency (%) | 92.27 | 88.7 | 40.3 | 7.74 |
| | Energy efficiency (%) | 87.91 | 84.15 | 38.49 | 6.96 |
| $21^{th}$ | Charge capacity (mAh/g) | 68.4 | 34.6 | 86.7 | - |
| | Discharge capacity (mAh/g) | 63.6 | 27.5 | 52.8 | - |
| | Coulometric efficiency (%) | 92.31 | 79.41 | 60.85 | - |
| | Energy efficiency (%) | 88.07 | 74.49 | 58.07 | - |

Hans-Olav Melløy

NTNU
Norwegian University of
Science and Technology